NON INVASIVE CHARACTERIZATION OF TISSUE THERMAL CONDUCTIVITY, BLOOD PERFUSION AND ELASTICITY *IN-VIVO* USING MAGNETIC RESONANCE IMAGING AND HIGH INTENSITY FOCUSED ULTRASOUND

A Dissertation Presented to

the Faculty of the Department of Physics

University of Houston

In Partial Fulfillment

of the Requirements for the Degree

Doctor of Philosophy

By

Jiming Zhang

December 2013

NON INVASIVE CHARACTERIZATION OF TISSUE THERMAL CONDUCTIVITY, BLOOD PERFUSION AND ELASTICITY *IN-VIVO* USING MAGNETIC RESONANCE IMAGING AND HIGH INTENSITY FOCUSED ULTRASOUND

Jiming Zhang

APPROVED:

Dr. Pei-Herng Hor, Chariman

Dr. Raja Muthupillai
St Luke's Episcopal Hospital

Dr. Wu-Pei Su

Dr. Chin-Sen Ting

Dr. Shuheng Pan

Dr. Donald Kouri

Dr. Dan Wells, Dean
College of Natural Sciences and Mathematics

ACKNOWLEDGEMENTS

I am forever indebted to Dr. Pei-Herng Hor and Dr. Raja Muthupillai for their guidance and support throughout this endeavor. Their unbridled enthusiasm for this work was contagious and inspiring. Their thoughtful insights, creative ideas, and informative discussions have also played a key role in the successful completion of this work. It has been a privilege to work with such professional scientists. I would also like to express my deep gratitude to Dr. Wu-Pei Su, Dr. Donald Kouri, Dr. Shuheng Pan, and Dr. Chin-Sen Ting for their insightful comments in each meeting of annual progress evaluation.

I am also thankful to Amol Pednekar and Zheng Wu with whom I have spent countless hours discussing my work and life in general. I'd like also to thank senior labmate Ramkumar Krishnamurthy for his help during the stage of learning magnetic resonance imaging.

I would like to sincerely thank all the clinical and research staff (Benjamin Cheong, Fischer John, June Garcia, Claudio Arena, Janie Swaab, Andre Duffy, Dave Crocker, David Leija, Debra Dees, Brenda Lambert, and Misty Meredith) in the lab of imaging research in radiology department at St Luke's Episcopal Hospital and Philips Healthcare (Ari Partanen, Greg Smith, Charles Mougenot, Max Kohler, Tiina Karjalainen, and Lizette Warner) for their help and support in phantom, *in-vivo* in animal and uterine fibroid studies. Thank you, junior labmate Feifei Qu, for regular discussion in the lab meeting.

I also want to thank my close friends in Houston: Ying Yi, Xiaoqiang Li, Xiaohan Ma, Xu Li, Haoying Liu, Zhiqiang Wang, and their spouse, who made my graduate student day cherishable ones.

On a personal note, I wish to convey all my love and appreciation to my wonderful wife Li Chen, for her encouragement to pursue research as a career and taking care of my loving family (2 years old daughter Jessie Zhang and 2 months old boy Albert Zhang) during the past six years. Dragging along my unconditionally loving spouse through the rigors of the PhD program is not fair to them, and I hope to give back to her all they have given me. Her patience and encouragement helped me focus on the important things in life, not necessarily my dissertation, and also helped me enjoy the good times and get through the not so good times. My special gratitude and love goes to my older brother Buzhou Zhang who supported me in all facts during the application and living in United States; otherwise I would not have this great chance to work and meet so many nice and insightful people in Houston. I also would like to thank my mother- and father- in-law and my parents for coming to Houston to help take care of my lovely two young kids, and their forever love and selfless spirit to my family. I would also like to thank my older sister Shuangquan Zhang, young sister Songting Zhang, two young brothers Baigen Zhang, Jisong Zhang, and my sister-in-law Hui Chen and her husband Zengchao Zhang and brother-in-law Bo Chen for their encouragement and forever support for my family.

NON INVASIVE CHARACTERIZATION OF TISSUE THERMAL CONDUCTIVITY, BLOOD PERFUSION AND ELASTICITY *IN-VIVO* USING MAGNETIC RESONANCE IMAGING AND HIGH INTENSITY FOCUSED ULTRASOUND

An Abstract of a Dissertation

Presented to

the Faculty of the Department of Physics

University of Houston

In Partial Fulfillment

of the Requirements for the Degree

Doctor of Philosophy

By

Jiming Zhang

December 2013

ABSTRACT

In Magnetic resonance imaging (MRI) guided high intensity focused ultrasound (MR-HIFU) surgery, high-intensity ultrasound beam is focused within the body under MRI guidance to create focal regions of thermal coagulation. MR-HIFU surgery is increasingly used to non invasively ablate uterine fibroids, breast cancer, and liver metastases. Until now, MR-HIFU surgery used thermal dose as a sole measure of treatment effectiveness, without taking into account the bio-thermal and bio-mechanical properties of tissue, as well as tissue physiologic response to HIFU heating. In this dissertation, we propose methods to use the MR-HIFU system, to characterize tissue thermal (conductivity), physiological (blood perfusion), and mechanical (elasticity) properties. We have performed *in-vivo*, non invasive measurements of tissue thermal conductivity and studied the thermal response of blood perfusion to thermal ablation of pig muscle and uterine fibroids using MR-HIFU. We demonstrate the feasibility of measuring elasticity in phantom by MRI tracking the mechanic wave propagation introduced by a transient discharge of acoustic radiation force from HIFU. The results showed that the thermal conductivity of muscle tissue undergoes little variation at clinical MR-HIFU surgery temperature range (60^{o}C~90^{o}C) compared to the value at lower temperature ($<40^{o}$C). However the local blood perfusion rate undergoes a fast (in tens of seconds) and large increase (~20 times) compared to that in the muscle without thermal ablation. The shear elasticity estimated by MR-HIFU agrees with conventional MR elastograhy method for estimating mechanical property of tissue mimicking phantoms. We demonstrate that the non invasive, *in-vivo* characterization of thermal conductivity, blood perfusion behavior and mechanical property can be carried out in one MR-HIFU platform. It will eventually benefit the planning, the heating stratagem, and the outcome of thermal surgery.

CONTENTS

LIST OF FIGURES

LIST OF TABLES

Chapter 1

Introduction

The significance of accurate and successful treatment of tumor or neoplasm (either benign or malignant) cannot be overstated. The traditional method of treating tumor is to undergo invasive open surgery procedure. Open surgical procedures involved significant patient morbidity post-intervention in terms of prolonged recovery time, and potential for treatment-related acute and chronic complications. Alternative approaches that can potentially reduce patient morbidity, while preserving or improving treatment effectiveness, is an ongoing quest in the field of medicine. One of most investigated non invasive surgical alternative is the treatment of tumors via thermal ablation based on high intensity focused ultrasound (HIFU)[1, 2] . HIFU ablation rapidly destroys tumor by coagulative necrosis of the tissue in tens of seconds at the focus without damaging the intervening structures passed by ultrasound beam [3]. The success of HIFU surgery depends on precise localization of tumor region (planning), targeting HIFU beam on the tumor without damaging surrounding healthy tissue (treatment), and evaluating the effectiveness of treatment during and after ablation (evaluation). In magnetic resonance imaging (MRI)-guided HIFU, MRI is used as a non invasive imaging modality to plan, monitor and evaluate thermal ablation. Since its initial description as a potential therapeutic device, MR-HIFU has been used to treat uterine fibroids[4-7], prostate cancer[8, 9], and breast cancer [10-12]. A routinely used metric to measure the efficiency of thermal ablation is the deposited thermal dose measured in the units of equivalent minutes at 43 ℃[13] . While this is a useful metric, the thermal dose required to cause tissue necrosis, is governed by bio-thermal properties and physiological response of the target tissue to thermal ablation. At present, the current generation of clinical MR-HIFU devices provide the user with control over the applied acoustic power (*W*), duration

(*s*), and frequency (*f*). However, very little information about the tissue bio-thermal, and bio-mechanical properties are known, and MR-HIFU treatment proceeds until a pre-defined threshold of thermal dose is attained. An accurate *a-priori* knowledge about the tissue thermal properties such as thermal conductivity, tissue physiologic response to heating (e.g., perfusion changes), and tissue mechanical properties could help to deliver thermal dose in a more efficient, and controlled manner. In this dissertation, we propose mechanisms to use the therapeutic MR-HIFU device to non invasively measure *tissue thermal conductivity* and *tissue blood perfusion* response during thermal therapy using HIFU.

Furthermore, it is conceivable that tissue bio-thermal properties, as well as biomechanical properties could serve as non invasive diagnostic markers of disease. For example, it is now well recognized that tissue stiffness is a marker of health [14, 15]. For example, American Cancer Society recommends breast self examination as a screening tool for early detection of breast cancer[16]. However, palpation is a qualitative method of characterizing tissue stiffness. It would be highly desirable to have a non invasive, quantitative imaging device to assess tissue stiffness beyond the reach of the palpating arm of the physician. We propose to use the MR-HIFU platform *to* non invasive*ly measure tissue mechanical properties* – a potential parameter that could be used to evaluate the effectiveness of HIFU therapy. A brief description of the content of each chapter in this dissertation is given below.

- **Chapter 2**: This background chapter consists of the motivation behind tissue thermal, physiological and mechanical properties characterization, in the context of MR-HIFU. The chapter also briefly outlines the principle of MRI, and the theoretical basis of using MRI to measure spin motion, and tissue temperature. Following the MR description, tissue thermal and mechanical effect from HIFU is described.

- **Chapter 3**: The accuracy of lesion targeting via HIFU, in terms of the spatial location of the HIFU focus within the tissue, the spatial extent of heating, and the precision of the MRI temperature measurement, of the MR-HIFU system used in this study are evaluated in this chapter. The validation experiments using MRI and HIFU were performed in tissue mimicking gel phantoms, as well as in *in-vivo* animal models. Preliminary evaluation of the accuracy and precision of the MR-HIFU device was also evaluated *in-vivo* in the treatment of uterine fibroids. The determinants of the accuracy of the MR temperature measurements in terms of spatial resolution are also described in this chapter.
- **Chapter 4**: This chapter introduces the theoretical principle behind the estimation of tissue thermal conductivity from the spatial-temporal temperature spread in MR-HIFU. The validation of this method was done by comparing the thermal conductivity estimated from HIFU heating of pig thigh muscle *in-vivo* to the published data. This method was then applied to estimate the thermal conductivity of uterine fibroid *in-vivo*, to obtain a patient specific thermal parameter. The merits and limitations of this method are also discussed.
- **Chapter 5**: Numerical methods to model tissue blood perfusion behavior during HIFU therapy are described in this chapter. A bio-heat transfer model was used to simulate the temperature evolution measured from HIFU heating of pig thigh muscle *in-vivo*, under the assumptions of constant perfusion rate and temperature-dependent perfusion rate. The model was also applied to estimate thermal perfusion of uterine fibroid treatment *in-vivo*. A large and fast increase of the blood perfusion rate was found to be necessary to account for the *in-vivo* temperature evolution in both *in-vivo* pig thigh muscle and uterine fibroid.

- **Chapter 6**: The theoretical basis, experimental means, and analysis methods necessary to estimate tissue mechanical properties by using MRI to measure tissue displacement caused by shear waves emanating from the HIFU focus are described in this chapter. The feasibility of visualizing shear waves is experimentally demonstrated in phantoms. The estimated mechanical property was verified using conventional magnetic resonance elastography (MRE) method. The safety issues regarding temperature rise related to the pulse HIFU excitation was also analyzed.
- **Chapter 7**: A summary of the specific contributions of this dissertation in estimating tissue thermal conductivity, tissue perfusion, and tissue mechanical properties in the context of MR-HIFU surgery is presented in this chapter. A summary of potential clinical applications that could potentially benefit from the knowledge of tissue bio-thermal, physiologic, and biomechanical properties is briefly discussed.

Chapter 2

Background

2.1 Current Tissue Properties Characterization

For the successful clinical application of ablative procedures involving focused ultrasound [17-19], radiofrequency energy [20, 21], hyperthermia [22, 23], and cryogenics [24, 25], physicians must be able to create lesions accurately and precisely by either heating or freezing tissue. Tissue response to heating (or cooling) is to dissipate the disruptive thermal energy via conduction, convection, and radiation in order to maintain thermal homeostasis. Therefore, an accurate knowledge of tissue thermal properties (such as thermal conductivity, specific heat, and blood perfusion rate) and of how these properties depend on temperature is necessary for understanding and controlling heat transfer in living tissue [26]. The success of these ablative procedures may be enhanced with the knowledge of the tissue thermal properties and physiologic responses of tissue to heating in the targeted area. Changes to tissue mechanical properties such as elasticity can serve as surrogates for the effectiveness of ablative therapies.

One ablative method is to focus ultrasound energy deep within the tissue to cause non invasive local heating, and to use an external imaging modality such as magnetic resonance imaging (MRI) to measure the resulting temperature increase within tissue. These ablative methods are commonly referred to as MRI-guided High Intensity Focused Ultrasound Therapy (MR-HIFU), and would be the topic of interest in this dissertation.

An abbreviated summary of the background information regarding the measurement of tissue thermal conductivity, tissue blood perfusion, and tissue elasticity in the context of MR-HIFU is presented below.

2.1.1 Tissue Thermal Conductivity

Measuring thermal conductivity involves three basic components: 1) a known heat source to deposit well-controlled thermal energy to the region of interest (ROI); 2) an effective modality to monitor and record tissue thermal response, namely, the spatio-temporal temperature evolution due to controlled heating; and 3) an efficient algorithm to extract the thermal conductivity.

Invasive methods to measure tissue thermal conductivity:

The first *ex-vivo* measurement of thermal conductivity on excised human fat and muscle tissue was performed in 1951 using contact heat disks to heat tissue specimen, and thermo-couples to measure the temperature change. A steady-state solution of Penne's bio-heat equation was used to calculate thermal conductivity[27]. Small thermo-couple probes were then developed and invasively inserted into cat kidney tissue to measure effective thermal conductivity *in-vivo* using steady state solution algorithm to extract thermal conductivity[28]. To avoid the complicated set-up associated with steady-state measurement, a simplified transient method using self-heated thermistor was introduced to measure tissue thermal conductivity *in vitro* (effective thermal conductivity)[29]. Further refinements of the transient heating approach involved a variety of techniques such as self-heated thermistor method[30-32], thermal probe pulse-decay method[33, 34] and micro hot-wire method[35-37] were used to evaluate tissue thermal conductivity either *in-vivo* or *in vitro*. These invasive measurements yielded tissue thermal conductivity with better than 5% accuracy. The invasive nature of the heat probes and the measurements, invariably limited the scope of these methods to in vitro or animal studies. For human studies, it would be desirable to have a method that uses both a non invasive heating probe as well as a measurement device.

Non invasive *methods to measure tissue thermal conductivity:*

Modern techniques such as infrared imaging [38], ultrasonography [39], and MRI [40] have been used to non invasively measure the thermal conductivity of epidermis on the arm of a Caucasian adult, the breast of a turkey, and the thigh muscle of rabbit, respectively. Infrared imaging is restricted to superficial applications because its penetration depth (which is wavelength-dependent) is only a few millimeters. Ultrasound-based methods are also limited, as the relationship between temperature and the ultrasound wave speed is linear only within a narrow change range (0~15 ℃) [41]. In contrast, MRI-based methods are unencumbered by constraints related to the depth of penetration and can span a relatively large thermodynamic range (0 ℃ to 100 ℃) making it an attractive measurement tool for quantitatively estimating the tissue thermal conductivity.

With respect to the heat source, unlike the traditional use of invasive probes such as self-heated thermistors, micro hotwire, or the laser fibers, it would be desirable to have a virtual heating source. One potential mechanism for depositing heat within the body in a non invasive manner is the use of focused ultrasound. In a manner analogous to a child using a magnifying lens to concentrate sunlight to a focal point to burn paper, sound waves can be focused to a small area and greatly increase the desired effect of thermal energy. The energy beams can be focused to heat a volume as small as a few cubic millimeters within the body, while sparing tissue outside the target. The combination of high-intensity focused ultrasound to generate heat within the body, and MRI as a heat measurement device, makes MR-HIFU an attractive non invasive therapeutic platform capable of measuring tissue thermal properties such as thermal conductivity.

2.1.2 Tissue Blood Perfusion

MR-HIFU has been widely used as a clinical modality of non invasively treating uterine fibroid [4-7], breast tumor [10-12], gene therapy[42], and palliative bone treatment[43], and for local drug delivery [44, 45] based on the absorption of focused ultrasound energy in the target. Several studies have shown that the eventual tissue damage caused by thermal ablation is highly variable. A dominant reason for this variation is the response of the body to maintain thermostasis, by dissipating the excess heat via thermally induced vasodilation[46]. If the thermal energy delivered is insufficient to overwhelm the competing effect of increase in perfusion, then the treatment may be compromised or ineffective. In the laser induced thermal ablation, the temperature-dependent blood perfusion rate was shown to significantly affect accumulated damage volume (30% less than invariant blood perfusion)[47, 48]. The temperature distribution in microwave thermal therapy has also been shown to be profoundly altered by local blood perfusion [49-51].

Much of the current knowledge regarding tissue perfusion response to heating comes from the hyperthermia literature, where the target tissue is heated to moderate temperatures (<45^{o}C) over relatively long period of time (several tens of minutes). In animal models, hyperthermia induced by using energy sources such as microwave[49-51], focused ultrasound[52, 53], radio-frequency[54], etc, all result in significant alterations in local blood perfusion. However, it must be noted that all studies that measured hyperthermia induced perfusion changes were done at relatively low temperatures (< 45 ℃) and occurred over several tens of minutes. However, in the case of HIFU thermal surgery, the target is heated rapidly (in tens of seconds) to temperatures in excess of 60 ℃ to kill the tumor tissues. The bio-thermal response of tissue to such extreme heating, i.e., changes in local blood perfusion is still largely unknown. We are going to study the behavior of tissue blood perfusion at therapeutic temperature level using MR-HIFU.

2.1.3 Tissue Elasticity

Though temperature sensitive MRI sequences permit reliable measurement of temperature (and calculate thermal dose) during heating to estimate the success of HIFU procedure, it would be desirable to have independent measures of treatment outcome. For example, it is known that protein denaturation due to heating can change local tissue stiffness [55-57]. This provides a potential contrast mechanism that may be exploited to distinguish treated regions from untreated regions. Tissue elasticity has been shown to be an attractive contrast parameter to evaluate, as evident from its clinical adoption in the case of liver MR Elastography (MRE) as a non invasive tool to measure liver fibrosis. MRE assessment of liver fibrosis obviates the need for invasive liver biopsies that suffers from significant sampling error(14.5%-25%), poor reproducibility[58-60], and has the potential for causing non-insignificant morbidities such as bleeding, pneumothorax, biliary tree puncture and death (~1 in 10,000-12,000) [61],[62].

The strength of tissue elasticity as a contrast parameters is the large dynamic range of tissue stiffness between normal and pathological states of the tissue [63], compared to underlying contrast parameters assessed using CT, MR, or ultrasound[64, 65]. Such a large dynamic range raises the possibility that changes in tissue elastic properties may be sufficiently sensitive to detect even identify early stages of carcinogenesis and it's possible that they may even have predictive value in certain types of cancer[65-67]. There is some evidence to show that the tissue elastic parameters are significantly affected by thermal ablation[55-57].

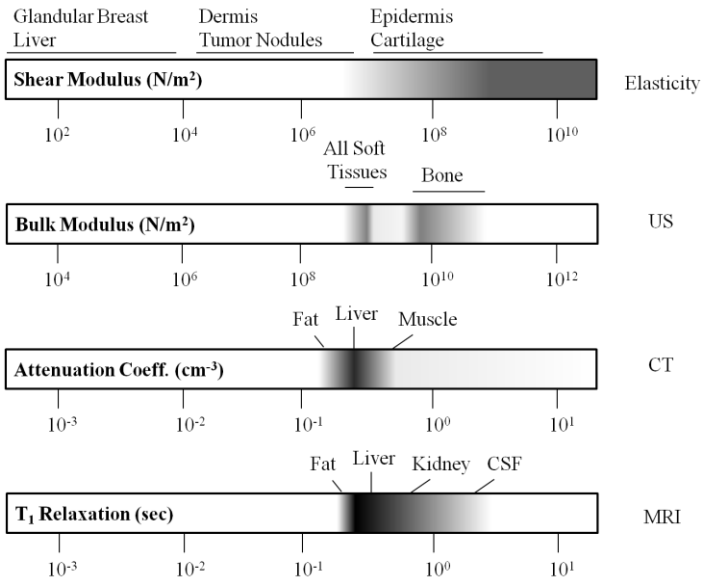

Figure 2.1 The bulk elastic modulus, x-ray attenuation coefficient, and the MR relaxation parameters that form the basis of tissue contrast in US, CT and MR span about an order of magnitude in soft-tissues. In contrast, the shear elastic modulus spans nearly six orders of magnitude between different tissue types.

Quantitative estimation of tissue elasticity involves subjecting the tissue to a mechanical deformation (stress), measurement of the resulting deformation (strain), and reconstructing tissue mechanical properties from the knowledge of the two using suitable algorithms.

While tissue elasticity can be estimated by applying a known static compression to the tissue[68], and measuring the resulting tissue deformation, this method requires accurate and complete information of both the stress and strain distribution within the body – something that is difficult to obtain *in-vivo*. Furthermore, such static measurements do not provide information regarding the time dependent components of tissue elasticity, e.g., viscosity. MR-HIFU-based tissue elasticity measurement overcomes both these limitations.

In this dissertation, we propose and test a method that has the potential to use the MR-HIFU therapeutic device to generate mechanical waves within the body, and use MRI to measure the minute tissue displacements caused by the generated mechanical wave. We propose to impart a mechanical disturbance at the focal point using the acoustic radiation force (ARF) using HIFU

system, and measuring the resulting tissue response using MRI. The propagation of the mechanical disturbance within tissue can yield information about tissue mechanical properties.

2.2 MR-HIFU for Non invasive *in-vivo Tissue Property Characterization*

2.2.1 Introduction of MR-HIFU

The coupling of HIFU to non invasively impart thermal energy within the body at specific locations in a controlled manner with MRI based non invasive measurement of temperature *during* therapy has made MR-HIFU an attractive modality for tissue ablation. Additional advantages of MRI include its excellent soft tissue contrast that allows soft-tissue target delineation *before* treatment [69], and evaluation of outcome *after* treatment. Studies have demonstrated that MR-HIFU can create well-defined regions of irreversible cell damages consisting of protein denaturation, and coagulation necrosis within the body at target locations[70-72]. *In-vivo* human studies show tremendous promise in the treatment of masses within the body, and prominent clinical applications include MR-HIFU treatment of tumors of the breast[10-12], kidney[73], prostate[8, 9], liver[74], and uterus[4-7].

The biophysical effects of HIFU within the body are twofold. First, the local, rapid rise of temperature at the focus – bio-thermal response, and second, the mechanical effect (so called, acoustic radiation force) caused by the abrupt change in the acoustic pressure gradient at the focus[75-79]. In the following two subsections, the background knowledge of MRI and HIFU will be reviewed separately before describing the methods for characterizing tissue thermal, physiological and mechanical properties by this integrated MR-HIFU system.

2.2.2 Magnetic Resonance Imaging

The intrinsic magnetic properties of atomic nuclei form the basis of MRI signal. Atomic nuclei such as, ^{1}H, ^{31}P, ^{23}Na, ^{13}C, etc., which have odd number of protons or neutrons (an unpaired nucleon), possess a net nuclear spin angular momentum (***I***) and a magnetic dipole moment (**m**). These two vector quantities are related by [80]:

$$\boldsymbol{m} = \gamma \boldsymbol{I} \tag{2.2}$$

where γ is the gyromagnetic ratio characteristic of nuclei.

The potential energy of the dipole in an external static magnetic field $\boldsymbol{B_0}$ is given by the negative of the scalar product between the vectors $\boldsymbol{B_0}$ and ***m***. The external magnetic field $\boldsymbol{B_0}$ exerts a torque ($\boldsymbol{\tau}$) on the magnetic moment (***m***) given by the vector product of $\boldsymbol{B_0}$ and ***m***[80].

$$\boldsymbol{\tau} = \boldsymbol{m} \times \boldsymbol{B_0} \tag{2.3}$$

In case of an atomic nucleus such as ^{1}H with an intrinsic spin angular momentum (***I***), Equation 2.3 can be rewritten as:

$$\boldsymbol{\tau} = \boldsymbol{m} \times \boldsymbol{B_0} = \frac{\mathrm{d}\boldsymbol{I}}{\mathrm{dt}} \tag{2.4}$$

Combining Eq. (2.2) and (2.4), the following relationship can be obtained.

$$\frac{\mathrm{d}\boldsymbol{m}}{\mathrm{dt}} = \gamma \boldsymbol{m} \times \mathbf{B_0} \tag{2.5}$$

This equation is known as the Larmor equation, describing the motion of magnetic dipole moment with a spin angular momentum in the presence of an external magnetic field as a precession of ***m*** about $\boldsymbol{B_0}$ (depicted in Fig. 2.2).

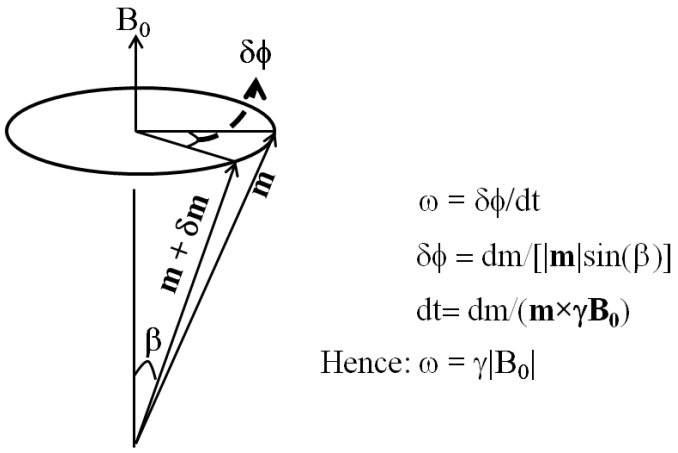

Figure 2.2 Diagram of a spin precessing about B_0 with an angular momentum. The angular frequency (ω) is derived using Eq. 2.5.

The precessional frequency, known as Larmor frequency, is proportional to the external magnetic field strength (derivation shown in Fig.2.2).

$$\omega_0 = \gamma |\mathbf{B_0}| \tag{2.6}$$

2.2.2.1 MRI Spatial Encoding

Two steps toward generating a MR image are: 1) creating a measurable magnetization; and 2) encoding the spatial distribution of the measurable magnetizations.

1) Origin of measurable magnetization:

According to the quantum mechanical rules, the allowed orientation for a nuclear spin in an external magnetic field is finite and discrete. The number of allowed states is equal to $2\boldsymbol{I}+1$. For hydrogen, contains only one proton, the angular momentum is 1/2. So the resultant allowed orientation is two: either spin up (higher energy) or spin down (lower energy) states. The relative

population distribution between these two energy states is represented by the known Boltzmann distribution[80]:

$$\frac{n_+(spin\ up, +1/2)}{n_-(spin\ down, -1/2)} = \exp\left(\frac{\Delta E}{kT}\right) \tag{2.7}$$

where k is the Boltzmann constant, T is the temperature of the sample, n_+ and n_- are the number of spins at a lower energy state (parallel aligned with $\boldsymbol{B_0}$) and higher energy state (anti-parallel aligned with $\boldsymbol{B_0}$), and ΔE is the energy difference between these two states, which is equal to $\gamma\hbar\boldsymbol{B_0}$, where $\hbar$ is the reduced Planck constant. If the water sample was maintained at absolute zero temperature, all protons will align with the direction of external magnetic field (lower energy state). However, if the temperature of the sample is not absolute zero, the thermal motion of the atoms will cause the dipoles to occupy both the allowed two energy states. The energy difference between the two spin states (ΔE) is much smaller than the thermal energy causing $\Delta E/kT << 1$. In this case the number of spins parallel to the magnetic field exceeding the number anti-parallel to that field, the 'spin excess', is also very small. There is only an excess fraction of about 1×10^{-6} protons in the lower energy state at room temperature in a magnetic field of 0.3 Tesla (Fig. 2.3).

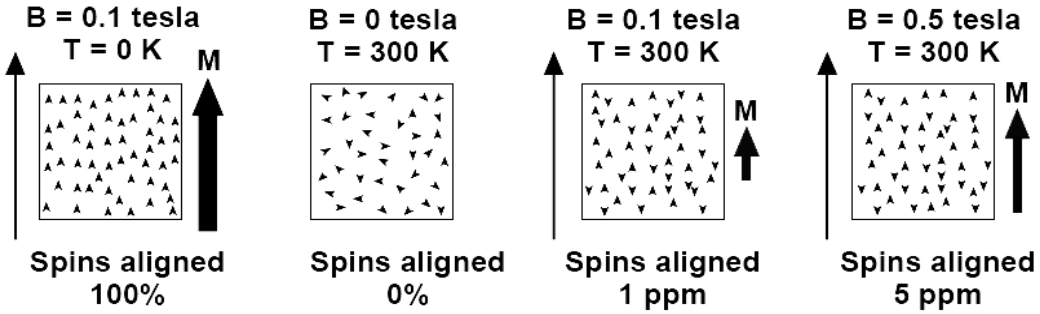

Figure 2.3 Creation of net magnetization **M** as a function of temperature, and magnetic field strength

This extreme small differential population of spins between the two states results in a net macroscopic magnetization $\boldsymbol{M}$ in a sample. This net magnetization precesses about $\boldsymbol{B_0}$ at a

frequency given by the Larmor Eq. (2.6). However this magnetization is not readily measurable. In a typical MR experiment, the measurable MR signal is created via the following process.

By convention, direction of external magnetic field $\boldsymbol{B_0}$ is designated as the longitudinal or *z*-axis, and the plane perpendicular to the z axis is often referred to as the transverse or *xy*-plane. Then the *z*-component of magnetization, $\boldsymbol{M_z}$ is tilted away from $\boldsymbol{B_0}$, then the transverse component of magnetization $\boldsymbol{M_{xy}}$ can be measured using an appropriately oriented receiver coil[81]. A commonly used method to tip $\boldsymbol{M_z}$ would be to apply another magnetic field $\boldsymbol{B_1}$ (through radio frequency, RF). If $\boldsymbol{B_1}$ is a magnetic field rotating at the Larmor frequency and applied orthogonal to $\boldsymbol{B_0}$, then the magnetization $\boldsymbol{M}$ precessing at the Larmor frequency experiences a second torque that tilts the magnetization away from the z-axis (*resonance*)(Fig. 2.4).

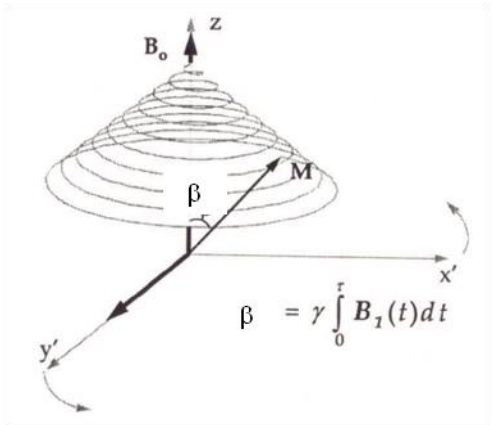

Figure 2.4 Diagram of creation of transverse magnetization. A rotating magnetic flux density B_1 applied for a duration of τ, in the *xy*-plane in the presence of B_0, tips the magnetization vector $\boldsymbol{M}$, through an angle β from the z-aixs. The x' and y' axis are rotating at the Larmor frequency proportional to B_0 as denoted by the arrows. The thin line shows the trajectory of the tip of $\boldsymbol{M}$, following excitation. The measureable component of magnetization is in the transverse plane.

The extent of the tip of the magnetization vector to the transverse plane is often described as the flip angle (β) (Figure 2.4). After $\boldsymbol{B_1}$ is turned off, M_{xy} precessing in the transverse plane induces an *emf* in an appropriately oriented coil. The received signal amplitude decays exponentially as the phase coherence of spins is lost over time due to various relaxation

mechanisms (spin-spin relaxation (T_2) and spin-lattice relaxation (T_1)) [81]. The decaying signal measured immediately following RF excitation is often referred to as Free Induction Decay (FID) (Fig. 2.5). This is the origin of the signal measured in MRI to form an image.

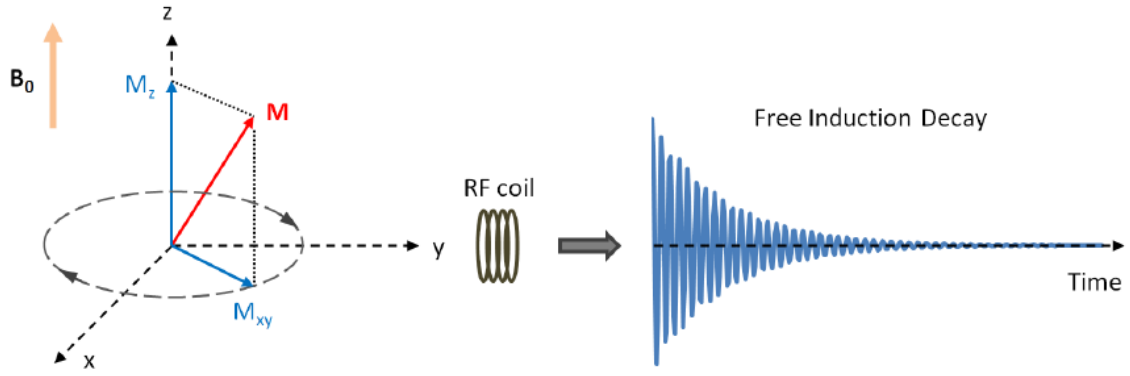

Figure 2.5 Creation of a signal in the RF coil due to the presence of a transverse magnetization M_{xy} rapidly rotating around the z-axis (image courtesy of Thomas Boulet, 2012).

2) Spatial encoding

To resolve spins spatial distribution in a heterogeneous sample, a spectral analysis of the FID can be used based on Larmor Eq. 2.6. It states that the resonance frequency of protons is proportional to the applied external magnetic field. Thus if the strength of the magnetic field is deliberately altered such that the spins at different locations precess at different frequencies, then spatial location of the spins can be obtained by analyzing the received MR signal in spectral domain.

The signal S received by the receiver coils placed outside the sample is the integral sum of the transverse magnetization $\boldsymbol{M_{xy}}$ over the entire volume. For sake of simplicity, the relaxation effects are ignored in the following derivation.

$$S(t) = \int \boldsymbol{M_{xy}}(\boldsymbol{r}, t)d\boldsymbol{r} = \int M_{xy}(\boldsymbol{r})\exp(j\phi(\boldsymbol{r}, t))d\boldsymbol{r} \qquad (2.8)$$

where M_{xy}, and ϕ are the amplitude and phase of transverse magnetization. The process of spatial encoding can be analytically derived from the Larmor equation. Let $\boldsymbol{M}(\boldsymbol{r})$ be the spatial distribution of spins that needs to be resolved, and $\boldsymbol{G_r}$ be the magnetic field gradient along direction $\boldsymbol{r}$, superimposed over the static magnetic field $\boldsymbol{B_0}$. Then the Larmor relationship given by Eq. 2.6 can be rewritten as:

$$\omega = \omega_0 + \omega_G$$

$$= \gamma(B_0 + \boldsymbol{G_r}(t) \cdot \boldsymbol{r}) \tag{2.9}$$

Then spins at different spatial locations along direction $\boldsymbol{r}$, precess at a characteristic frequency ω. So the accumulated phase is

$$\phi(t) = \int_0^t \omega(t) d\tau = \omega_0 t + \gamma \int_0^t \boldsymbol{G_r}(\tau) \cdot \boldsymbol{r} d\tau \tag{2.10}$$

The modulated signal can be obtained by plugging Eq. 2.10 into Eq. 2.8

$$S(t) = \int M_{xy}(\boldsymbol{r}) \exp(j \left(\omega_0 t + \gamma \int_0^t \boldsymbol{G_r}(\tau) \cdot \boldsymbol{r} d\tau \right) d\boldsymbol{r} \tag{2.11}$$

The signal in Eq. 2.11, with demodulating frequency $\Omega = \omega_0$ is rewritten as

$$S(t) = \int M_{xy}(\boldsymbol{r}) \exp\big(j(\boldsymbol{k_r}(t) \cdot \boldsymbol{r})\big) \, d\boldsymbol{r} \tag{2.12}$$

where

$$\boldsymbol{k_r}(t) = \gamma \int_0^t \boldsymbol{G_r}(\tau) d\tau \tag{2.13}$$

Eq. 2.12 has the form of a Fourier transform, where $\boldsymbol{k}$ and $\boldsymbol{r}$ are the conjugate variables. In other words, the integral of the time varying waveform $\boldsymbol{G_r}$ corresponds to traversing the conjugate space, often referred to as ***k-space***.

Thus, magnetic field gradients can be used to traverse *k*-space. If the receiver was open during these traversals, then the received temporal signal corresponds to measurements at those *k*-space locations. Therefore, the Inverse Fourier Transformation (IFT) of the received signal should yield the spatial spins distribution modulated by the spin relaxation parameters and experimental conditions.

In general two-dimensional (2D) MRI acquisition constant magnetic field gradients (G_z, G_y, G_x, applied in *z*-, *y*- and *x*-axis respectively) are commonly used to encode the spatial information. These three gradients also called as slice selection, phase encoding, and frequency encoding gradients respectively.

During slice selection, a spatially varying magnetic field G_z is synchronized with a RF pulse that contains a selected set of frequencies, so that only spins in the sub-volume (one slice) whose Larmor frequencies equal to the frequency (ω) of RF pulse will get excited and tilted to the transverse plane.

$$\omega = \gamma(B_0 + G_z z) \tag{2.14}$$

Then the position of slice get excited can be described as below:

$$z = \frac{\omega}{\gamma G_z} - \frac{B_0}{G_z} \tag{2.15}$$

By changing the ω or G_z, slice at other position can be excited. After MR signal is generated in transverse plane (*xy*-plane), we need to acquire the *k*-space data (k_x, k_y) to get spatial distribution

of spins in the excited plane by IFT. Based on Eq. 2.13, two methods can be used in sampling the 2D *k*-space: either changing the strength or duration of the magnetic field gradient (Eq. 2.16 and 2.17).

$$k_y = \gamma \int_0^{\delta} G_y(\updownarrow) d\tau^{\square} = \gamma G_y(\updownarrow)\delta \tag{2.16}$$

$$k_x = \gamma \int_0^{t} G_x d\tau =^{\square} \gamma G_x t \tag{2.17}$$

In Eq. 2.16, the duration δ of the gradient G_y is *fixed* through the acquisition, while the gradient strength is linearly changed with the sampling order in *y* direction. (k_y: phase encoding). In Eq. 2.17, the strength of gradient G_x is fixed through the acquisition, while the duration varies with the sampling order for each k_x value in *x* direction. (k_x : frequency encoding). After the three encoding steps are finished in a sequence, then the full 2D k-space (k_x, k_y) for each slice is acquired. Then the 2D IFT can be performed to obtain the anatomy information. As for 3D MR acquisition, a 3D k-space (k_x, k_y, k_z) is acquired. In this case, the whole 3D spins will be excited. Following the same principles in acquiring k_y, the k_z data can be obtained by linearly changing gradient strength of G_z in *z* direction. After the full 3D k-space is acquired, the 3D IFT can be performed to get the 3D anatomy information.

The process of spatial encoding of spins discussed above assumed that the spins were stationary. However MR experiments can be designed to provide information regarding tissue motion, diffusion, temperature, etc.

2.2.2.2 MRI Temperature Measurement

Since both characterization of tissue thermal conductivity (Chapter 4) and blood perfusion (Chapter 5) rely on the MRI temperature measurement, a basics of MR temperature imaging (MRTI) sequence is briefly introduced.

Of the many MR parameters that can provide temperature sensitive contrast such as the Apparent Diffusion Coefficient (ADC) of water[82], the spin-lattice relaxation time (T_1)[83, 84], spin-spin relaxation time (T_2)[85], proton density (PD)[86, 87], magnetization transfer (MT)[88, 89], temperature sensitive contrast agent[90-92], and the water Proton Resonance Frequency (PRF)[93, 94] have proven useful for monitoring temperature changes in soft tissue during drug delivery of hyperthermia or thermal therapies. To date, the most exploited and widely validated quantitative MRTI techniques are still based on PRF because of two major benefits[95]: 1) the shift of the PRF is proportional to temperature over a large range of temperatures (15~100^{o}C)[93] with a sensitivity of -0.01ppm/^{o}C; and 2) it is also insensitive to tissue type with a range of approximately -0.0096 to -0.0113 ppm/^{o}C in tissue. We will focus on the PRF method for measuring temperature evolution in this dissertation.

The physical basis for the temperature dependence of PRF is that the temperature rise leads to a corresponding increase in molecular Brownian motion that bends, stretches, and breaks hydrogen bonds between local water molecules. The decreased net hydrogen bond strength results in an increase in the strength of the covalent bond between the water protons and oxygen, which better shields the proton from the external magnetic field and changes the proton shielding constant ($\Delta\sigma$). This results in a resonance frequency shift (Δf) of the proton[93, 96]. The frequency shift is an approximately linear with temperature (ΔT)[97, 98]

$$\Delta f = \frac{\gamma}{2\pi}\Delta \mathrm{B} \cong -\frac{\gamma}{2\pi}B_0\left(\Delta\sigma + \frac{2}{3}\Delta\chi\right) \cong \frac{\gamma}{2\pi}B_0\alpha\Delta T \qquad (2.18)$$

where α [ppm/^{o}C] is temperature sensitivity coefficient and is primarily representative of the changes in the shielding constant ($\Delta\sigma$) with some contribution from changes in bulk susceptibility due to temperature ($\Delta\chi$). B_0 is the static external main magnetic field.

Based on Eq. 2.10, the phase change ($\Delta\phi$) due to the temperature change after demodulation of ω_0 can be written as follows

$$\Delta\phi(r,t) = \int_0^{T_E} 2\pi\Delta f(r,t)d\tau = \gamma B_0 \alpha T_E \cdot \Delta T(r,t) \tag{2.19}$$

where T_E is the echo time when MRTI reads the temperature. Therefore temperature change can be measured through relating the difference in phase between two dynamics as below

$$\Delta T(r,t) = \frac{\Delta\phi(r,t)}{\gamma\alpha B_0 T_E} \tag{2.20}$$

A typical MRTI sequence used to measure temperature is a gradient echo based (Fig. 2.6).

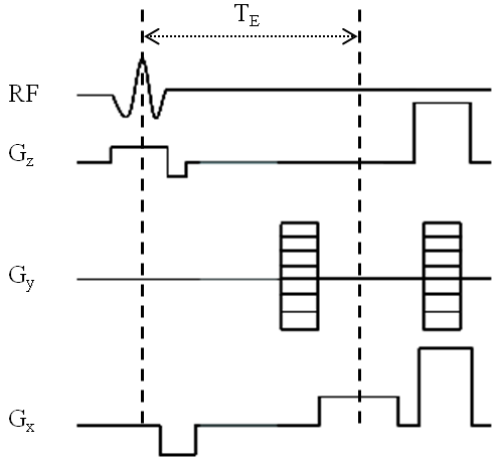

Figure 2.6 Diagram of typical MR pulse sequence for measuring temperature. A small flip angle (<30^{0}) RF pulse synchronized with a slice selection gradient G_z is used to excite magnetization in the selected slice into transverse plane to create transverse magnetization. A phase encoding gradient G_y and frequency encoding gradient G_x will be applied after slice selection gradient to do a 2D spatial encoding.

The phase images $\phi(r, t)$ at different time points will be acquired during thermal therapy using above sequence. The $\phi(r, 0)$ will be acquired before heating to serve as a background phase in order to calculate phase change due to temperature rise during therapy. The reference temperature (T_{ref}) is assumed to be body temperature. From Eq. 2.20, the absolute spatial-temporal temperature distribution can be calculated as follows

$$T(r,t) = \frac{\phi(r,t) - \phi(r,0)}{\gamma \alpha B_0 T_E} + T_{ref} \tag{2.21}$$

2.2.2.3 MRI Displacement Measurement

In this section, the use of MRI to measure displacement introduced by applied stress is going to be reviewed for the purpose of measuring tissue mechanical properties in Chapter 6. MRI has been firstly used to directly visualize the propagation of acoustic strain waves by spatially mapping displacement patterns corresponding to mechanical introduced motion[99], known as MR Elastography (MRE). It has then been widely used to measure the shear stiffness of soft tissues[100-108].

The spin in a magnetic field accumulate a phase that is dependent on both the strength of static main magnetic field and the applied magnetic field gradient along the direction of the spin motion[109] as shown in Eq. 2.9 and 2.10.

$$\begin{aligned} \phi(\boldsymbol{r},t) &= \int_0^t \gamma\big(B_0 + \boldsymbol{G}(\boldsymbol{r},\tau)\cdot\boldsymbol{r}(\tau)\big)d\tau \\ &= \gamma\int_0^t B_0 d\tau + \gamma\int_0^t \boldsymbol{G}(\boldsymbol{r},\tau)\cdot\boldsymbol{r}(\tau)d\tau \end{aligned} \tag{2.22}$$

To encode the spin motion, in addition to conventional spatial encoding gradients, a new gradient $\boldsymbol{G}(\boldsymbol{r}, t)$ known as motion encoding gradient (MEG) is introduced. The 1st term in the above Eq. is a constant, since B_0 is time invariant and does not reflect information about spin motion. It is the 2nd term that is of interest in motion detection. The spin motion vector can be further expanded as a Taylor's series to probe motion of higher order like velocity, acceleration jerk, etc.

$$\boldsymbol{r}(t) = \boldsymbol{r}_0 + \boldsymbol{v_0}t + \frac{1}{2}\boldsymbol{a_0}t^2 + \cdots \tag{2.23}$$

Inserting Eq. 2.23 to Eq. 2.22,

$$\phi(\boldsymbol{r}, t) = \boldsymbol{r_0} \cdot \gamma \int_0^t \boldsymbol{G}(\boldsymbol{r}, \tau)d\tau + \boldsymbol{v_0} \cdot \gamma \int_0^t \boldsymbol{G}(\boldsymbol{r}, \tau)\tau d\tau + \frac{1}{2}\boldsymbol{a_0} \cdot \gamma \int_0^t \boldsymbol{G}(\boldsymbol{r}, \tau)\tau^2 d\tau$$

$$= \boldsymbol{r}_0 \cdot \boldsymbol{M_0} + \boldsymbol{v_0} \cdot \boldsymbol{M_1} + \boldsymbol{a_0} \cdot \boldsymbol{M_2} + \cdots \tag{2.24}$$

Where $\boldsymbol{r_0}$, $\boldsymbol{v_0}$, and $\boldsymbol{a_0}$ are the zeroth, first and second derivatives of the position vector at time $t = 0$ corresponds to position, velocity and acceleration respectively, and $\boldsymbol{M_0}$, $\boldsymbol{M_1}$ and $\boldsymbol{M_2}$ are the zeroth, first, and second temporal moments of the gradient waveform. Therefore it is possible to encode individual components of spin motion with an appropriate MEG waveform. In other words, the zeroth moment of a gradient encodes the spatial position of the spins, while a gradient with a finite first moment $\boldsymbol{M_1}$ encodes the velocity component of spin motion, which has been used in measuring blood flow[109] and suppressing artifacts caused by physiologic motion by selectively nulling the temporal moments of the gradient waveform[110].

Two types of motion (cyclic and transient) will be addressed in this section:

1) Magnetic resonance imaging of cyclic motion

The motion caused by a cyclic applied stress on the tissue introduces a temporal spin motion vector as shown below[99]:

$$\boldsymbol{r}(t) = \boldsymbol{r}_0 + \boldsymbol{\xi}_0 \exp[j(\boldsymbol{k}\cdot\boldsymbol{r} - \omega t + \theta)] \tag{2.25}$$

where $\boldsymbol{r}_0$ is the mean position and $\boldsymbol{\xi}_0$ is the displacement amplitude of the spin from its mean position. ω is the angular frequency of mechanical wave, $\boldsymbol{k}$ is the wave number, θ is the initial phase offset of the wave. Then the dynamic phase shift of the moving spin can be obtained by inserting Eq. 2.25 into Eq. 2.22:

$$\phi(r,\alpha) = \gamma \int_0^{\tau=NT<T_E} \boldsymbol{G}(r,t')\cdot\boldsymbol{\xi}_0 e^{j(\boldsymbol{k}\cdot\boldsymbol{r}-\omega t'+\alpha)}dt' + \gamma \int_0^{\tau=NT<T_E} \boldsymbol{G}(r,t')\cdot\boldsymbol{r}_0 dt' \tag{2.26}$$

where N is the number of MEG cycles, $T = 2\pi/\omega$ and $\boldsymbol{G}$ is the applied motion encoding gradient. By properly choosing the waveform of MEG, where $\boldsymbol{M}_0 = 0$, the second term in Eq. 2.26 is then zero. For example MEG with multiple bipolar pairs N, duration τ, and the switching frequency same as mechanical motion:

$$\boldsymbol{G}(r,t) = \begin{cases} +\boldsymbol{G}_0; & t \in [nT, (2n+1)T/2] \\ -\boldsymbol{G}_0; & t \in [(2n+1)T/2, (n+1)T] \end{cases} \tag{2.27}$$

where n = 0, 1, 2, 3, ..., N-1. $\boldsymbol{G}_0$ is the gradient strength amplitude in [10^{-3}T/m]. To simplify the analysis, the ramp times of MEG are negligible. Then the Eq. 2.26 becomes[99]:

$$\phi(r,\alpha) = \frac{2\gamma NT(\boldsymbol{G_0}\cdot\boldsymbol{\xi}_0)}{\pi} sin(\boldsymbol{k}\cdot\boldsymbol{r}+\theta) \tag{2.28}$$

By analyzing the Eq. 2.28, following constructive result can be made for cyclic motion:

i) The phase shift of the received MR signal is directly related to the mechanical wave propagation in the tissue (wave vector $\boldsymbol{k}$, displacement amplitude vector ξ_0, and initial wave phase θ), which provides a potential tool for investigating the tissue mechanical properties which governs the wave propagation in the tissue.

ii) The measured phase shift is proportional to the displacement amplitude vector, MEG amplitude, and number of cycles of MEG. This makes measuring the micro and sub-micron motion feasible by increasing the gradient strength of MEG or number of cycles of MEG.

iii) The scalar product between the gradient vector and the displacement amplitude vector assures that it is feasible to measure the motion of any direction by superimposing MEG in corresponding direction.

iv) The dependence of the phase shift on the initial phase offset α between the MEG and the mechanical excitation provides a tool to temporally study the behavior of spin motion or wave propagation by dynamically changing the phase offset θ. This also paves a way to study the wave propagation in frequency domain instead of the time domain which will simplify the analysis[111].

2) Magnetic resonance imaging of transient motion

The phase shift introduced by transient motion $\boldsymbol{r}(t)$ can be generally written as below based on Eq. 2.26 ignoring irrelevant term to motion

$$\phi = \int_0^{\tau} \gamma \boldsymbol{G}(\boldsymbol{r}, \tau) \cdot \boldsymbol{r}(\tau) d\tau \tag{2.29}$$

Approximating the MEG waveform as a square wave of duration τ and amplitude $\boldsymbol{G_0}$ for simplicity of theory description, the accumulated phase shift is proportional to the average position $\overline{\boldsymbol{r}}$ during the motion encoding time[112].

$$\phi = \gamma\tau \boldsymbol{G}_0 \cdot \overline{\boldsymbol{r}} \tag{2.30}$$

If the motion encoding gradient is applied along the direction of spin motion, the accumulated phase shift can be rewritten in simplified form

$$\phi = \gamma\tau G_0 \overline{r} \tag{2.31}$$

Then the average position can be calculated as following

$$\overline{r} = \frac{\phi}{\gamma\tau G_0} \tag{2.32}$$

Therefore, the displacement as a function of time introduced by transient motion can be estimated using Eq. 2.32 by varying the time delay between the onset of the MEG and the start of the transient mechanical excitation. The tissue elasticity can then be calculated by deducing the wave velocity from the introduced shear wave propagation.

2.2.3 High Intensity Focused Ultrasound

Ultrasound is a pressure wave with a frequency above the audible range of a human ear (18-20 kHz); it is generated by a mechanical motion that induces the molecules in a medium to oscillate around their rest positions (Fig. 2.7A). Due to the bonding between the molecules, the disturbance is transmitted to the neighboring molecules. The motion causes compressions and rarefactions of the medium and thus a pressure wave travels along with the mechanical

disturbance (Fig. 2.8B). In most cases, the molecules vibrate along the direction of the propagation (known as longitudinal or compression wave), but in some instances, the molecular motion is across the direction of the wave propagation (shear wave). Since the shear waves quickly attenuated in solids such as bone, most current medical ultrasound methods utilize longitudinal wave to diagnosis disease or ablate tumor tissue.

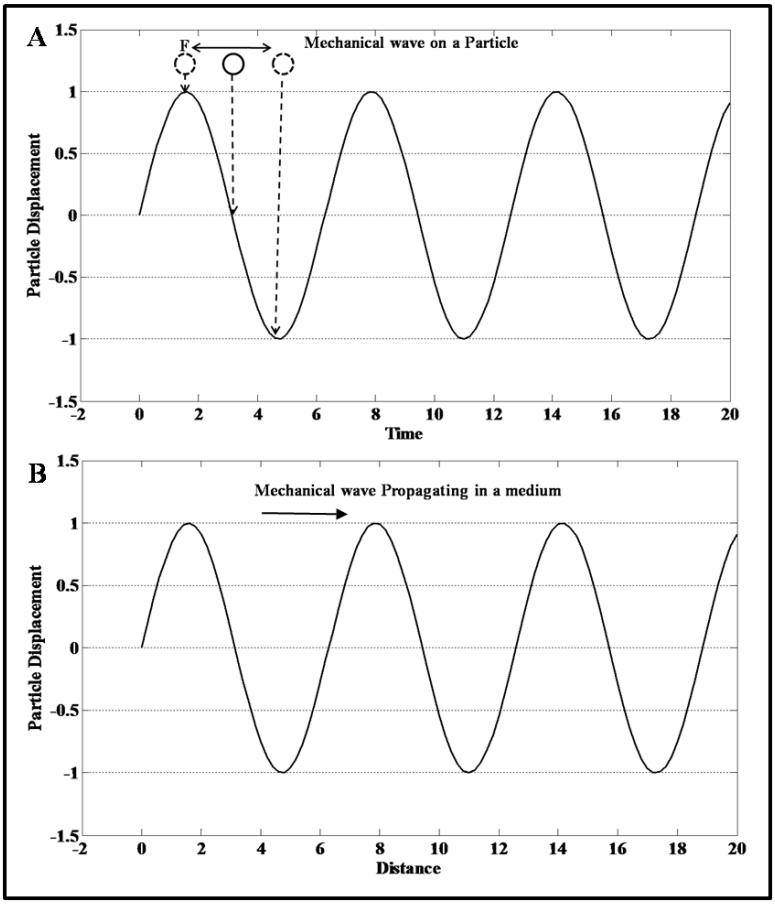

Figure 2.7 diagram shows the particle motion in a shear wave created by mode conversion of an ultrasound wave as function of time (A) and the particle motion in a medium where the shear wave is propagating as function of spatial location (B).

The ultrasound is normally generated by applying radiofrequency (RF) voltage across a piezoelectric material that expands and contracts in proportion to the applied voltage. The generated ultrasound field distribution depends on the size, shape, and frequency of the vibration

source. If the diameter of an ultrasound source is much larger than the wavelength in the medium, the ultrasound wave can be focused by lenses[113] or reflectors[114] or by making the transducer self-focusing[115] (Fig. 2.8). The acoustic intensity at the focus could be as ten times as much high of the 1st side lobe in that ultrasound field.

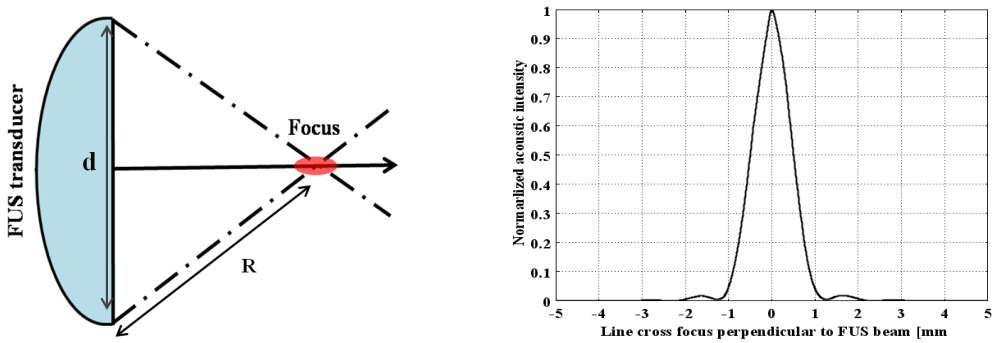

Figure 2.8 A diagram of a self-focusing spherically curved ultrasound transducer (Left) and the simulated line profile of acoustic intensity normalized to the peak across the focus and perpendicular to the FUS beam diection.

The geometrical focuse of this single element transducer is often described as a F-number, which is the ratio between the radius of curvature (R) and the diameter (d) of the transducer:

$$F = \frac{R}{d} \tag{2.33}$$

By increasing the radius of curvature (R), the focus can be pushed deeper into the tissue but at the cost of the focal region becoming longer and the lower peak intensity due to the reduced focusing effect of the transducer and also the attenuation in the tissue.

An alternative to single element transducer is the phase-array, multi-element transducer in which individual elements are driven with RF-signals having each specified delays (phase) and amplitude to obtain a desired focal point (electrical focusing, Fig. 2.9). An ultrasound beam can be focused anywhere in front of the array when the element center-to-center spacing is wavelength/2 or smaller[116]. This provides the ability to electronicly steer the focal point or

simultaneously create multiple focal points of ultrasound field by appropriately adjusting the phase of the electrical signal for each piezoelectric element.

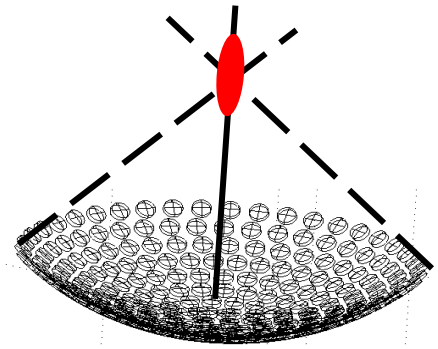

Figure 2.9 A diagram of a spherical phase-array electronic focusing transducer.

2.2.3.1 Current Clinical Thermal Ablation with HIFU

The thermal effects of focused ultrasound were initially used to induce highly localized coagulation of tissue in target [117, 118]. The transducers used in earlier HIFU surgery were single-element spherical shell transducers that allowed for ablation of a single elliptical focal region with a diameter on the order of a wavelength (a few millimeters when operated at frequency of MHz range). By mechanically moving the transducer, a larger volume can possibly be treated[119, 120]. This traditional techinique progressively heated single focal point at a time until all the target volume is treated with each sonication followed by a cooling period to decrease the temperature accumulation in the healthy tissue located in both near and far field path of ultrasound beam (Fig. 2.10). The treatment efficiency of this *point-by-point* ablation technique is hampered by energy dissipation due to heat conduction and convection near the focus.

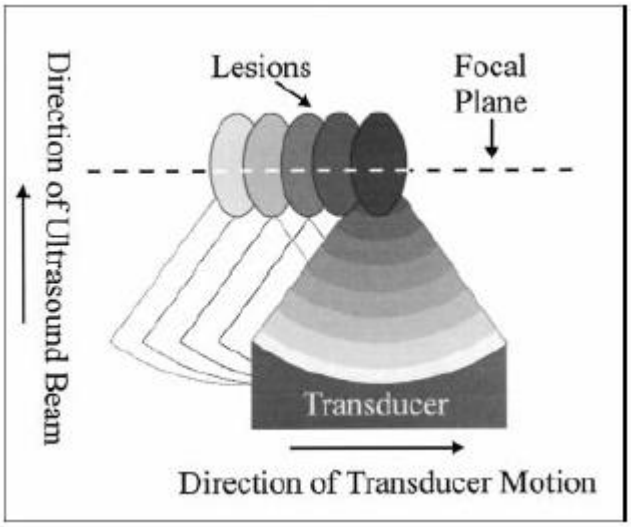

Figure 2.10 Diagram shows the point-by-point sonication. Image courtesy of McDannold, Radiolog, 1999.

Recent developments in the design of MR-compatible phase-array transducers has allowed rapid ablation of a larger volume than the focal point without need to mechanically move the transducer through two ways: 1) Simultaneously heating multiple local region by splitting the natural focus into multiple foci[121-123]; and 2) Continuely sonicating local region by temporally switching predetermined multi-foci patterns[124, 125].

While the large volume of heating achieved by multi-foci heating (or split-focus) is technically feasible, this approach can cause unintended heating due to high-energy content in the side lobes. To overcome this issue, a new volumetric heating strategy have been proposed[72]. In this volumetric HIFU heating, a single focus is electronically steered along a predefined trajectory, e.g., multiple outward-moving concentric circles placed in the plane (treatment plane) perpendicular to the direction of HIFU beam and centered on the axis of propagation[126] (Fig. 2.11). By heating several pre-defined focal points at regularly positioned intervals on the trajectory, a relatively large volume could be treated. The spatial location of the focus on the trajectory, and the temporal interval between heating successive points is carefully controlled to

minimize the loss of thermal energy due to conduction and convection – an issue with heating using a fixed focus transducer.

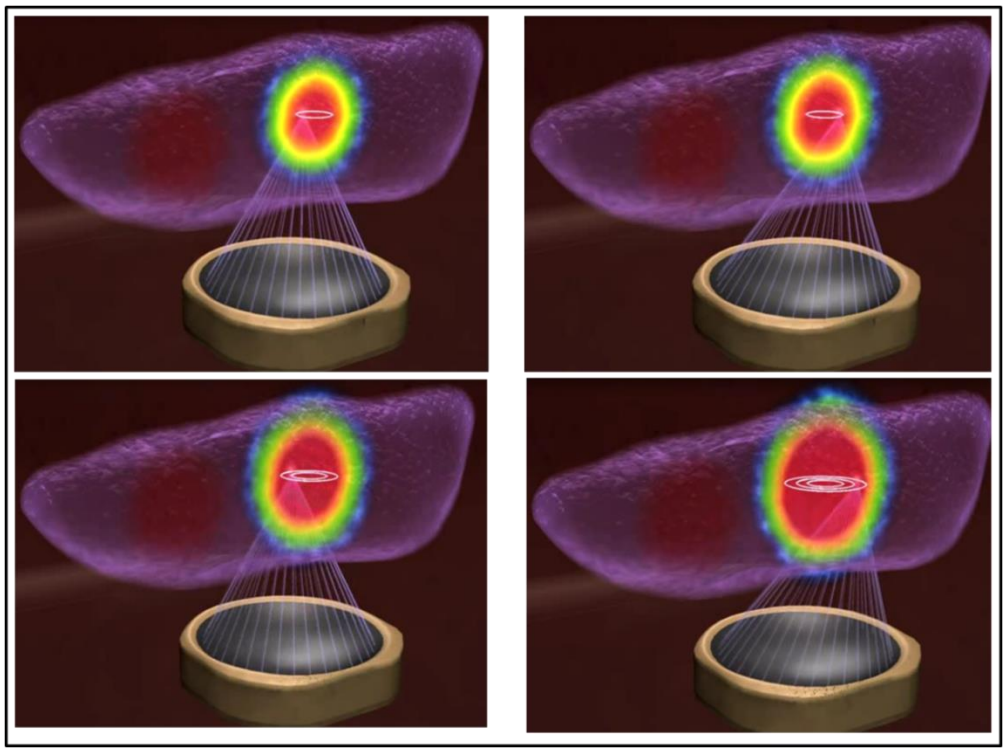

Figure 2.11 Diagram shows the volumetric sonication. Image courtesy of Philips Healthcare.

As an example, Köhler et al describe a circular sonication trajectory in which the temporal interval between successive focal points was 50ms, with near instantaneous switching between the points (a few microseconds)[72]. The sonication order of these locations was chosen such that the radial coordinates corresponded to a constant jump in phase between any two successive points:

$$\Delta\varphi = \frac{2\pi}{N_p}\left(\frac{N_p}{2} - 1\right) \tag{2.34}$$

where, N_p was the number of focal point on the circle (a multiple of 4). There were total four sonication circles (diameter: 4mm, 8mm, 12mm, and 16mm) available in this volumetric

sonication algorithm with different pre-defined number of focal points on these four circles (N_p = 8, 16, 24 and 32 respectively).

The sonication order of these locations was chosen to maximize the distance between successive points, which in radial coordinates corresponded to a constant jump in phase between any two successive points of

$$\Delta\varphi = \frac{2\pi}{N_p}\left(\frac{N_p}{2} - 1\right) \tag{2.34}$$

where N_p was the number of focal point on the circle (multiple of 4). There were total four sonication circles (diameter: 4mm, 8mm, 12mm, and 16mm) available in this volumetric sonication algorithm with different pre-defined number of focal points on these four circles (N_p = 8, 16, 24, and 32 respectively). Such volumetric heating strategies make it possible to spread the expended thermal energy via diffusion to ensure uniform heating over the entire volume.

The size of sonication volume encompassed by the predefined trajectory is referred to as a cell, e.g., a volume encompassed by a trajectory of 4-mm diameter circle is referred to as a 4-mm cell. A volume of 8-mm cell was performed by adding one more 8-mm diameter circle to the 4-mm cell. So 12-mm and 16-mm cell were composed of three circles (diameter: 4mm, 8mm, and 12mm) and four circles diameter: 4mm, 8mm, 12mm, and 16mm) respectively. This terminology for cell dimension will be used throughout the dissertation.

The sonication time for each circle depended on the size of the cell and the operation frequency and ranged from 20s for a 4 mm treatment cell to about 70 s for a 16 mm treatment cell at 1.2 MHz. Sonication of the focal point locations at each circle was repeated until the sonication time of that circle was reached, and then the locations of the next circle were to be sonicated. The sonication ended once the last circle in the trajectory was sonicated. The sonication duration in this algorithm was optimized off-line [126] based on a simulation of tissue temperature change by Penne's bio-heat transfer equation[127] with assumptions of all tissue

thermal and physiological parameters temperature independent. However, this algorithm may result in overheating target tissue due to the inhomegenity of tissue and also result in heat deposition in non-target region due to the prolonged sonication time compared to the point-by-point heating stratagem. An improved feedback algorithm was recently developed to be used together with this high efficiency volumetric ablation method[128]. It was implemented by adjusting the duration of the concentric ablation circles within the target volume to reach an optimal temperature and necrosis dosage level based on the real-time MRI measured temperature distribution (Fig. 2.12). The sonication was stopped when the outermost sub-trajectory has reached its target temperature or alternatively all voxels in the entire intended volume have reached a thermal dosage of causing necrosis.

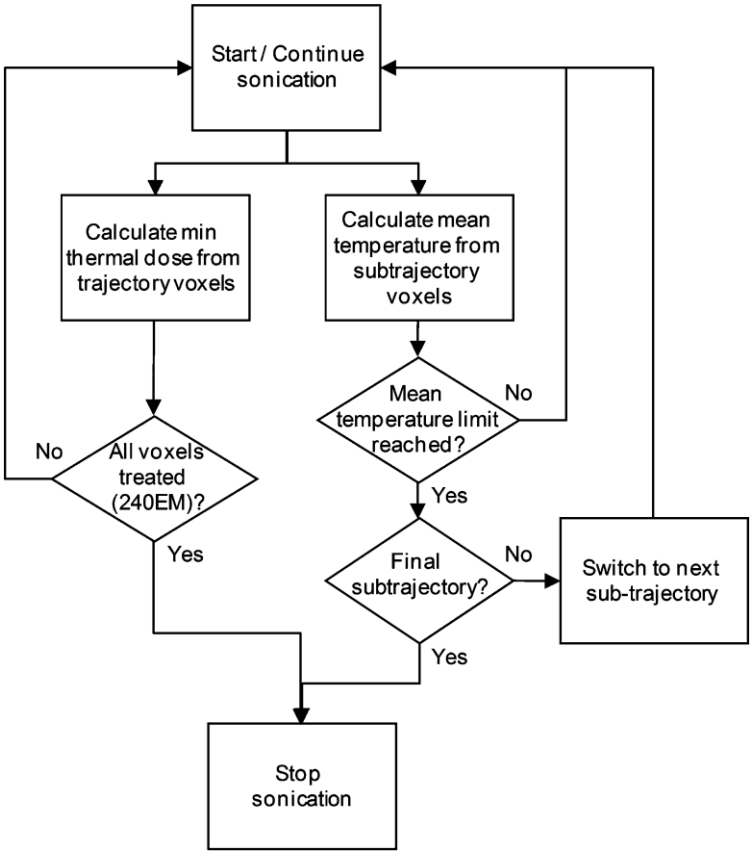

Figure 2.12 Diagram illustration of the improved feedback algorithm with volumetric ablation technique. Image courtesy of Enholm's paper, 2010.

Enholm et al demonstrated in animal studies, that the standard deviation of the diameter was reduced by factors of 1.9, 7.2, 5.0 and 3.4 for 4-, 8-, 12-, and 16-mm cell and thus improved the reproducibility of the induced lesion size. Energy efficiency of this algorithm was also improve since less energy used to create the desired lesion[128].

2.2.3.2 Mechanical Effect from HIFU

In addition to the clinical utilization of thermal effect of HIFU, its mechanical effect, originated from the momentum transfer from the ultrasound wave to the medium, has been studied in tissue elasticity characterization[129], which is related to the pathological information and visualizing HIFU focal spot[130, 131]. The radiation force F (N/m^3) introduced from the mechanical effect of ultrasound (ARF) is dictated by the ultrasound absorption coefficient α (m^{-1}), speed of ultrasound c(m/s) and the local acoustic intensity I (W/m^2) [132, 133] in the tissue (as shown in Eq. 2.1).

$$F = \frac{2\alpha I}{c} \tag{2.35}$$

The acoustic radiation force (ARF) is highly directional and localized at the HIFU focus. ARF outside the focus is at least an order of magnitude smaller than at the focus [112]. ARF initiates mechanical a wave that propagates both in longitudinal (compressional) mode and in transverse (shear) mode (Fig. 2.13).

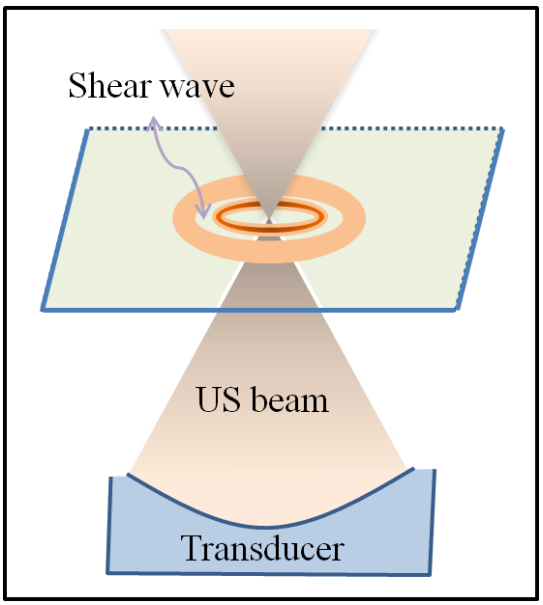

Figure 2.13 Cartoon illustrations of the transient shear waves generated by acoustic radiation force.

The transient impulse displacement *r* at the focus introduced by HIFU beam may be modeled as an over-damped oscillator response [134].

$$r(t) = \begin{cases} 0; & t \le 0 \\ \frac{F}{k}\left(1 - e^{-\frac{t}{\tau}}\right); & 0 \le t \le T \\ r(t)|_{t=T} \cdot e^{-\frac{t}{\tau}} & ; t > T \end{cases} \tag{2.36}$$

Here *k* is a proportionality constant relating ARF and displacement, and τ is the time constant of the transient response. *T* is the duration of ultrasound burst. Both *k* and τ depend on the tissue visco-elastic properties and the spatial distribution of ARF. The generated shear wave resulted from the disturbance of ARF in the focal spot has been experimentally observed by optical[135, 136], ultrasound[137, 138], and MRI[129, 139] techniques.

The use of ARF to generate shear wave is expected to provide several advantages. First, it is possible to generate shear wave directly inside the tissue of interest by positioning the focus of the transducer at the desired location by a combination of mechanical and/or electrical steering

focus of the transducer. Second, the desired penetration can be achieved by the choice of an appropriate central frequency of the ultrasonic waves. For most clinical applications, to achieve a depth of penetration in the range of several centimeters the transducer frequency is chosen to be on the order of few hundred kHz to low MHz regime. A notable exception is in the treatment of prostate cancer which uses high frequency probes (on the order of 4-6 MHz to target tissues very close to the transducer surface. Third, such low frequency longitudinal waves penetrate within the body with little attenuation and easily reach the focal plane with sufficient intensity to generate a shear wave. Fourth, the directionality of the force is known *a priori*, facilitating the choice of the direction of the MEG.

However, use of ARF is also fraught with issues that may concern patient safety due to heating and potential for cavitation induced tissue damage[140]. A short ultrasound burst can be used to drastically reduce tissue heating compared to continuous excitation[129] while a transient shear wave can still be generated in deep tissue. The latter aspect is particularly interesting as it helps to partially overcome the challenges faced by conventional MRE due to reflection, refraction, and attenuation of mechanical waves coupled into the body from the surface [141]

Chapter 3

Limitations and Quality Assurance of Volumetric MR-HIFU Measurements

3.1 MR-HIFU Validation: Accuracy and Precision

In this chapter, we address the fundamental issues related to the accuracy and precision of the MR-HIFU system used in this work, in delivering a prescribed thermal dose to a pre-defined region within the body. We also address the issues concerning the accuracy and precision of MR temperature measurement. The quality assurance of this system was analyzed in phantom, *in-vivo* pig model and in human uterine fibroid *in-vivo*. The limitation of the MR-HIFU system, example the effect of spatial resolution on temperature and thermal dose measurement, will be addressed.

MRI thermometry for HIFU

The optimized MRTI sequence for clinical MR-HIFU surgery was as following. Real time multi-plane temperature images were acquired using a multi-shot echo-planar imaging (EPI) technique with the acquisition parameters: repetition time (TR) = 37ms; echo time (T_E) = 20ms; flip angle (FA) = 20 º; voxel size = 2.5×2.5×7 mm^3; matrix size = 160×99; field of view (FOV) = 400×248 mm; EPI factor = 11; and a 1-2-1-binomial water selective excitation pulse for suppressing fat signal. A total of 6 slices of 7mm each were prescribed to monitor temperature elevation during sonication (Fig. 3.1) based on the temperature-dependent proton resonance frequency (PRF) shift of water[142] and Eq. 2.21. Three of the 5 coronal slices with a 0-mm inter-slice gap, stacked in the coronal plane perpendicular to the ultrasound beam axis, automatically bisected the focal ellipsoid. One sagittal slice (parallel to the ultrasound beam axis) was also

automatically positioned to allow visualization of heating in the long axis of the ellipsoid. The two remaining coronal slices were placed in the near and far field of ultrasound beam to monitor any unintended temperature elevation near critical structures outside the ablation zone.

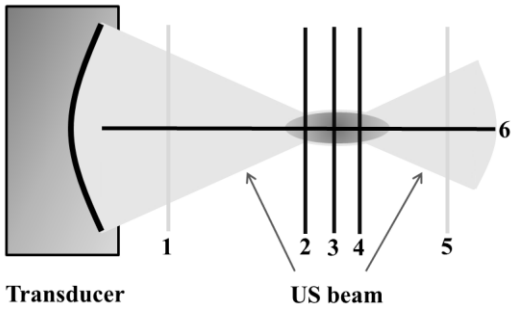

Figure 3.1 Relative positions of the six slices used for real-time monitoring temperature elevation.

The total acquisition time for all 6 slices was 2.9 seconds per dynamic i.e. temporal resolution is 2.9s. The uncertainty of temperature measurement (σ_T) is inversely related to the signal-to-noise ratio (SNR_M) of the MR magnitude image, given by[119]:

$$\sigma_T = \frac{1}{\alpha\gamma T_E B_0} \cdot \frac{1}{SNR_M} \tag{3.1}$$

where α is the PRF coefficient for aqueous tissue, γ is the gyromagnetic ratio, B_0 is the main magnetic field, and T_E is the echo time. Temperature information was overlaid only on pixels with a SNR_M of >4.5 (which corresponds to a temperature measurement uncertainty σ_T of <3 ℃) during HIFU heating. The baseline drift in temperature maps was corrected by measuring the average temperature changes in pixels that were at least 30mm away from focal spot and that had a σ_T of <3 ℃[143].

Tissue damage was then real time estimated by thermal dose (*TD*) defined at equivalent minutes (EM) at 43^{o}C using the Sapareto-Dewey equation[13] based on the dynamic temperature maps.

$$TD(t) = \int_0^t R^{T-43} dt' \tag{3.2}$$

Where R is equal to 2 if $T(t) \geq 43^{o}C$ and 4 if $T(t) < 43^{o}C$. The dead tissue volume was quantified as the volume including voxels of a thermal dose above 240 EM – a threshold that is widely considered to result in tissue necrosis [126].

MR-HIFU experimental setup of phantom model

All sonications performed in phantom study were used to analyze the accuracy and precision related to heating and were implemented on Philips clinical HIFU system (Sonalleve™, Philips Medical Systems, Vantaa, Finland) integrated with a 1.5T MRI scanner. This system consisted of a 256-element spherical-shell phased-array transducer of 12-cm radius of curvature and 13-cm aperture, radiofrequency generator cabinet, workstation for therapy control, and integrated 3-element MRI receiver coil suitable for imaging. One of the receive coil elements is located around the acoustic window in the table top, and the other 2 coil elements are enclosed in a freely movable, curved, rigid plastic container that was strapped on top of the phantom. The ultrasound propagated out of the water bath and passed through an acoustic window in the HIFU table top. Acoustic coupling between HIFU agar phantom (mixture of agar and 2% silica) and acoustic window was ensured by placing an aqueous, bacteriostatic, disposable standoff pad (Aquaflex®; Parker Laboratories, Fairfield, New Jersey, USA). Degassed water was added to both sides of the pad to further improve coupling at the interfaces (Fig. 3.2).

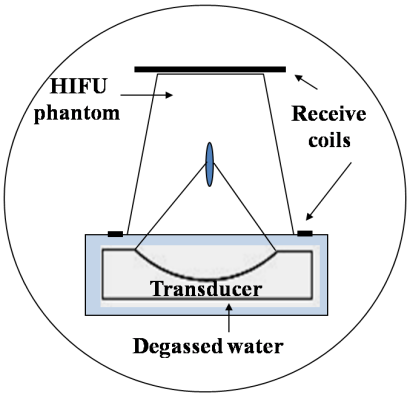

Figure 3.2 Schematic drawing of the clinical HIFU platform

MR-HIFU experimental setup of in-vivo pig model

1) Animal protocol

The animal study for both MR-HIFU system quality assurance analysis and characterization of both tissue thermal conductivity (Chapter 4) and blood perfusion (Chapter 5) was performed in two Institutions. Both facilities used the same experimental procedures and the same hardware and software configurations[144]. The protocol was approved by respective Institutional Animal Care and Use Committees. A total of 4 healthy pigs (body weight, 50 to 65 kg) were treated in this study. Three of the pigs were treated at our institution, and the other animal was treated at another institution in Finland. We created thermal lesions in both hind thigh muscles of the 4 pigs. To facilitate propagation of the HIFU beam through the skin, each hind leg was shaved and any remaining hair was removed with hair-removal cream (Nair). Each pig was sedated by injecting telazol (4 to 6 mg/kg) and atropine sulfate (0.02 to 0.05 mg/kg) intramuscularly. The animal was then moved into the MRI scanner and was placed in either the right or left decubitus position on top of the HIFU device. To avoid unwanted motion during HIFU sonication, the pig was further sedated throughout the procedure by means of a propofol drip (180 mL/hour). The animal's body temperature and cardiac frequency were monitored with a

rectal temperature probe and vectorcardiography respectively. At the end of the MR-HIFU session, the pig, which was under deep anesthesia, was euthanized with an intravenous injection of a lethal dose of potassium chloride (60 to 90 mEq), per institutional guidelines.

2) Experiment setup

All HIFU sonications in *in-vivo* pig study were performed using same clinical MR-HIFU system as used in the phantom study. One of the total three receive coils element was still located around the acoustic window in the table top, and the other two coil elements were enclosed in a freely movable, curved, rigid plastic container that was strapped on top of the animal instead. Acoustic coupling between HIFU acoustic window and the pig's leg was ensured by placing a gel pad. A mixture of ultrasound transmission gel and degassed water was added to both sides of the gel pad (aqueous standoff bacteriostatic disposable Aquaflex®, Parker Laboratories, Fairfield, NJ) to further improve coupling at the interfaces (Fig. 3.3).

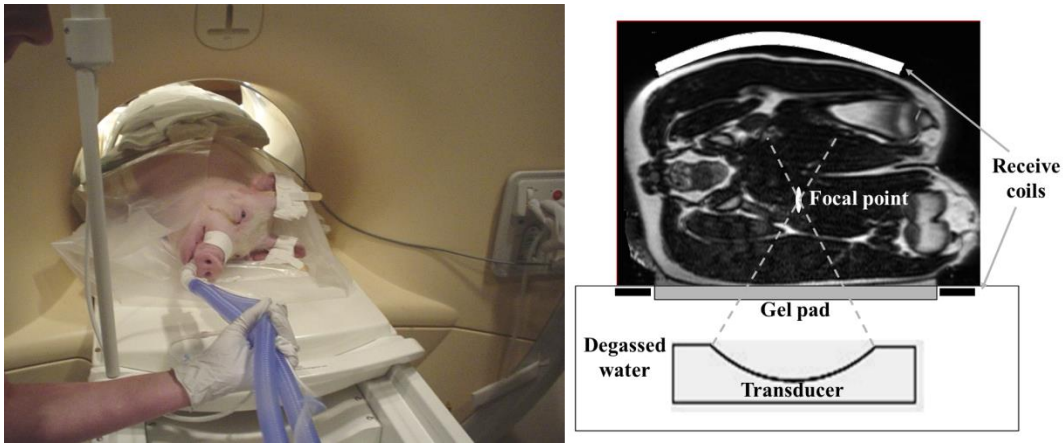

Figure 3.3 Real picture (Left) and schematic drawing (Right) of the *in-vivo* pig HIFU experiment setup

The same MRTI protocol was used to monitor the temperature evolution as in the phantom study.

MR-HIFU experimental setup of in-vivo uterine fibroid model

1) Patient enrollment

This study was approved by the institutional review board of St Luke's Episcopal Hospital (Houston, TX, US) and written informed consents for the MR-HIFU uterine fibroid surgery were obtained from all patients; however, the requirement of patient consent for tissue properties characterization was subsequently waived because of its retrospective nature of this post-process. From August 2009 to March 2013, five women with symptomatic uterine fibroids (mean age, 47 years; range, 42–54 years) were treated using MR-HIFU surgery procedure. Inclusion criteria were as follows: *(i)* pre-menopausal or peri-menopausal women aged 18– 59 years and weight less than 140kg; *(ii)* transformed symptom severity score (ie, subset of uterine fibroid symptoms and quality of life) of 40 or greater[145] ; *(iii)* diameter of dominant fibroid is greater than 3 cm and less than or equal to 12 cm; *(iv)* not currently pregnant or with any plans for future pregnancy; *(v)* no contraindications to MR imaging or MR imaging contrast agent; *(vi)* no evidence of calcification or degeneration in the uterine fibroid at conventional radiography or MR imaging[146]; and *(vii)* signal intensity of fibroid is not higher than myometrium in T_2w MR images. Exclusion criteria were: *(i)* presence of other pelvic diseases, such as endometriosis, ovarian tumor, acute pelvic diseases, or important systemic disease; *(ii)* scar tissue or surgical clip in the direct path of the HIFU beam; or *(iii)* fibroids not quantifiable at MR imaging (in terms of number and volume measurements[70].

2) Experiment setup

All procedure for *in-vivo* uterine fibroid HIFU treatment was performed on an outpatient basis by one experienced interventional radiologist. After HIFU treatment, MR temperature

measurements were transferred to an off-line computer to estimate tissue thermal conductivity (Chapter 4) and blood perfusion behavior (Chapter 5). A catheter was inserted just before the treatment for injecting contrast agent right after treatment to evaluate the treatment outcome. Patients were instructed to lie in a prone position with an acoustic coupling to the acoustic window of HIFU tabletop achieved by gel pad same as used in animal study and a small amount of degassed water (Fig. 3.4, Left). The specific designed pelvic receive coils for MR abdomen imaging were put on top of the butt of the patients to receive MR signal. The body temperature was taken after the patient was set up inside the scanner. The patient was instructed to try to stay as still as possible during the whole process of treatment. One research nurse stayed inside the scanner room with patients to convey the thermal ablation procedure and ensured patient comfort. The patient was also instructed that she is free to stop the treatment using the patient safety device if for any reason, she felt abnormal heating (Fig3.4, middle). The 3D anatomic acquired MRI images were then sent to HIFU therapy console for operator to plan the target region in fibroid tissue (Fig 3.4, right). Two transparent yellow cone regions showed near field and far field region of HFIU beam. The red region showed the target fibroid region. The transducer is shown at the bottom in yellow.

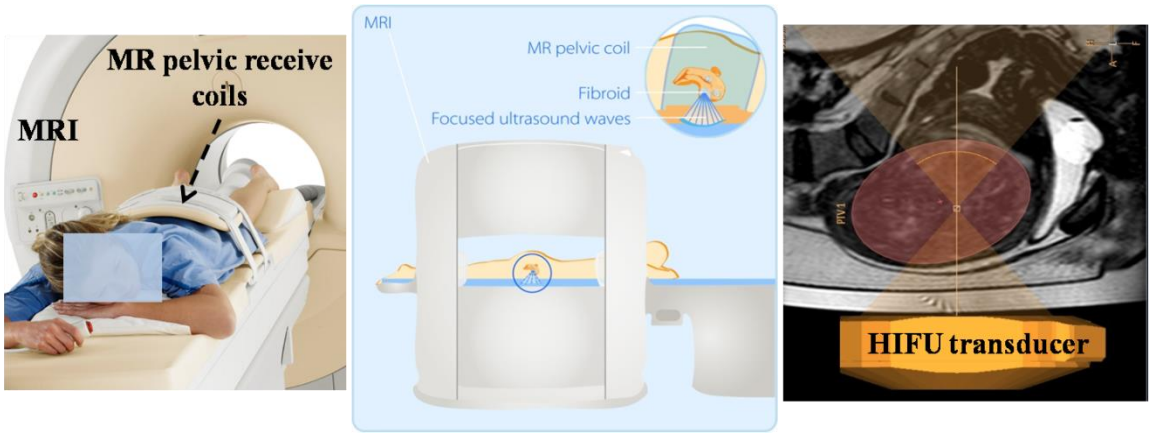

Figure 3.4 *In-vivo* HIFU thermal ablation of uterine fibroid experiment setup. The patient lie down on the HIFU table in prone position with feet first entering MRI scanner (Left); Patient stayed still inside MRI scanner (Middle); Treatment planning based on anatomic MRI images (Right). Image courtesy of Phillips healthcare.

Pretreatment Quality Assurance Procedure

A routine quality assurance procedure was performed by using a tissue mimicking HIFU phantom (Model TTP1; ATS Laboratories, Bridgeport, Conn) before each MR-HIFU procedure. According to the protocol provided by the manufacturer, four HIFU sonications (4-mm treatment cells without a feedback control) situated at least 2 cm apart were performed and monitored with clinical used MRTI sequence. Pass criteria for sonication accuracy included misregistration displacement from the intended target location within -3mm to 3mm in the left-right (LR), feet-head (FH) directions and -6mm to 6mm in the anterior-posterior (AP) direction and maximum temperature to be within 45^{o}C to 55^{o}C at the test power level of 30W at 1.2 MHz. Through this procedure, proper system calibration and normal function of the MR-HIFU system was ensured before *in-vivo* surgery.

3.1.1 Temperature Measurement Precision

Based on Eq. 2.21, temperature $T(r, t)$ change is proportional to the change of MRI measured phase. So the accuracy of MRTI strongly relies on the accuracy of MRI measured phase. The

noise in MRI is produced by electrical resistance in the receiver coil, dielectric and inductive losses in the sample, preamplifier electronics and RF transmitter[147]. These sources produce noise in the in-phase and out-of-phase MRI signals. The uncertainty of phase measurement (σ_ϕ) is inversely related to the signal-to-noise ratio (SNR_M) of the MRI magnitude image [119]. To better understand this, Eq. 3.1 was rewritten in Eq. 3.3 and 3.4.

$$\sigma_\phi \propto \frac{1}{SNR_M} \tag{3.3}$$

$$\Delta\phi = \alpha\gamma B_0 T_E \Delta T \tag{3.4}$$

where α is the PRF change coefficient for aqueous tissue, γ is the gyromagnetic ratio, B_0 is the main magnetic field, and T_E is the echo time. $\Delta\phi$ is the phase change introduced by the temperature change ΔT. The SNR_M is measured by calculating the difference in signal intensity between the area of interest and the background (usually chosen from the air surrounding the object) divided by the standard deviation of the back ground noise[148].

Temperature precision was analyzed in phantom, *in-vivo* pig thigh muscle and *in-vivo* women uterine fibroid by repeated measurements of temperature in unheated regions. The temporal standard deviation of the temperature measurement in unheated regions yielded a measure of the temperature precision.

Fig. 3.5 showed the measured temperature map on both coronal plane and sagittal plane for HIFU heating. HIFU beam is perpendicular to the coronal imaging plane and parallel to the sagittal plane.

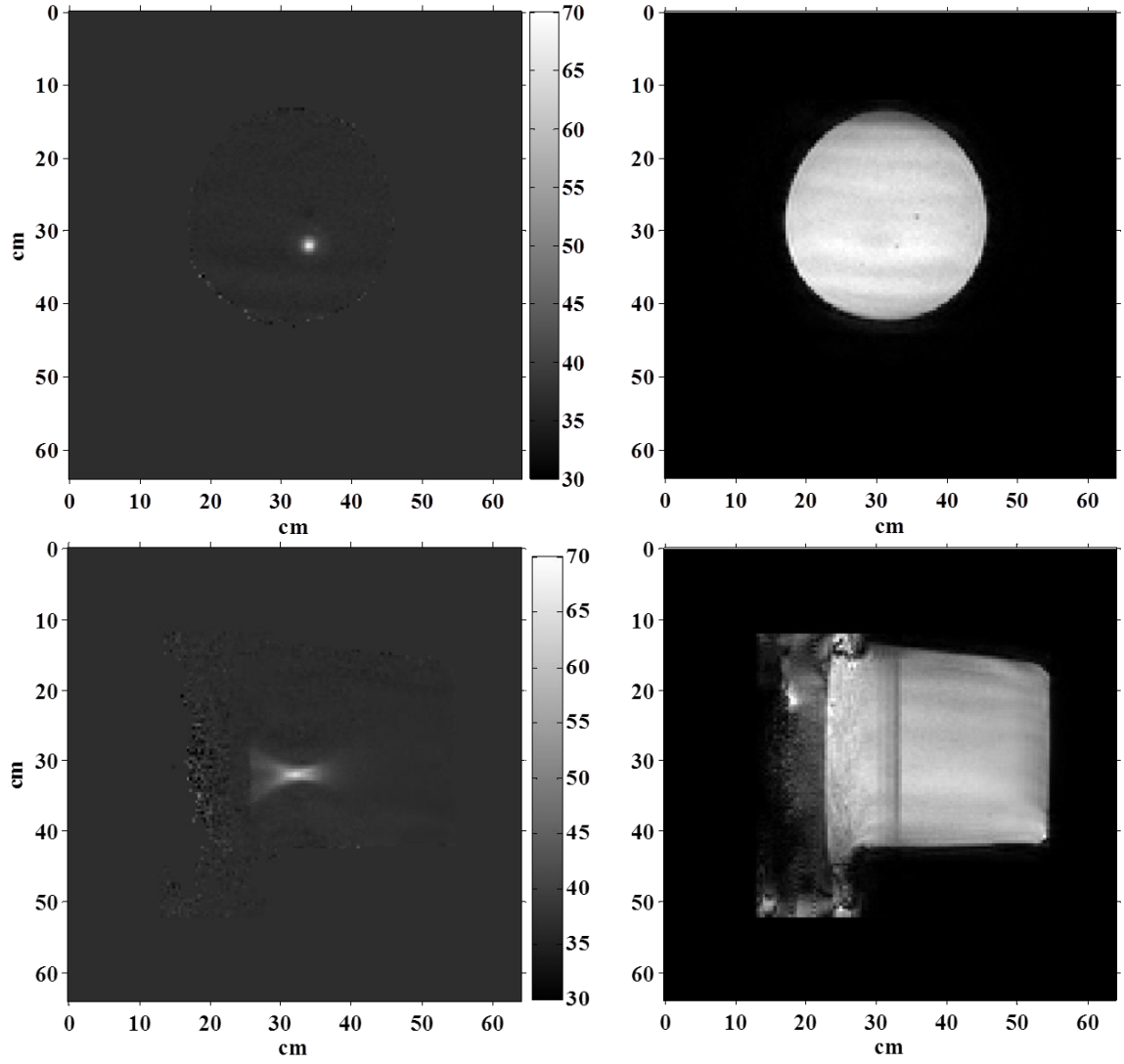

Figure 3.5 Temperature map (Left) and anatomical magnitude image (Right) of phantom study on coronal (Top) and sagittal (Bottom) slices. Color bar showed the temperature value in ^{o}C.

The average temperature precision was calculated in the six regions drawn in both coronal and sagittal plane far away from the heating center in phantoms was **0.35±0.03^{o}C** (Fig. 3.6).

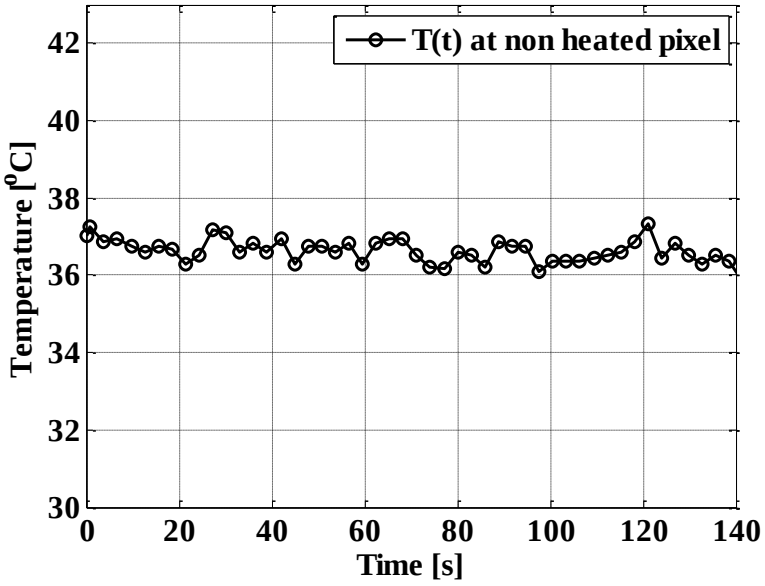

Figure 3.6 Temperature evolution of a representative pixel far away from heating center in phantom study

Temperature map (Left) and MRI magnitude (Right) images at one time point for HIFU ablation of pig thigh muscle (Top) and uterine fibroid (Bottom) are shown in Fig 3.7. The average measured temperature precision were **1.13±0.24°C** for pig thigh muscle and **1.22±0.37°C** for uterine fibroid treatment respectively. The difference of temperature measurement error between *in-vivo* animal study and *in-vivo* uterine fibroid treatment can also be visualized in Fig. 3.8.

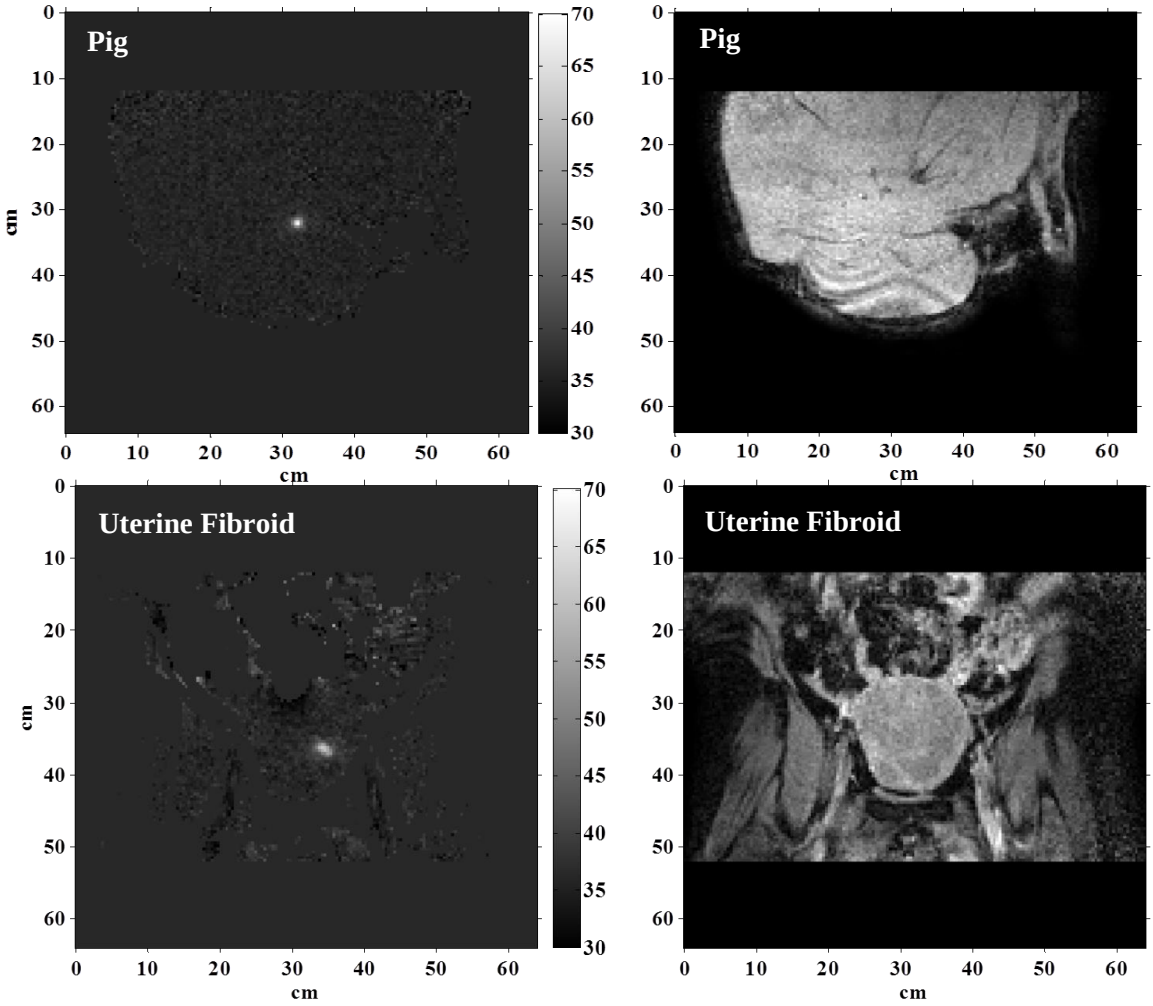

Figure 3.7 Temperature map (Left) and anatomical magnitude image (Right) of *in-vivo* pig study (Top) and *in-vivo* uterine fibroid (Bottom) treatment on coronal slice. Color bar showed the temperature value in ^{o}C. The heating was performed on pig thigh muscle.

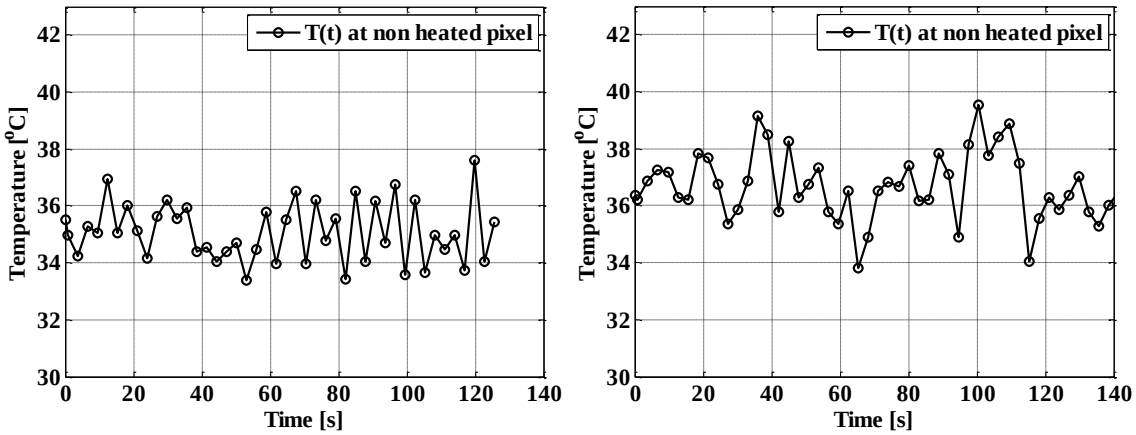

Figure 3.8 Temperature evolution of a representative pixel far away from heating center *in-vivo* animal study (Left) and *in-vivo* uterine fibroid (Right) treatment.

Regarding the temperature precision measured in phantom, *in-vivo* animal and *in-vivo* uterine fibroid treatment, temperature precision was highest in phantom and worst *in-vivo* uterine fibroid. This is because MR phase information is affected by tissue motion, and in living tissue this additional phase due to respiratory/cardiac motion, as well as susceptibility difference between tissues lowers the attainable temperature precision. The temperature distribution pattern shown in Fig. 3.5 and 3.7 also confirmed that HIFU focus was approximately an ellipsoid in phantom, *in-vivo* animal and uterine fibroid studies (circle in perpendicular to HIFU beam and ellipse in parallel to HIFU beam), as designed.

3.1.2 MR-Temperature Measurement Accuracy: Partial Volume Effects

MRTI essentially captures an analog variation of temperature into a spatially and temporally discrete representation in the form of a series of images. Therefore, the spatio-temporal discreteness (sampling size or pixel size, or sampling interval or temporal resolution) of MR TI will affect the accuracy of the measured quantity, i.e., temperature. Same underlying temperature spread may be measured differently when using different sampling scheme due to averaging effects (sampling grid location, effective voxel size, and temporal resolution). This effect is more conspicuous in HIFU heating, because the spatially non uniform deposition of

thermal energy into a small volume creates sharp spatial temperature gradient with a focal spot that has dimensions on the order of a MRTI voxel[149]. Parker et al., have reported 17% and 33% errors in measuring maximum temperature and retrospectively estimated lesion volume respectively has been shown using single focus HIFU heating, and 5% and 18% errors for 4-mm circle heating respectively with MRTI sampling grid size of $1.0 \times 1.0 \times 3.0$ mm^3[149]. However the MRTI sampling effect on peak temperature and lesion volume of new volumetric HIFU heating stratagem has not been evaluated yet. In this section, the MRTI sampling effect will be investigated for the new volumetric HIFU heating stratagem for all 4mm, 8mm, 12mm, and 16mm cell [150].

To assess the impact of spatial sampling (spatial resolution) effect of MRTI on accuracy of temperature and lesion volume measurement in the context of volumetric ablation, the spatio-temporal temperature distribution following MR-HIFU volumetric sonication using various cell sizes (4 mm, 8 mm, 12 mm, and 16 mm diameter) was analytically modeled by a series of 2D Gaussian functions with variances determined by the local thermal conductivity with very high spatial resolution of 0.05 mm x 0.05 mm. The analytic model assumed a peak temperature of 75 ^{o}C at the end of sonication, followed by cooling to 45 ^{o}C at various typical intervals used in clinical MR-HIFU setting (Sonalleve™, Philips Healthcare). The typical heating time and cooling was shown in Table 3.1.

Table 3.1 Typical heating and cooling times for various treatment cell sizes used in clinical HIFU setting

Cell diameter [mm]	Heating duration [s]	Cooling duration [s]
4	20	80
8	27	100
12	45	120
16	64	140

The spatio- temporal temperature distribution was generated using the formula given below:

$$T(x, y, t) = T(x_0, y_0, t) \cdot \exp\left(-\frac{(x - x_0)^2 + (y - y_0)^2}{2\sigma^2(t)}\right) \quad (3.5)$$

where (x_0, y_0) is the position of HIFU heating center, $T(x_0, y_0, t)$ is the instantaneous Gaussian peak temperature. $\sigma(t)$ is the instantaneous Gaussian variance at time t, which is dependent on the thermal diffusivity and linearly increases with the cooling time [151, 152].

$$\sigma^2_{cooling}(t) = \sigma_0^2 + 4Dt \quad (3.6)$$

Where σ_0 is the Gaussian variance at time right after stop heating, and D is the thermal diffusivity, which is directly related to the thermal conductivity (k), tissue density (ρ), and specific heat (c) as following

$$D = \frac{k}{\rho c} \quad (3.7)$$

Temperature map at each time point in coronal plane perpendicular to HIFU beam were modeled as a 2D Gaussian distribution (Eq. 3.5). In this analytical model, the thermal conductivity (k), tissue density (ρ) and specific heat (c) were assumed to be 0.5 W m^{-1} K^{-1}), 1050 kg/m^3, and 3500 J kg^{-1} K^{-1}) respectively which is similar to the skeletal muscle. The temporal resolution used was 1s. The peak temperature $T(x_0, y_0, t)$ was assumed to be linearly increased with the time during the HIFU heating period from 37 to 75^{o}C while linearly decrease with the time during cooling period from 75 to 45^{o}C. The Gaussian variance during the heating period was assumed to linearly increase from 0 to σ_0 which was determined by the target lesion area when the HIFU heating was stopped (feedback control). Determined σ_0 for each HIFU cells was shown in table 3.2. The analytical lesion area was then calculated from the analytical generated temperature maps based on Eq. 3.2.

Table 3.2 σ_0 for each type of cell.

Cell diameter [mm]	Target dose area [mm^2]	Determined σ_0 [mm]
4	12.57	1.89
8	50.27	3.67
12	113.10	5.25
16	201.06	6.84

The below was an example of generated analytical temperature distribution (Left) of 8mm cell right after stop heating and the dose contour (Right) of 30EM (outer circle) and 240EM (inner circle) (Fig. 3.9).

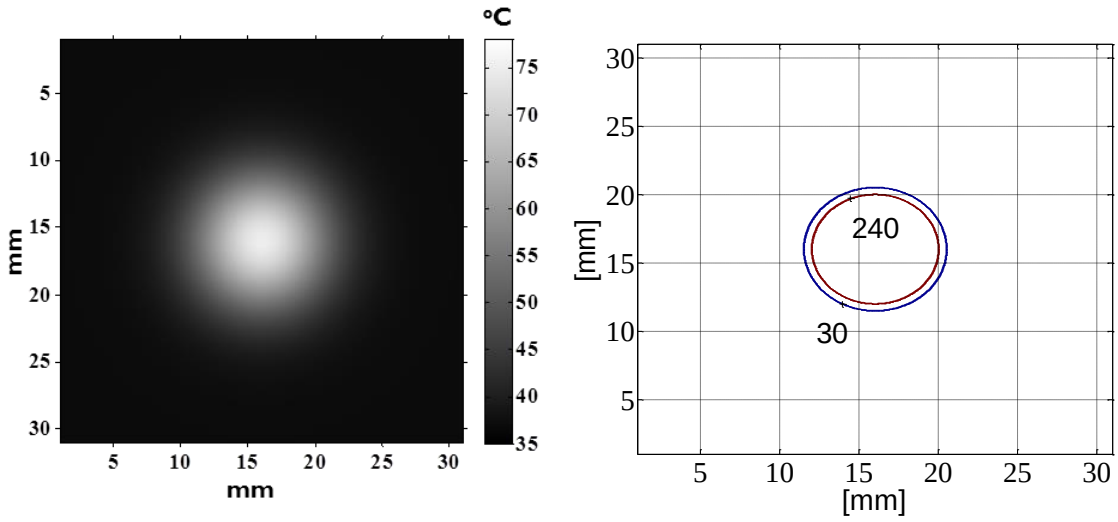

Figure 3.9 Generated analytical temperature map (Left) right after stop heating for mimicking an 8mm HIFU cell heating and the accumulated thermal dose map (Right).

The effect of acquired pixel size on peak temperature and thermal dose was then systematically evaluated by reconstructing spatio-temporal temperature images with progressively increasing pixel sizes starting at 0.5mm × 0.5mm and increasing step of 0.2mm × 0.2 mm. The reconstructed temperature map and corresponding dose accumulation was compared to the analytical result.

Representative reconstructed temperature maps at time right after heating with pixel size of 0.5mm × 0.5mm (Left) and 2.5mm × 2.5mm (Right) for smallest and largest cell size (4 mm and 16mm) were shown Fig. 3.10. Unlike the larger volumetric cell of a diameter of 16 mm, peak temperature of the 4 mm cell was substantially diminished at a spatial resolution of 2.5mm × 2.5mm due to the averaged temperature over the pixel. As a result, the estimated lesion area (> 240 EM) also had substantial errors (Fig. 3.12).

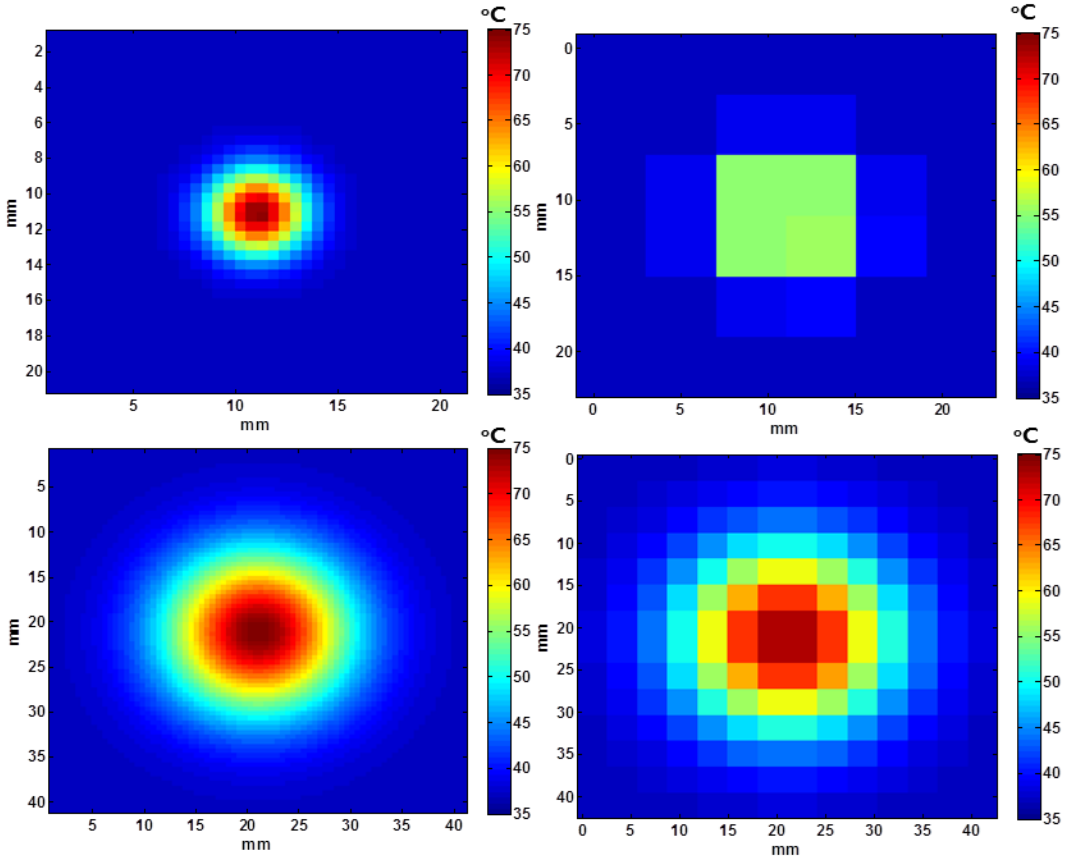

Figure 3.10 Representative reconstructed temperature maps right after heating for 4 mm cell (Top) and 16 mm cell (Bottom) with different reconstruction pixel size (Left: 0.5 mm × 0.5 mm and Right: 2.5 mm × 2.5 mm).

The mean and standard deviation of the peak temperature and lesion area with various reconstructed pixel size starting at 0.5 × 0.5 mm^2 with increasing step of 0.2 × 0.2 mm^2 were estimated by shifting the spatial location of the peak temperature within the pixel at a tenth of a

pixel increments in both x- and y- direction. The relative error of reconstructed peak temperature and lesion area at different reconstructed pixel size is shown in Fig. 3.11 and 3.12 respectively. The simulations assumed isometric pixel size. The 1^{st}, 2^{nd}, 3^{rd}, and 4^{th} rows were the plots of 4mm, 8mm, 12mm and 16mm cell respectively used in clinical MR-HIFU setting.

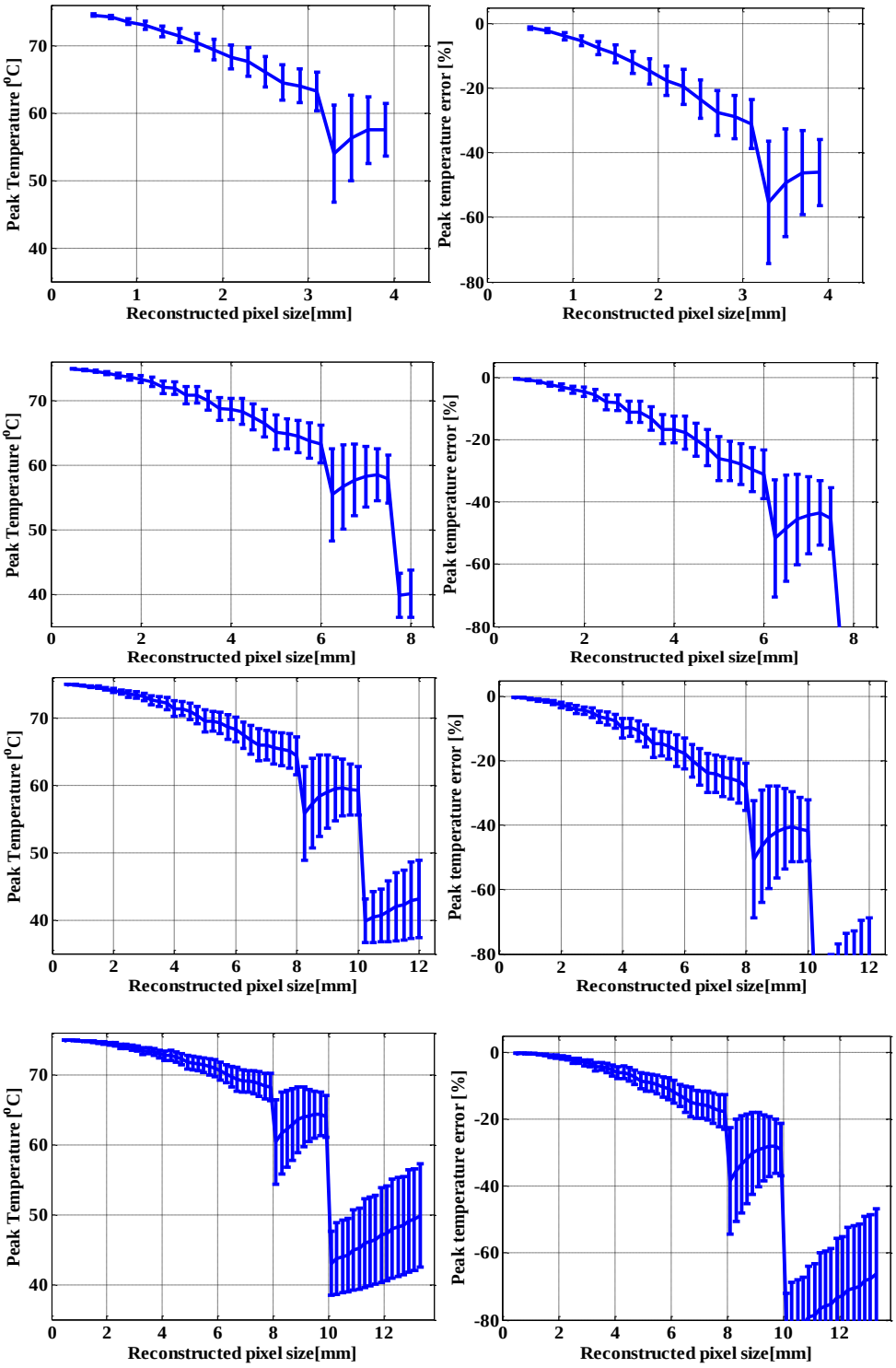

Figure 3.11 The dependence of absolute (Left) and relative (Right) percent error in MR-HIFU temperature measurement on spatial resolution.

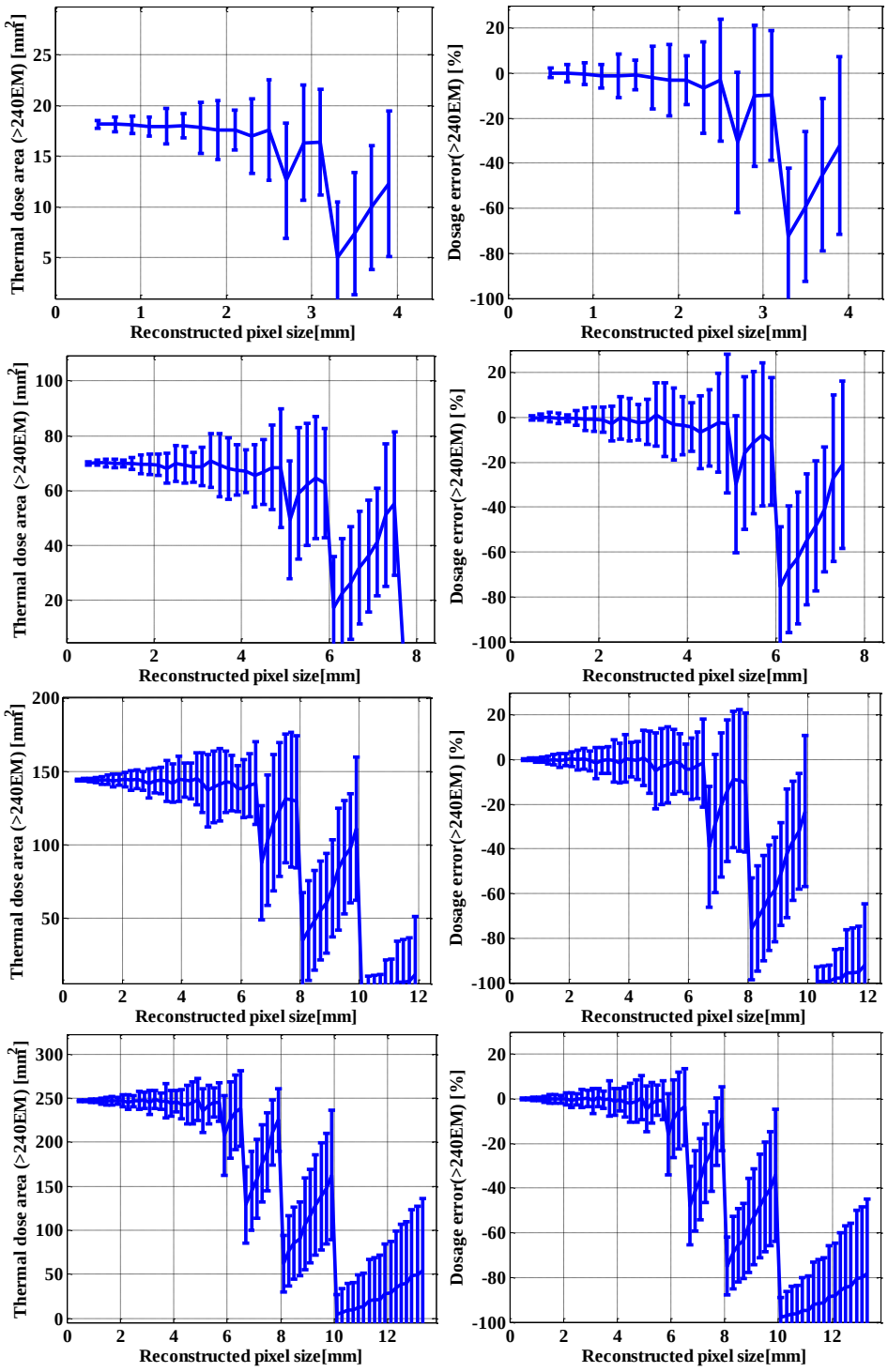

Figure 3.12The dependence of absolute (left) and relative (right) percent error in MR-HIFU lesion area (>240EM) measurement on spatial resolution.

The uncertainty of both measured peak temperature and calculated lesion area increases with the reconstructed pixel size for various HIFU cell size. In other words, the accuracy of temperature and thermal dose measurements are strongly influenced by the spatial resolution. To achieve 10% error in peak temperature measurement, the spatial resolution needs to be less than $1.5\times1.5mm^2$, $2.5\times2.5mm^2$, $4.0\times4.0mm^2$, and $5.0\times5.0mm^2$ for 4mm, 8mm, 12mm, and 16mm HIFU cell respectively. The spatial resolution of temperature measurement was $2.5\times2.5mm^2$ for clinical MR-HIFU surgery which resulted in peak temperature measurement error were $25\pm7\%$, $8\pm2\%$, $4\pm1\%$, and $2\pm0.7\%$ for 4mm, 8mm, 12mm, and 16mm cell respectively while $32\pm25\%$, $0.0\pm10\%$, $0\pm5\%$, and $0\pm2\%$ for lesion area measurement error. Therefore spatial resolution of $2.5\times2.5mm^2$ for 4mm cell was totally not reliable in both temperature and lesion volume measurement. That's why 4mm cell was excluded from tissue blood perfusion characterization in this dissertation. However the clinical used spatial resolution for temperature measurement was still good for bigger cell size (8mm, 12mm, and 16mm).

3.1.3 Accuracy of HIFU Heating

To quantify the accuracy of HIFU heating, two comparisons were made between actual lesion and target lesion. *First*, the position of centroid of the thermal dose (>240EM) for each HIFU cell size (4mm, 8mm, 12mm, and 16mm in diameter) was compared to the location of target lesion (lesion in this dissertation was defined as a thermal dose exceeding 240EM). The distance between the intended target location, and the measured target location was calculated in three direction (FH, RL, and AP), which was referred as offset in each direction. Here AP direction was parallel to HIFU beam while FH and RL were perpendicular to HIFU beam. Fig. 3.13 shows the offsets in FH, RL, and AP direction for phantom (Top), *in-vivo* pig (Middle), and *in-vivo* uterine fibroid (Bottom). The inner and outer circles showed the offsets value of 2.5mm

and 5.0mm distance away from the target position of HIFU heating respectively which corresponded to one and two pixels respectively.

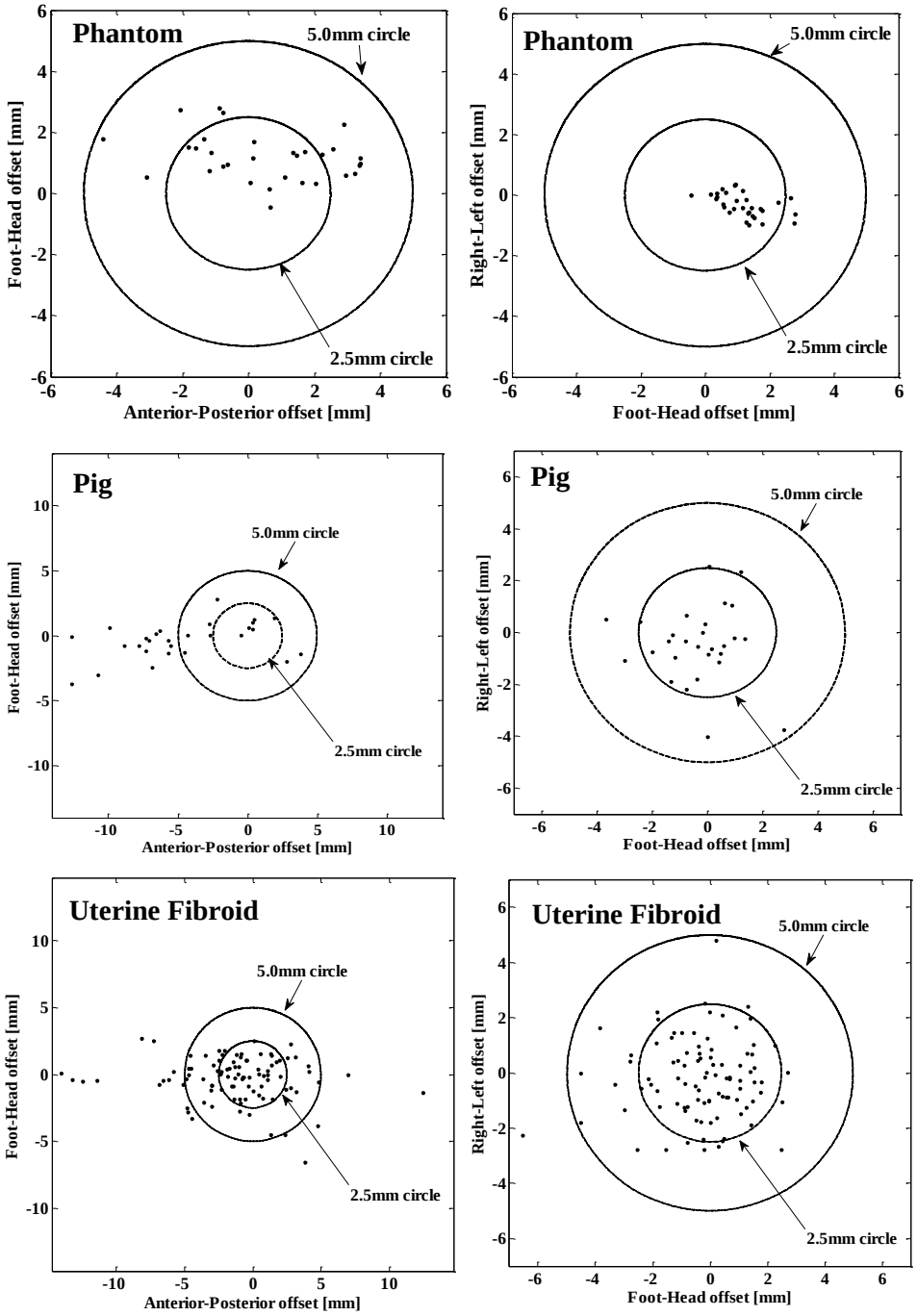

Figure 3.13 Offsets between target position and the centroid of actual thermal dose lesion region for phantom (Top), *in-vivo* pig and *in-vivo* uterine fibroid (Bottom). The offsets of 100%, 100%, and 98.3% treated cell in the direction of perpendicular to HIFU beam falls in the range of 2-pixel away from intended location in phantom, pig and uterine fibroid respectively while 100%, 53.6%, 28.3% treated cell falls outside of the 2-pixels from the intended position respectively in the direction parallel to HIFU beam.

The offsets in the directions (RL and FH) perpendicular to the HIFU beam in all phantom, animal, and uterine fibroid studies were strictly confined within 5.0mm from target position, which was less than two pixels. The phantom and animal studies showed that most data points even fell inside of 2.5mm circle which was only one pixel away from target. However, the offset in the AP direction, parallel to the HIFU beam, exhibited more spread compared to the direction perpendicular to the HIFU beam, and a few data points even fell outside of 5.0mm away from target. This was more conspicuous in the pig and uterine fibroid studies. This can be explained by the actual shape of the HIFU heating due to the near field effect. Because more energy was deposited in the region away from heating center but toward to HIFU transducer (near field) than the region away from heating center but away from HIFU transducer (far-field). This brought the centroid of actual lesion closer to the transducer. Another reason for the larger offset in the AP direction in *in-vivo* studies compared to phantom studies is due to the phase error introduced by tissue inhomogeneity, since the tissue within the ultrasound beam in this MR-HIFU system was assumed to be uniform. For example, the fat layer in ultrasound beam would bring the HIFU focus closer to the HIFU transducers.

Second, the actual HIFU lesion size (dimension in the short and long axis of ellipsoid) was compared to the intended lesion size (Table 3.3). The actual dimension of the thermal lesions induced by HIFU ablations were calculated from the thermal dose maps by measuring the connected voxels with a dose exceeding 240EM. The thermal lesion diameter was attained from the three central coronal slices that had the largest area of connected voxels above 240EM by computing the diameter of a circle with corresponding cross-sectional area. The length of the thermal lesion was measured from the sagittal image as the maximum distance along the HIFU beam direction of connected voxels above 240EM. This was done in a custom-build software in HIFU console[126, 128, 148]. The planned dimension and actual caused dimension of lesion were

shown in Fig. 3.14 for phantom (Top), *in-vivo* animal (Middle), and uterine fibroid (Bottom). The dots showed the experimental data while the solid black line showed the linear fit between dimension of actual caused lesion and planned lesion. The slope indicated how good the HIFU heating is between the planned and actual lesion. In this analysis, it should be noted that while all cells including aborted sonication were used for calculating the offsets (targeting accuracy analysis) only successfully treated cells were chosen to analyze cell dimension (target size analysis).

Table 3.3 Planned dimension of lesion size using different HIFU cell to heat the tissue

Planned dimension	4-mm cell	8-mm cell	12-mm cell	16-mm cell
Diameter (mm)	4	8	12	16
Length (mm)	10	20	30	40

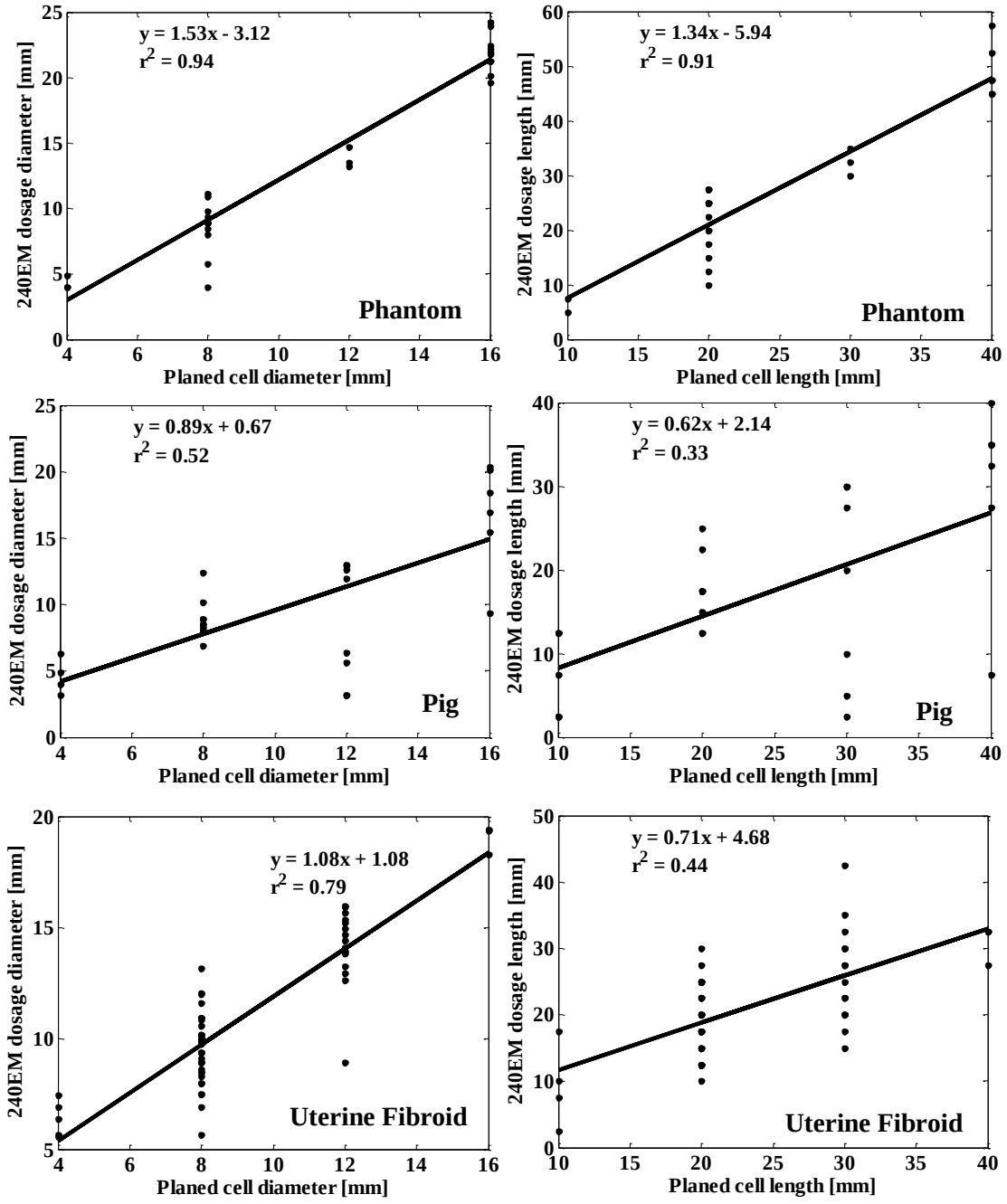

Figure 3.14 Actual dimension of HIFU induced lesion size (short (Left) and long (Right) axis) was compared to planned dimension for phantom (Top), *in-vivo* pig (Middle) and *in-vivo* uterine fibroid (Bottom) treatment.

The actual measurement of the short-axis diameter of the heated ellipsoid was larger than the planned diameter in the phantoms (slope was 1.5), but was close to the planned diameter in

the *in-vivo* animal and human studies (slope was 0.9, 1.1 respectively). On the other hand, the long axis diameter of the heated ellipsoid was significantly longer than the planned diameter in the phantom (slope was 1.3), but was substantially shorter in the *in-vivo* animal and human studies (0.6 and 0.7 respectively).

The slope between actual lesion size and planned size of phantom studies was shown much larger than the slope of *in-vivo* studies of both pig and human uterine fibroid. We speculate that this may be attributed to the thermal energy loss due to convection within tissue. No convective heat loss occurs in phantoms, and this may result in large lesion size, compared to lesion sizes created in live tissue with convective heat loss. This would result in more heat energy was dissipated by blood perfusion and thus cause less lesion volume in *in-vivo* study. This speculation is supported by the energy efficiency analysis in the following section.

3.1.4 Energy Efficiency of HIFU Heating

Thermal energy efficiency of HFIU heating is clinically calculated as the ratio of actual caused lesion volume in milliliter (mL) to applied HIFU energy in kilojoules (kJ), which is the product of heating duration and applied acoustic power. The thermal dose volume can be obtained from built-in software in HIFU console.

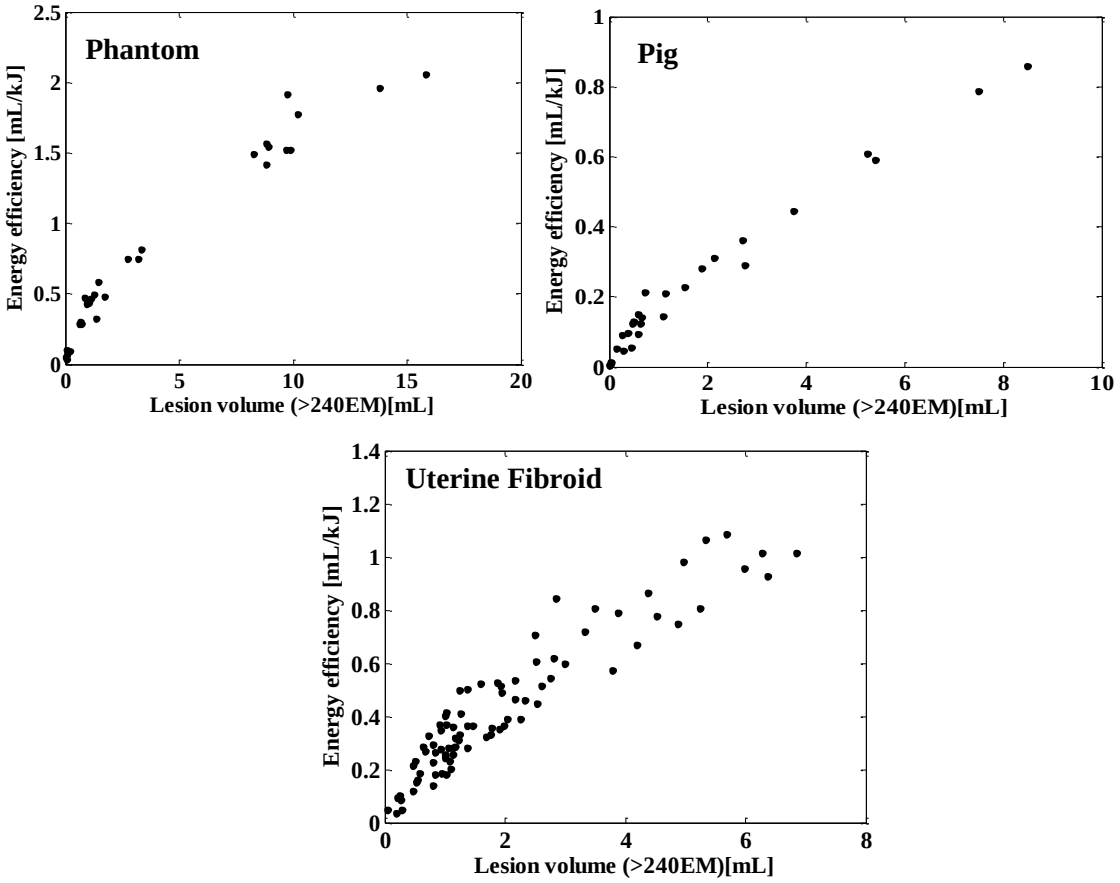

Figure 3.15 Energy efficiency vs actual HIFU caused lesion volume in phantom (Top left), *in-vivo* pig thigh muscle (Top right) and *in-vivo* uterine fibroid (Bottom) studies.

HIFU thermal energy efficiency was plotted as the function of actual HFU caused lesion volume for phantom (Top left), *in-vivo* pig (Top right), and *in-vivo* uterine fibroid (Bottom) studies respectively (Fig. 3.15). All three types of HIFU studies showed that energy efficiency increase with the volume size. The phantom studies showed the highest energy efficiency and animal studies in healthy pig muscle demonstrated lowest efficiency. The efficiency for uterine fibrous tissue was in between. This suggests that the blood perfusion in pig skeletal muscle may be greater than in uterine fibroids [46].

Conclusions:

The key performance metrics of the MR-HIFU system used in this dissertation were determined as follows:

1. The MRTI protocol predominantly used in this dissertation has a precision of 1.2 ± 0.4 ℃ for *in-vivo* uterine fibroid applications. Temperature precision is much higher for phantoms where confounding effects such as respiration, cardiac pulsation, and blood flow are absent.
2. In order to achieve less than a 10% temperature *measurement error* or *accuracy*, the relative pixel size of MRTI acquisition should be less than a third of the dimension of the short-axis diameter of the ellipsoid.
3. *Targeting accuracy*: The heated cell centroids were within 2 pixels of the planned cell centroids for 1.7%, and 28.3% of the cells along the planes perpendicular and parallel to the HIFU beam path, respectively, for *in-vivo* ablation of uterine fibroids.
4. The *energy efficiency* of treatment substantially increased with the treatment cell volume, and ranged from 0.4mL/kJ for 2cc treatment volume to 0.9mL/kJ for 6mL treatment volume.

Chapter 4

Tissue Thermal Conductivity Estimated from MR-HIFU

4.1 Introduction

Successful clinical applications for focused ultrasound surgery[17-19], radio frequency (RF) cancer therapy[20, 21], hyperthermia[22, 23], cryopreservation[153], and cryosurgery[24, 25] require the ability to accurately create lesions by heating or freezing of tissue. The success of such ablative procedures largely depends on tissue thermal properties and physiological response of tissues in the target and surrounding area. An accurate knowledge of tissue thermal conductivity, specific heat, blood perfusion rate, and their temperature dependencies are key factors for a complete understanding and control of heat transfer in living tissue[26]. In this chapter, we focus on the determination of one of these important parameters: *tissue thermal conductivity*.

Unlike infrared-[38] and ultrasonography-[39] based techniques, MRTI techniques to estimate thermal conductivity are unencumbered by constraints related to the depth of penetration, and can span a relatively large thermodynamic range (0~100^{o}C). Cheng and associates [40] and Dragonu and coworkers[154] have described MRI-based methods for estimating tissue thermal conductivity. However, these approaches involve only modest heating of tissues (up to 15 ℃), which is not high enough to induce thermo-coagulative necrosis. We sought to determine whether the thermal conductivity of tissues could be estimated *in-vivo* from MRI-based temperature measurements of tissues treated with high-temperature thermal ablations that cause coagulative necrosis. Compared with other MRI-based methods, such ablations require much higher temperatures, and the tissue thermal property response at these high temperatures is completely unknown. Therefore, we

devised a method for estimating the thermal conductivity of tissue *in-vivo* at therapeutic temperatures level between 60 ℃ and 90 ℃. This method allowed us to estimate tissue thermal conductivity in the context of clinical thermal ablation using MR-HIFU procedure. We used this method *in-vivo* to determine thermal conductivity in pig thigh muscle and uterine fibroids in women treated with HIFU at therapeutic power levels (acoustic power of 80 to 170 W) over a relatively short period (10 to 70 seconds)[144].

4.2 Theory

4.2.1 Theoretical Background for Extracting Thermal Conductivity

The bio-heat transfer model describes the spatio-temporal temperature evolution in tissue in the absence of large-vessel flow:

$$\rho_t c_t \frac{\partial T(\vec{r},t)}{\partial t} = k_t \nabla^2 T(\vec{r},t) - \rho_b c_b \omega (T(\vec{r},t) - T_a) + Q_{met} + Q_{ext} \qquad (4.1)$$

where $T(\vec{r},t)$ is the tissue temperature at time t and location $\vec{r}$; ρ_t , c_t, and k_t are tissue density, specific heat, and thermal conductivity, respectively; ρ_b, c_b, and ω_b are blood density, specific heat, and perfusion rate respectively; T_a is the arterial blood temperature, Q_{met} is the metabolic rate, and Q_{ext} is the power deposition per unit volume by external heat source. During HIFU heating, $Q_{ext} >> Q_{met}$, and subsequent to thermal ablation, ie, after delivery of a 240-EM dose, the tissue can be considered metabolically inactive. As a result, the Q_{met} term could be ignored in the context of HIFU therapy. Assuming an equal density and specific heat of tissue and blood ($\rho_t = \rho_b$, $c_t = c_b$), a uniform thermal conductivity in the tissue (k_t), and only the cooling period ($Q_{ext} = 0$), Eq. 4.1 can be rewritten in a simpler form:

$$\frac{\partial T_\delta(\vec{r},t)}{\partial t} = D\nabla^2 T_\delta(\vec{r},t) - \omega_b T_\delta(\vec{r},t) \tag{4.2}$$

where $T_\delta(\vec{r},t) = T(\vec{r},t) - T_a$ is the temperature rise compared to the arterial temperature, and $D = \frac{k_t}{\rho_t c_t}$ is the tissue thermal diffusivity in [m^2s^{-1}]. For simplicity, each expression T stated below in this chapter stands for temperature increase T_δ compared to the arterial temperature. Also, parameters such as ρ_t, c_t, ρ_b, c_b, and T_a are assumed to be time-invariant. This equation could then be analytically solved by using Fourier transformation over spatial coordinates with the assumption that homogeneous tissue in the region of interest is large enough with respect to the heated area. (This assumption is not always valid, especially when a large vessel exists in that area).

$$\frac{\partial T(\vec{k},t)}{\partial t} = -(k^2 D + \omega_b) T(\vec{k},t) \tag{4.3}$$

where $T(\vec{k},t)$ is the spatial Fourier transformation of $T(\vec{r},t)$. Assuming that diffusivity and perfusion are time-invariant, the analytical solution for this 1st-order differential equation during the cooling period is

$$T(\vec{k},t) = T(\vec{k},0)\exp(-k^2 Dt)\cdot\exp(-\omega_b t) \tag{4.4}$$

where $T(\vec{k},0)$ is the initial spatial temperature distribution at the beginning of the cooling period in the Fourier domain. The spatial distribution of the HIFU beam energy deposition is approximated by a 3-dimensional (3D) Gaussian distribution that has longitudinal and transverse dimensions with respect to the ultrasound beam direction and that depends on ultrasound frequency, the radius of curvature, and the aperture of the transducer. Although the Gaussian-fitted spatial distribution of temperature is ideally suited for a fixed-focal-point heating strategy, the initial spatial temperature distribution $T(\vec{k},0)$ right after heating could still be fitted as a

Gaussian function in the volumetric heating strategy during the cooling period. The Gaussian temperature distribution in the spatial domain results in the following expression in the Fourier domain[154]:

$$T(\vec{k},0) = T_0(2\pi)^{3/2}\sigma_{0xy}^2\sigma_{0z}\exp[-\frac{(k_x^2+k_y^2)\sigma_{0xy}^2}{2}]\exp[-\frac{k_z^2\sigma_{0z}^2}{2}]\exp[-w_b t] \quad (4.5)$$

where T_0 is the temperature at the trajectory center at the end of the sonicating period and where σ_{0xy} and σ_{0z} are the Gaussian variances (temperature spatial spread) in the horizontal (Oxy) and vertical (Oz) directions respectively. The analytical solution of spatial temperature evolution is solved by inserting Eq. 4.5 into Eq. 4.4 through the inverse Fourier transform under the assumption of uniform tissue thermal properties:

$$T(\vec{r},t) = T_0\frac{\sigma_{0xy}^2}{\sigma_{0xy}^2+2Dt}\sqrt{\frac{\sigma_{0z}^2}{\sigma_{0z}^2+2Dt}}\exp[-w_b t]\exp[-\frac{x^2+y^2}{2\sigma_{0xy}^2+4Dt}]\exp[-\frac{z^2}{2\sigma_{0z}^2+4Dt}] \quad (4.6)$$

Note that the perfusion term in Eq. (4.6) acts as a scaling factor, while diffusivity is the only factor that governs the shape of the Gaussian temperature spread and the rate at which the Gaussian spread expands: $\frac{\partial(\sigma_{xy}^2)}{\partial_t}$. So, in this case, the dependency of Gaussian variance on thermal diffusivity can be calculated from the temperature evolution from the coronal slices as follows:

$$m = \frac{\partial(\sigma_{xy}^2)}{\partial t} = \frac{\partial(2\sigma_{0xy}^2+4Dt)}{\partial t} = 4D = \frac{4k_t}{\rho_t c_t} \quad (4.7)$$

where m is the slope of the Gaussian variance change in the time domain and where ρ_t (1060 kg·m^{-3}) and c_t (3600 J·kg^{-1}·K^{-1}, at ~37 ^{o}C) are the tissue density and specific heat, respectively. The perfusion term in Eq. 4.6 will not affect the change in Gaussian variance but affect only the peak value of the Gaussian temperature spread. Hence, thermal conductivity could be estimated

by exclusively analyzing the change in Gaussian variance of the temperature spread in Eq. 4.7 and is independent of blood perfusion. In this method, the thermal conductivity was the average effect of the time course investigated, and the tissue-specific heat change was neglected during this short time.

4.2.2 Post-processing of Temperature Profiles to Extract Thermal Conductivity

To estimate thermal conductivity, we analyzed the evolution of the spatial spread of temperature maps during the cooling period [40]. Post-processing of the temperature-drift corrected-phase data involves 2 steps. First, the temperature distribution on each of the 3 coronal planes (in a 75×75 mm^2 region located around the center of HIFU cell trajectories) at each of the cooling time points, is fitted by a 2D Gaussian function based on Eq. 4.6 by using a Levenberg-Marquardt algorithm and custom software in MATLAB (MathWorks Inc., Natick, Massachusetts, USA) to determine Gaussian variance $\sigma_{xy}^2(t)$. Only those Gaussian variances that were fit with a high confidence were used in the calculation of thermal conductivity. The quality of fit (r^2) was determined by a figure of merit defined by:

$$r^2 = \frac{\sum_{i=1}^{n} w_i (y_i' - \bar{y})^2}{\sum_{i=1}^{n} w_i (y_i - \bar{y})^2} \tag{4.8}$$

Where y_i, y_i', $\bar{y}$, and w_i are test data, fitted data, mean of the test data, and weights of the test data respectively. r^2 can take on any value between 0 and 1, with 1 indicating a perfect fit of the model to the measured data, and 0 indicating a complete lack of correlation between the measured data and the fitted model [155]. To improve the quality of fit, each temperature value included in the 2D fit was weighted by the magnitude of the corresponding voxel (as weights w_i), as the phase standard deviation is known to be inversely proportional to the SNR of the MRI magnitude image. The fit yielded the Gaussian variance of the temperature spread $\sigma_{xy}^2(t)$ at each time point.

Second, the temporal evolution of Gaussian variance $\sigma_{xy}^2(t)$ was fitted to a linear function of the cooling time. The local tissue thermal diffusivity *D* was the slope of the fit, and thermal conductivity k_t was then calculated according to Eq. 4.7. The thermal conductivity value corresponding to the fit that yielded the highest r^2 value ($r^2 > 0.9$) among the coronal slices was chosen as the estimated thermal conductivity.

4.3 MR-HIFU Experiments

4.3.1 *In-vivo* Animal Study

We performed a total of 40 volumetric ablations in the thigh muscles of 4 pigs using a clinical MR-HIFU surgery procedure with either a feedback (n = 25) or a non-feedback (n = 15) algorithm (Table 4.1). Thirty-five of the attempted ablations were successfully completed: 23 of these procedures used a feedback algorithm, and the other 12 used a non-feedback algorithm. Spatio-temporal temperature profiles from these successfully treated cells were used to estimate the thermal conductivity *in-vivo* pig thigh muscle[156]. In 3 of the 5 unsuccessful cases, the safety algorithm caused the treatments to be automatically discontinued once the near-field or far-field temperature exceeded the predefined temperature safety limits; in the other 2 cases, treatment failure was due to equipment malfunction. The mean of the temporal standard deviation of temperature in untreated regions was 1.1 ± 0.2 ℃. The regions of real-time temperature change for all treatment cell sizes (4, 8, 12, and 16 mm) were roughly ellipsoidal, with the longest axis along the direction of propagation of the HIFU beam (as seen in the sagittal monitoring plane) and the two short axes in the direction perpendicular to HIFU beam (as seen coronal monitoring plane).

Table 4.1 Summary of experiments performed in each pig.

Pig	Body Temperature (^{o}C)	No. of Sonications	Peak Temperature (^{o}C)	Power (W)	Duration (sec)	Sonication Frequency (MHz)
1	36.0	4	65.4-71.6	140	20.8-70.7	1.2
2	36.0	2	65.1-65.6	140	27.7	1.2
3	35.5	4	67.1-86.3	140	24.4-65.1	1.2
4*	34.8	25	57.7-79.7	100-130	20.1-76.4	1.2, 1.4

* This procedure was performed at a different institution

The complete sequence of steps is presented in Fig. 4.1 A-D. Images from the treatment planning on the therapy console before sonication (Fig. 4.1A), MR evaluation of the non- perfused lesion at ~1 hour after treatment (Fig. 4.1B), and pathologic evaluation approximately 5 hours (Fig. 4.1C) and 5 days (post formalin fixation) (Fig. 4.1D) after treatment. At each step, the results showed excellent correspondence to one another[157].

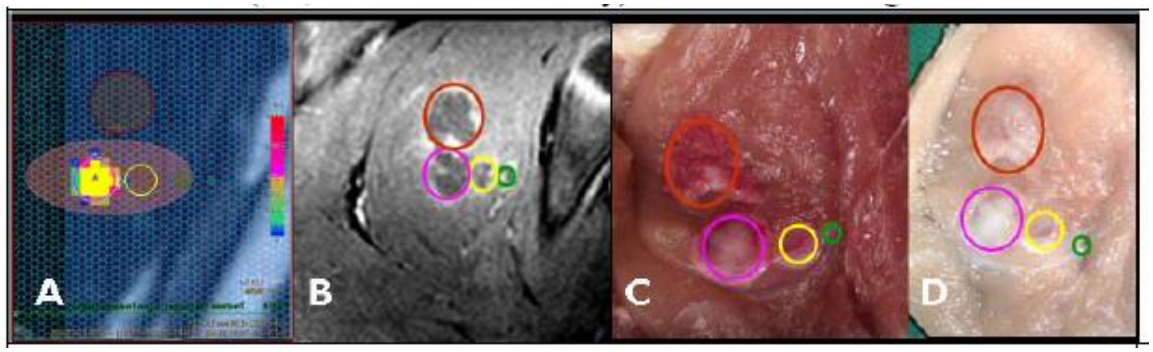

Figure 4.1 The 4-mm (green circles), 8-mm (yellow circles), 12-mm (pink circles), and 16-mm (red circles) lesions on MR-HIFU planning console. In view A, the real time temperature and thermal dose maps were overlaid on the 12-mm cells, and the cell grids (blue) for planning the treatment were overlaid on the anatomic image. Post-contrast non-perfused volumes after treatment (B), immediately after necropsy (C), and after necropsy and immersion in formalin (D) show the well-formed lesions.

Fig. 4.2 A-F showed the results of a representative HIFU non-feedback sonication of an 8-mm treatment cell. Fig. 4.2A clarified the anatomic structure of the pig leg, and Figure 4B showed a temperature map in the coronal plane at the end of HIFU treatment; the arrows indicate the location of the heating center (black arrow) and a representative voxel outside the heated region (blue arrow). The temporal evolution of these 2 points was plotted in Fig. 4.2C. The standard

deviation of the temperature (1.1 ± 0.2 ℃) confirmed the precision of the MRI thermometry. The temperature increased during HIFU sonication and then decreased after sonication (Fig. 4.2C) as a result of heat conduction and convection, which were influenced by tissue conductivity, blood perfusion, and the external heat source. Fig. 4.2D displayed the spatial spread of the temperature map and the quality of the 2D Gaussian fit right after heating. Figure 4E showed Gaussian-fitted temperature profiles around the trajectory center at 32.8 (t_1), 50.2 (t_2), and 82.2 seconds (t_3) after HIFU sonication was discontinued. The temporal evolution of Gaussian variance $\sigma_{xy}^2(t)$ and the associated linear fit were shown in Fig. 4.2F. This graph indicated a linear regression in time with goodness of fit (r^2 = 0.96). The average thermal conductivity based on Eq. 4.7 was 0.52W m^{-1} K^{-1} with a reproducibility of 10% (Fig. 4.3).

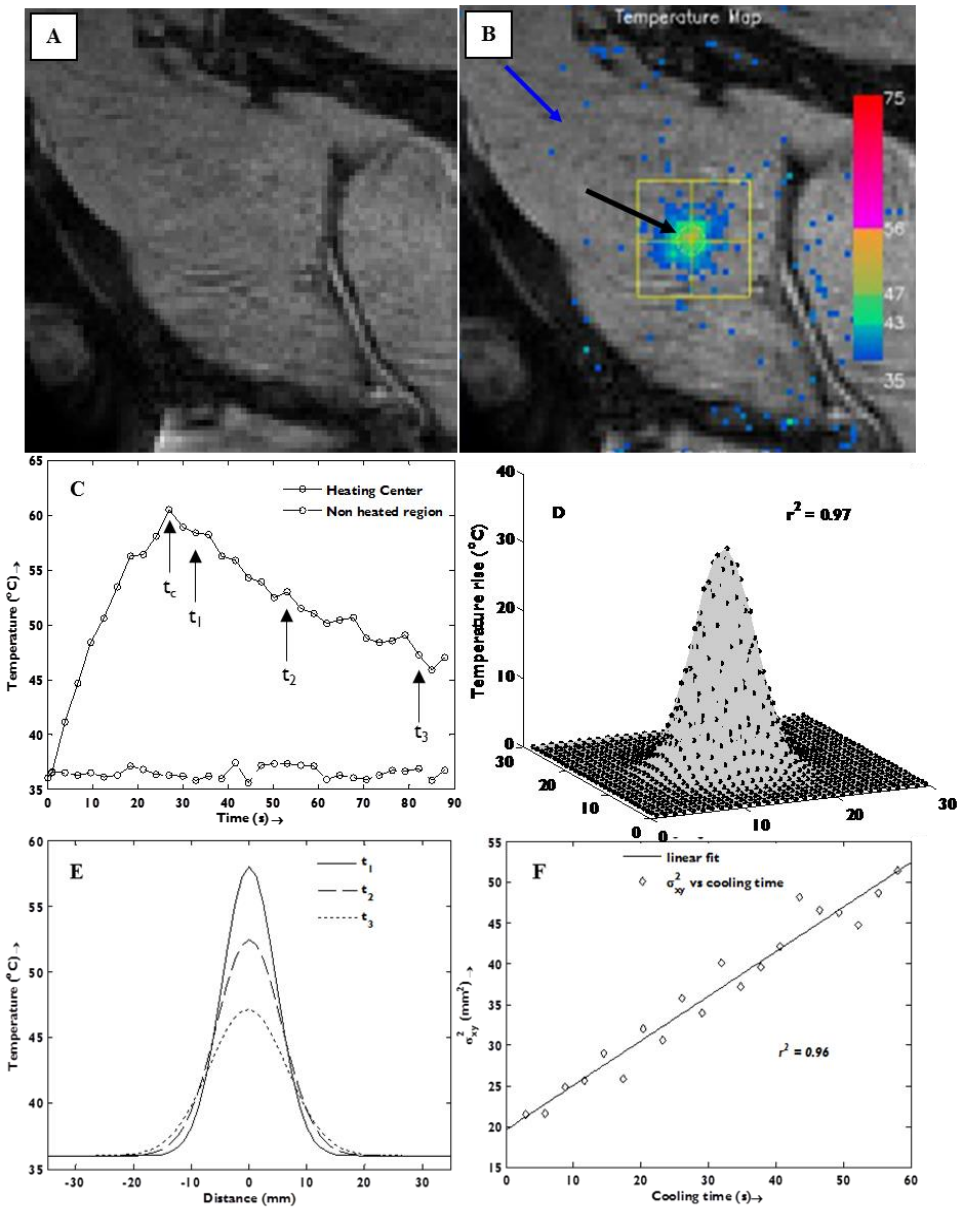

Figure 4.2 Results of a typical HIFU sonication using MRI thermometry. (A) MRI showed the anatomy of the pig leg. (B) Color-coded temperature distribution overlaid on the MRI anatomic information. (C) Temperature evolution at the trajectory center (black arrow in view B) and the region outside of the heating (blue arrow in view B). Time point t_c corresponds to the point at which the ultrasound was discontinued. (D) Experimental temperature spread (circle) and the associated 2D Gaussian fit right after sonication. (E) Gaussian-fitted temperature profiles across the trajectory center for 3 different time points (indicated in view C) during the cooling period. (F) Temporal evolution of $\boldsymbol{\sigma^2_{xy}}$ during the cooling period.

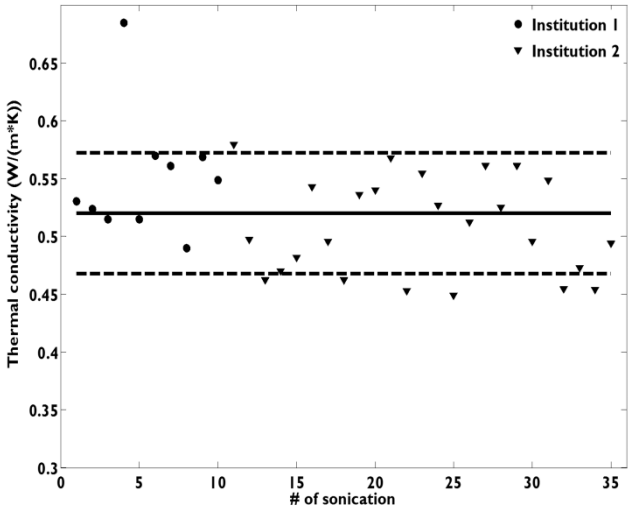

Figure 4.3 Estimated thermal conductivity based on temperature data from 10 of 15 sonications performed at St Luke's hospital (diamonds) and from 25 of 25 sonications performed at another institution (circles).The solid line shows the mean value for estimated thermal conductivity from different sonications, and the dashed line shows a variation of 10% around the average thermal conductivity.

4.3.2 *In-vivo* Uterine Fibroid Study

A total of 36 volumetric ablations were used to treat six uterine fibroids of five women under a clinical MR-HIFU system. Bulk of the treatment cells used a feedback (32/36) algorithm (Table 4.2). Spatio-temporal temperature profiles from these treatment cells were used to estimate the thermal conductivity of uterine fibroid. Incomplete ablations, for the reasons described below, were not used to estimate thermal conductivity: *(i)* the safety algorithm caused the treatments to be automatically discontinued once the near-field or far-field temperature exceeded the predefined temperature safety limit ; *(ii)* low signal to noise ratio occurred during the treatment; *(iii)* large patient motion was detected during temperature acquisition ; and *(iv)* the shape of temperature spread cannot be approximated to be a Gaussian function.

Table 4.2 Summary of experiments performed in each patient.

Patient	Body Temperature (°C)	No. of Sonications	Maximum Temperature (°C)	Power (W)	Duration (sec)
1	37.1	1	68.9	100	27.7
2	37.2	3	60.9-65.9	90-100	20.7
3	37.0	10	62.1-66.6	80-120	22.5-62.6
4	37.0	11	62.0-69.9	80-120	30.8-73.2
5	36.4	11	57.63-70.4	120-170	24.5-40.8

Figure 4.4 showed the treatment planning in HFIU console based on the MRI anatomic images (Left) and heating result from the planned cell (Right). It demonstrated that both temperature and lesion region showed a shape of ellipsoid *in-vivo* uterine fibroid study as shown in both phantom and animal studies. The standard deviation for the temperature measurement in untreated regions was 1.2 ±0.4 ℃.

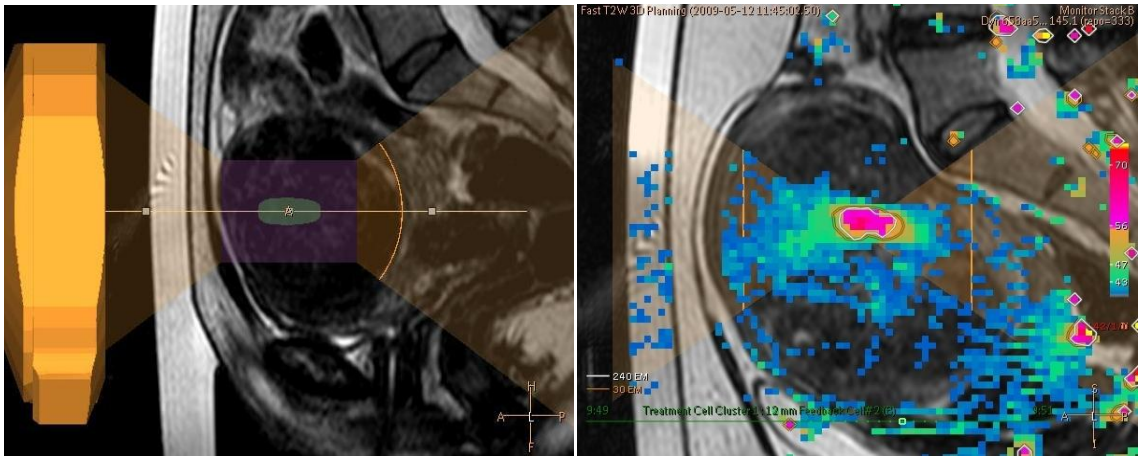

Figure 4.4 One of the examples of MR-HIFU uterine fibroid treatment. Anatomic image (Left) showed the treatment planning in HIFU console on sagittal view for a 16mm cell. The green ellipse showed the cell to be treated. Two transparent yellow cone regions showed both near- and far- filed of HIFU beam. Color encoded temperature map (Right) was overlaid on the magnitude anatomic image. The white contour showed the 240EM.

Fig.4.5 presented the treatment planning and outcome of MR-HIFU uterine fibroid surgery. Planning cells were overlaid on MRI anatomic images in MR-HIFU planning console (coronal: A and sagittal: B) and MRI evaluation of the non-perfused volume (NPV), dark region in uterine fibroid, at ~1 hour after treatment (coronal: C and sagittal: D). The results showed that excellent correspondence between the planned and actual NPV regions.

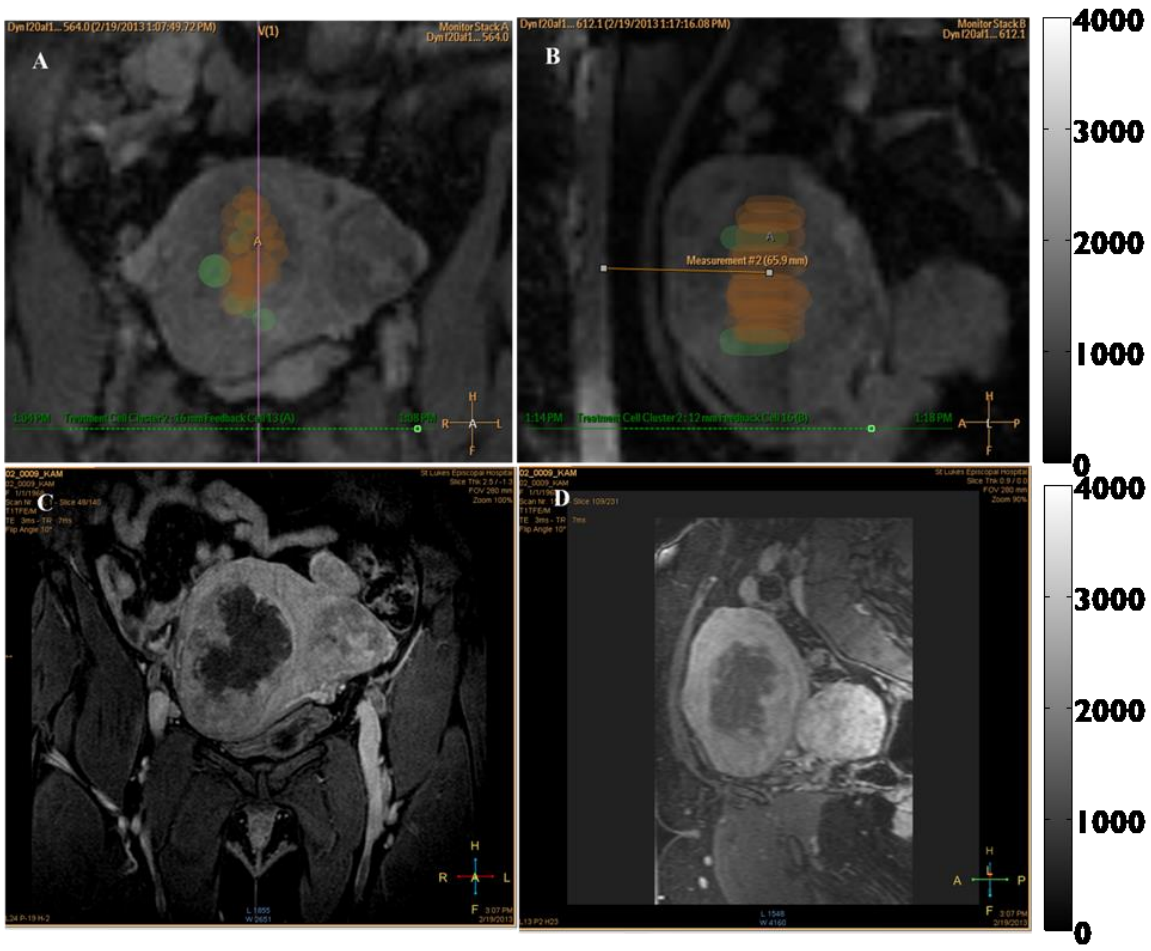

Figure 4.5 One of the examples of MR-HIFU uterine fibroid treatment. The top two anatomic images overlaid with treatment planning were showed in HIFU console (A: Coronal; B: Sagittal). The yellow circles and ellipse showed treated cells while the green circles and ellipses showed the untreated cells. The bottom two images showed the treatment outcome after the contrast enhanced (C: Coronal; D: Sagittal). The field of view of image C and D were: 280×280 mm^2 and 250×250 mm^2 respectively. The images A and B were cropped to better visualize the HIFU cells.

The process of estimating thermal conductivity of uterine fibroid based on a representative HIFU non-feedback sonication of an 8-mm treatment cell is shown in Figure 4.6. The dark circular region in the T_2 weighted coronal image is the uterine fibroid that is targeted for treatment (Fig.4.6A). The temperature elevation during HIFU heating is overlaid on the coronal image (Fig.4.6B); the arrows indicate the location of the heating center (thick arrow) and a representative voxel outside the heated region (thin arrow). The temporal temperature evolutions at these two voxels are plotted in Fig.4.6C. The standard deviation of the temperature (1.2 ±

0.4 ℃) confirmed the precision of the MRI thermometry. The temperature increased during HIFU sonication and then decreased after sonication (Fig.4.6C) as a result of heat conduction and convection. The spatial spread of the temperature map and the quality of the 2D Gaussian fit right after heating is displayed Fig.4.6D. Gaussian-fitted temperature profiles around the trajectory center at 30 (t_1), 54(t_2), and 92 seconds (t_3) after HIFU sonication was discontinued is shown in Fig.4.6E. The temporal evolution of Gaussian variance $\sigma_{xy}^2(t)$ and the associated linear fit are shown in Fig.4.6F. This graph indicates a linear regression in cooling time with goodness of fit ($r^2 = 0.95$).

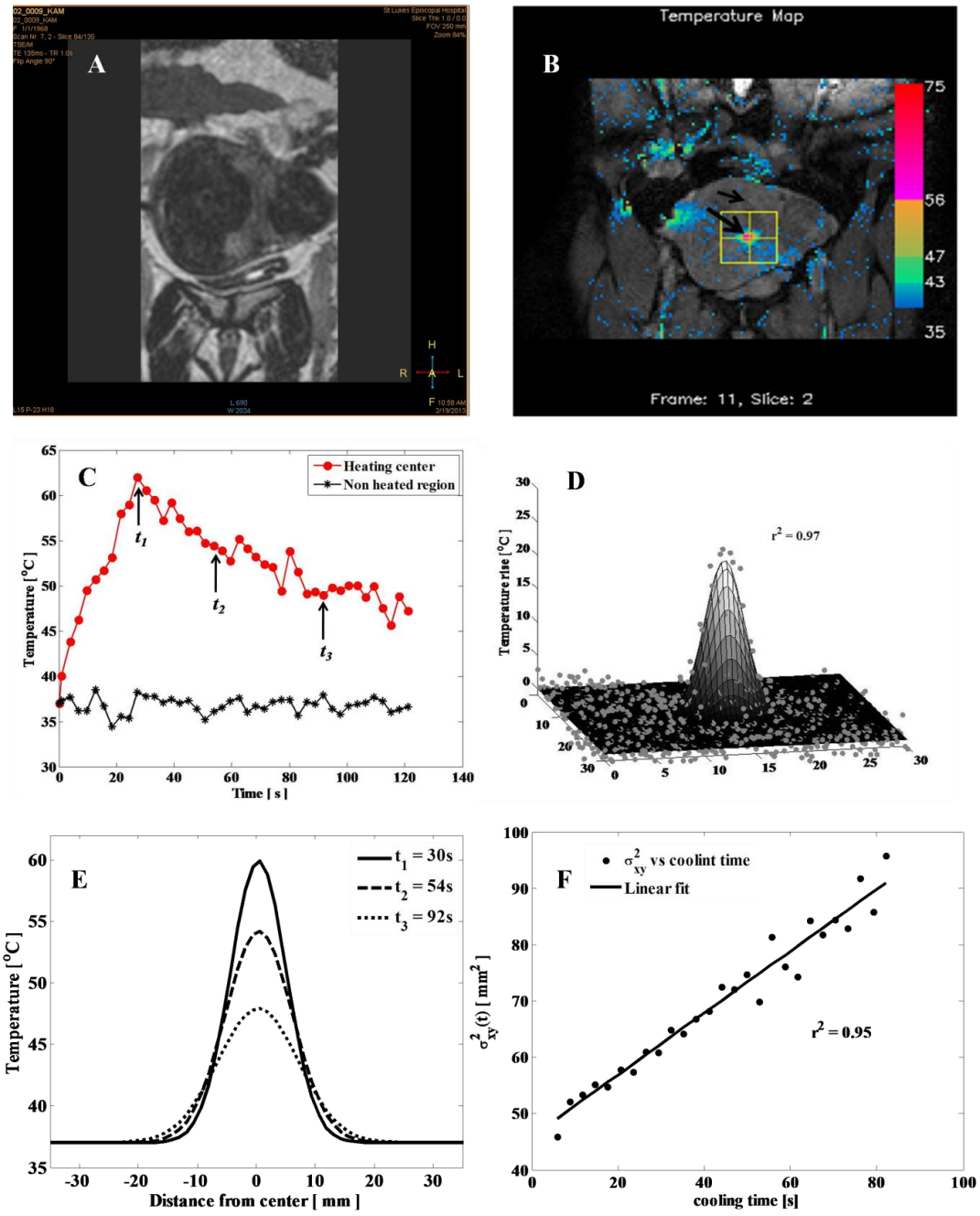

Figure 4.6 Results of a typical HIFU sonication using MRI thermometry. (A) MRI showed the anatomy of the uterine fibroid. (B) Color-coded temperature distribution overlaid on the MRI anatomic image. (C) Temperature evolution at the trajectory center (thick arrow) and the region outside of the heating (thin arrow) arrow in top right image. Time point t_1 corresponds to the point at which the ultrasound was discontinued. (D) Experimental temperature spread (circle) and the associated 2D Gaussian fit right after sonication. (E) Gaussian-fitted temperature profiles across the trajectory center for 3 different time points (indicated in middle left image) during the cooling period. (F) Temporal evolution of $\sigma_{xy}{}^2(t)$ during the cooling period.

The estimated average thermal conductivity of uterine fibroids based on Eq. 4.7 was 0.49 W m^{-1} K^{-1} with a reproducibility of 15.5% (Fig. 4.7). The thermal conductivity of each treated fibroid was shown in table 4.3.

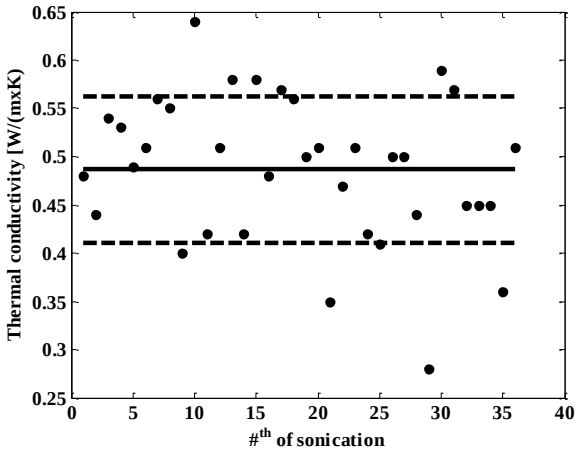

Figure 4.7 Estimated thermal conductivity based on temperature data from 36 sonications performed at our hospital (circles). The solid line shows the mean value for estimated thermal conductivity from different sonications, and the dashed line shows a variation of 15.5% around the average thermal conductivity.

Table 4.3 Estimated thermal conductivity in six fibroids in five women

Fibroids	Body Temperature (°C)	No. of Sonications	Thermal Conductivity *k* W/(m*K)	Std Of *k* W/(m*K)
1	37.1	1	0.45	-
2	37.2	3	0.44	0.08
3	36.9	3	0.49	0.05
4	37.0	7	0.53	0.07
5	37.0	11	0.50	0.08
6	36.4	11	0.47	0.08

4.4 Discussion and Conclusions

Although researchers have proposed several invasive approaches for measuring thermal conductivity *in-vivo*, these methods are limited by an inability to separate the relative contribution of heat conduction and perfusion components[158]. Non invasive approaches such as MRTI do not have this limitation. In the last decade, a few groups have used MRTI methods to measure tissue thermal conductivity. Both Cheng and coworkers [40], and Dragonu and coauthor[154] estimated *in-vivo* thermal conductivity of rabbit leg and *ex-vivo* kidney respectively by inducing a low and moderate temperature increase in tissue without causing tissue coagulation and achieved a reproducibility of ~10% with a precision of 0.2 ℃ for temperature measurement in a non-clinical setting. Therefore, this optimized procedure was well validated for non invasively estimating tissue thermal conductivity at low and moderate temperature. We then further developed this noninvasive procedure under clinical MR-HIFU surgical conditions of higher temperatures necessary for thermal ablation.

We used an *in-vivo* pig model to test the feasibility and precision of measuring tissue thermal conductivity in a high temperature range (60 ℃ ~ 90 ℃) using data sets obtained from clinical MR-HIFU setting procedure[156]. It has been shown that the *in-vivo* estimated thermal conductivity of skeletal muscle of pig is $0.52 \pm 0.05 W\ m^{-1}\ K^{-1}$, which is consistent with reported values. The similar precision (~10%) similar to that described in previous reports [40, 154] has also been achieved under clinical MR-HIFU setting. However the *in-vivo* uterine fibroid thermal conductivity during MR-HIFU surgery has not been estimated and reported yet which is one of the main parameters that govern heat transfer during one of the main clinical applications of MR-HIFU surgery to treat *uterine fibroids*.

We used a clinical MR-HIFU system to ablate the uterine fibroids *in-vivo* and heat the fibroid to a high temperature range (60 ^{o}C ~75^{o}C) to cause tissue necrosis. Each cell (different diameter) was heated to between 60^{o}C and 75^{o}C and then cooled naturally. The spatio-temporal temperature data were then analyzed to estimate the uterine fibroid thermal conductivity. The clinical MR-HIFU surgery set up used in this study had a temperature uncertainty of 1.2 ± 0.4 ℃, a spatial resolution of $2.5 \times 2.5 \times 7$ mm^3, and a temporal resolution of 2.9 seconds. The temperature precision, spatial and temporal resolutions used in this study are lower than previously reported animal studies. For example, Cheng and colleagues, report a temperature precision of 0.2 ℃, for a single slice measurement[151]. The additional safety precautions used in the clinical MR-HIFU surgery system, required simultaneous temperature monitoring of near/far field heating (more slices), and therefore had poorer temporal resolution. Nevertheless, this relatively modest temporal resolution did not hamper the estimation of thermal conductivity from the spatio-temporal temperature profiles during the cooling period. The average estimated uterine fibroid thermal conductivity is 0.49 ± 0.08W·m^{-1}·K^{-1} for these 36 estimations in six fibroids, which is roughly similar to the reported thermal conductivity values for skeletal muscle[159]. The variation of thermal conductivity in uterine fibroids (15.5%) is larger than the reported thermal conductivity measurements in skeletal muscle (10%). However the higher variation of thermal conductivity estimation *in-vivo* in uterine fibroid may be not purely stem from estimation error. We speculate that this thermal conductivity measurement may be affected by the inhomogeneity of the fibroid tissue. The average thermal conductivity for each fibroid was shown in Table 4.3. The mean value in 4th fibroid was higher than the other fibroids. It should be noted that this particular fibroid had a necrotic core (mainly fluid as shown in T_2w image) in center of the fibroid (Fig.4.8). Because the thermal conductivity of pure water at room temperature is 0.61W·m^{-1}·K^{-1}[160] and much higher than the surrounding soft tissue, the effective thermal conductivity of this fibroid was perhaps increased due to presumed contributions from increased

water content. The content of fluid shown in the fibroid was still unknown and thermal conductivity of different liquid can vary from 0.11~0.61W $\cdot m^{-1} \cdot K^{-1}$[161]. However, this hypothesis needs to be further confirmed in the excised fibroid and also in a larger population.

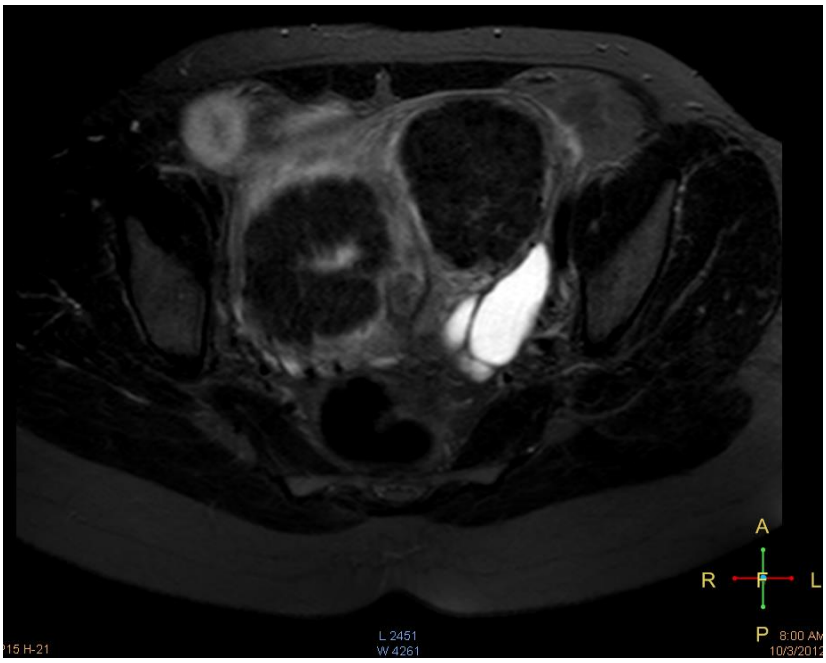

Figure 4.8MRI T_2 weighted image of the 3rd patient before HIFU treatment. Two dominant fibroids got MR-HIFU ablated. The fibroid closer to anterior is the 3rd fibroid and the other one is the 4th fibroid got treated in table 4.2.

Our results indicate that the mean value of thermal conductivity of uterine fibroids is 0.49 $\pm$0.08W $\cdot m^{-1} \cdot K^{-1}$ during the MR-HIFU treatment. The knowledge of uterine fibroid thermal conductivity could be beneficial for planning and optimizing the procedure of MR-HIFU uterine fibroid ablation. For example, the measured thermal conductivity information could be incorporated into algorithms used for optimizing the rate and the amount of thermal energy should be delivered. Furthermore, thermal conductivity information could also help researchers to design optimal thermal-dose delivery mechanisms that would administer just the necessary amount of thermal energy, help avoid overheating, and potentially minimize unwanted heating, particularly in the near field of the HIFU beam. Though thermal conductivity of uterine fibroid is

estimated from MR-HIFU procedure, it can also be used in optimizing other thermal ablation techniques in which thermal energy is used to ablate tumor like RF ablation, laser ablation and so on. On the basis of this preliminary experience with *in-vivo* uterine fibroid ablation, one can speculate that it may be possible to calculate such bio-heat properties during MR-HIFU surgery in patients. This hypothesis needs to be validated in a larger clinical study.

However, we wish to point out that the estimated *in-vivo* thermal conductivity is an average effect of the actual thermal conductivity for the time course spanning a few tens of seconds (~60 s) in the high temperature range (60^{o}C~75^{o}C) after the tissue is dead (ie, after a 240-EM thermal dose has been reached). In extrapolating the results from this study, one should carefully consider the following assumptions in our model: 1) in the analysis, we assumed that the local tissue was homogeneous, which may not be true in all cases; 2) tissue density, specific heat, diffusivity, and perfusion while (this technique is independent of perfusion) were considered constant, but they could have been sensitive to instantaneous changes in local temperature to varying degrees. In the initial clinical uterine fibroid ablations with MR-HIFU that we studied, these assumptions were likely to have been true due to the highly localized and a relatively brief ablation process associated with HIFU surgery.

In conclusion, this preliminary clinical study of MR-HIFU uterine fibroid therapy and *in-vivo* animal study show that:

1) It is possible to noninvasively estimate local tissue thermal conductivity *in-vivo* in a range of high temperatures (60 ℃ ~ 90 ℃).
2) The thermal conductivity of *in-vivo* uterine fibroid and pig thigh muscle at these high temperatures are $0.49 \pm 0.08 W\ m^{-1}\ K^{-1}$ and $0.52 \pm 0.05\ W\ m^{-1}\ K^{-1}$ respectively, and

3) Variation of thermal conductivity of uterine fibroid estimated using MR-HIFU is in the range of 15.5% and 10% for uterine fibroids and pig thigh muscle respectively.

Chapter 5

Tissue Blood Perfusion Response during MR-HIFU

5.1 Introduction

The absorbed thermal energy of MR-HIFU in the target is transferred to adjoining regions through two mechanisms: thermal conduction and thermal convection (blood perfusion) in the tissue. The tissue thermal conductivity and blood perfusion and their responses to the local heating will determine the temperature distribution during sonication and cooling period and thus affect the efficiency and effectiveness of the treatment. Tissue thermal conductivity and its response to HIFU heating was studied in Chapter 4. In this chapter we are focus on the tissue blood perfusion and its thermal response to the HIFU heating.

Blood perfusion rate in microcirculation including the capillary network plus small arterioles and venules of less than 100μm in diameter, is usually referred to as perfusion (defined as the blood flow rate per unit tissue volume). In addition to the effect in thermal convection during thermal therapy, blood perfusion also plays an important role in the local transport of oxygen, nutrients, pharmaceuticals, and heat through the body. Measurements of tissue blood rate are of importance in a wide variety of clinical areas including disease diagnostics, drug studies, and cancer hyperthermia[162]. Despite its clinical significance, there is no simple way to measure local perfusion.

Blood perfusion rate in normal tissue (such as skin and muscle) has been shown to have the ability to increase by a factor of 3~20 under hyperthermia heating (<45^{o}C) [46] by water bath. This will greatly affect the efficiency of heat dissipation in thermal ablation. However, the behavior of blood perfusion rate in a small volume under extreme therapeutic temperature

conditions (>60^{o}C) characteristic of HIFU surgery is still largely unknown. For instance, it has been found that regions adjoining the HIFU treated areas show no necrosis [163]. This further emphasizes the need for understanding the physiological response of not only in the normal tissue but also tumor. The *in-vivo* evaluation of physiological response of blood perfusion can, in turn, serve as a feedback for developing patient (tissue)-specific MR-HIFU surgical strategies

In this chapter, we focus on characterizing the local blood perfusion rate behavior in the therapeutic temperature level (>60^{o}C) identical to that of MR-HIFU thermal treatment of the pig muscle in Chapter 4. We use numerical methods to simulate the experimental spatio-temporal temperature distribution of pig muscle tissue treated by MR-HIFU. We found that a fast temperature-dependent perfusion rate is necessary to account for the time evolution of the temperature of the entire period of HIFU treatment. The constructed model was then applied to characterize blood perfusion behavior during *in-vivo* uterine fibroid treatment using MR-HFIU. The temperature-dependent blood perfusion rate was found to be necessary to describe temperature evolution through MR-HIFU procedure. This indicated that a proper target temperature can optimized to avoid excess heat dissipation by blood perfusion during thermal ablation.

5.2 Theory

We used bio-heat transfer equation to describe the spatio-temporal temperature evolution in tissue in the absence of large-vessel flow according to the following equation[127]:

$$\rho_t c_t \frac{\partial T(\vec{r},t)}{\partial t} = k_t \nabla^2 T(\vec{r},t) - \rho_b c_b \omega (T(\vec{r},t) - T_a) + Q_{met} + Q_{ext} \qquad (5.1)$$

where $T(\vec{r},t)$ is the tissue temperature at time t and location $\vec{r}$; ρ_t, c_t, and k_t are tissue density, specific heat, and thermal conductivity, respectively; ρ_b, c_b, and ω_b are blood density, specific heat, and perfusion rate respectively; T_a is the arterial blood temperature; Q_{met} is tissue metabolic rate, and Q_{ext} is the power deposition per unit volume by the external heat source (HIFU energy in case of MR-HIFU surgery). It should be noted that in this dissertation the above Eq. 5.1 is used to describe the collective thermal effect for tissues not in the immediate vicinity of large blood vessels and does not account for the directional convective heat loss due to blood flow from such large blood vessels.

In Chapter4 we showed that the temperature dependence of the thermal conductivity of the pig muscle under HIFU ablation conditions is negligible, therefore only the heat convection is still unknown in bio-heat transfer equation. Two models were considered for evaluating the blood perfusion rate behavior in this numerical study for MR-HIFU thermal surgery[164]: *Constant Blood Perfusion rate* (CBP) and *Temperature-dependent Blood Perfusion rate* (TBP) were used to simulate the heat convection by blood perfusion. In the model of CBP, the blood perfusion rate was assumed to be invariant (and equal to baseline blood perfusion values reported in the literature) during the HIFU treatment while the blood perfusion rate was assumed to be temperature-dependent for TBP model.

5.3 Simulation of in-vivo MR-HIFU Experiments

Geometric model

To simulate the HIFU heating during the treatment, a geometric model that accounts for the characteristics of HIFU heating was built. In particular, to mimic the heat energy as deposited by a volumetric heating, an ellipsoidal heat source (Table 5.1) representative of various cell sizes

used in MR-HIFU therapy were considered [72, 157]. To simulate the HIFU heating we used a constant power heat source of ellipsoid shape identical to that used in the experiments (Table 5.1).

Table 5.1 Heating source dimension used in the simulation

Ellipsoid cell dimension	4-mm	8-mm	12-mm	16-mm
Semi-short axis(mm)	2	4	6	8
Semi-long axis (mm)	5	10	15	20

The dimension of simulated region including the heating source and normal tissue region were chosen to make sure that the temperature on the boundary would not affect the temperature distribution inside the region close to the heating source. This assumption is valid as the HIFU heat source was highly localized and if the heating location was away from the skin surface or other large arteries. Both these conditions are satisfied in clinical MR-HIFU therapy Other specifics about the geometric model used in the numerical simulations are shown in Fig. 5.1. Temperature region for bio-heating transfer model was a cylinder of dimension 50mm in radius and 80mm in height which is large enough compared to the biggest HIFU cell (16-mm). The shape of HIFU heating source is simulated as an ellipsoid and its dimension was shown in Table 5.1 depending on the size of HIFU cell used in the experiments[126, 156, 157].

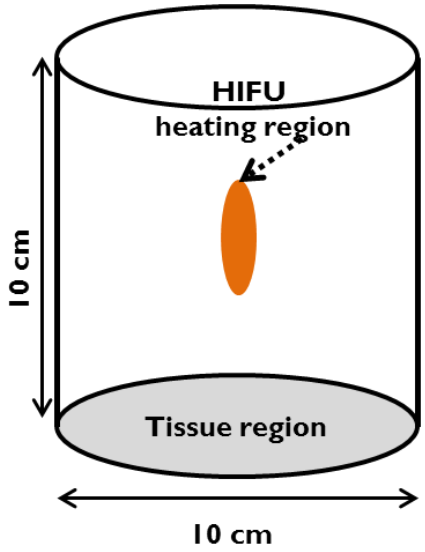

Figure 5.1 Geometric model used in this bio-heat transfer model for simulating the spatio-temporal temperature distribution from HIFU heating

Boundary condition

Heat flux condition was applied on the cylinder surface served as an air-tissue interface.

$$\boldsymbol{n} \cdot (k\nabla T) = q_0 + h(T_{ext} - T) \tag{5.2}$$

where $\boldsymbol{n}$ is the normal vector to the surface, k is tissue thermal conductivity, T and T_{ext} are tissue temperature and the air temperature or room temperature (21^{o}C in our experiment) respectively, h is heat transfer coefficient between air and tissue. q_0 is a general heat flux entering the tissue and thus is zero in this simulation.

The continuity condition was applied on all the interior boundaries:

$$-\boldsymbol{n_{up}} \cdot (\boldsymbol{q}_{up} - \boldsymbol{q}_{down}) = 0 \tag{5.3}$$

This means that the heat flux in the normal direction of boundary surface is continuous across the boundaries. $\boldsymbol{q}_{up}$ and $\boldsymbol{q}_{down}$ are the heat flux leaving and entering to the boundary surface respectively. Bio-heat transfer equation was solved for spatio-temporal temperature distribution

as observed *in-vivo* animal studies in the whole domain including heating and non heating regions (3D volume) based on two different perfusion models: *CBP* and *TBP*.

Tissue parameters

All other parameters used in the simulation used realistic, common values for human tissue[165, 166]. Density (ρ, 1060kg m^{-3}) and specific heat (c, 3600 J kg^{-1} K^{-1}) of both tissue and blood are assume to be the same. Arterial blood temperature (T_a) is 37^{o}C. Initial temperature of HFIU target and surrounding regions was given as experimentally measured oral temperature (uterine fibroid treatment) and rectal temperature (pig study). The heat transfer coefficient (h) between air and skin was 10W m^{-2} K^{-1}. The metabolic rate of muscle tissue (Q_{met}) is 745W m^{-3}. However this low metabolic heat rate can be ignored compared to externally applied therapeutic HIFU energy. Tissue thermal conductivity (k_t) was obtained from experimentally measured value for each cell described in Chapter 4.

5.3.1 Simulation of *in-vivo* MR-HIFU Animal Studies

The spatial-temporal temperature in cylinder and ellipsoid regions were calculated by the finite element method using COMSOL Multiphysics software (v3.5a COMSOL Inc., California, USA). For simulating heat transfer in each cell during HIFU thermal ablation, experimental cell diameter, and HIFU heating duration were used as inputs and the maximum temperature during HIFU experiment was used as a target temperature. The external applied heat source (Q_{ext}) was iteratively updated till the simulated maximum temperature reached the target experimental temperature (error <0.2^{o}C).

Constant Blood Perfusion rate model (CBP)

In the CBP model, blood perfusion rate (ω) in tissue was assumed to a constant during both HIFU heating and cooling period and the value was set to be 7.95×10^{-4} s^{-1} which is the value of base blood perfusion rate (ω_0) of muscle tissue at rest and at body temperature.

Temperature-dependent tissue blood perfusion rate model (TBP)

In the TBP mode, blood perfusion rate (ω) was assumed to be temperature-dependent.

$$\omega(T) = \omega_0 + \omega_T \tag{5.4}$$

The 1st term (ω_0) in the right of above equation is the based on blood perfusion rate at rest and at body temperature which is set to be the general blood perfusion rate (7.95×10^{-4} s^{-1}) for muscle and uterine fibroid tissue. The 2nd term ω_T is the temperature-dependent blood perfusion rate. The temperature-dependent blood perfusion rate during MR-HIFU experiment was divided into two time periods: heating and cooling period. In the heating period, temperature-dependent blood perfusion rate term ω_T is zero if the temperature is less than 45°C otherwise it increase linearly with temperature as shown in Eq. 5.5.

$$\omega_H(T) = \begin{cases} \omega_0, T \le 45^o C \\ \omega_0 + 3.77\times10^{-4}\times(T - 45^o C), T > 45^o C \end{cases} \tag{5.5}$$

Here the slope of perfusion (3.77×10^{-4} s^{-1}) increase was calculated based on the assumption that the blood perfusion increase by 20 times of the base perfusion of muscle tissue when temperature increases to 85^oC. However, this slope may be different for different types of tissue and needs to be verified for each specific tissue.

In the cooling period, blood perfusion rate was assumed to decrease linearly with falling temperature until 60°C and simultaneously the blood perfusion rate also drops to the base blood

perfusion rate ω_0 (Eq. 5.6). The blood perfusion rate is assumed to decrease faster than the heating period due to account for the fact that target 'cell' has been killed right after the delivery of lethal thermal dose(Thermal dose of 240EM was reached).

$$\omega_C(T) = \begin{cases} \omega_0, & T_{max,H}(\vec{r}) \le 45^oC \\ \omega_0 + 3.77 \times 10^{-4} \times (T - 45^oC), & 45^oC < T_{max,H}(\vec{r}) \le 60^oC \\ \omega_0 + u(\vec{r}) \times (T - 60^oC), & T_{max,H}(\vec{r}) > 60^oC \end{cases} \quad (5.6)$$

Where $u(\vec{r})$ is the slope of blood perfusion rate change with temperature. Here $T_{max,H}(\vec{r})$ was the temperature right after HIFU heating at position $\vec{r}$.

$$u(\vec{r}) = \begin{cases} 0, & T \le 60^oC \\ 3.77 \times 10^{-4} \times \left(1 + \dfrac{15^oC}{T_{max,H} - 60^oC}\right), & T > 60^oC \end{cases} \quad (5.7)$$

Simulation results

We compare the effectiveness of the two models for blood perfusion rate in simulating HIFU thermal ablation using a 16-mm cell in pig thigh muscle tissue (3.7~5.4cm below skin layer). Heating duration was 65.11s. The reached maximum temperature was 86.3^{o}C. The applied acoustic power and frequency of HIFU were 140W and 1.2MHz respectively. Temperature evolution under the CBP and TBP models is shown in Fig. 5.2 and 5.3 respectively. The black dots were the experimental temperature evolution data at HIFU heating center. The green, cyan, red and blue dots showed the experimental temperature evolution at position of one pixel (2.5mm) above, left, below and right of the heating center respectively. The blue solid line showed the simulated temperature evolution at heating center while the black solid line showed the simulated temperature evolution at 2.5mm away from heating center. The blood perfusion rate at heat heating center was plotted at different time from TBP model in Fig. 5.4.

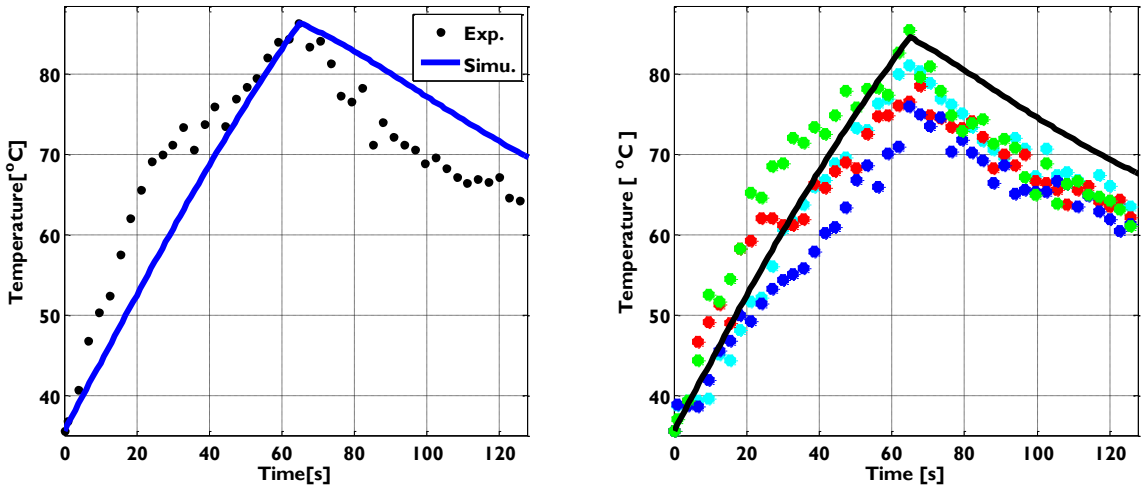

Figure 5.2 . Temperature evolution at heating center as predicted by the CBP model (solid blue line) compared against experimental measurement of temperature (Left) . The image on the right demonstrates the predicted temperature evolution under the CBP model (solid line) for pixels that are 2.5 mm away from the heating center (1 pixel distance) is shown on the right. The goodness of fit between simulation and experiment was: r^2 = 0.69, SSE = 2012.8.

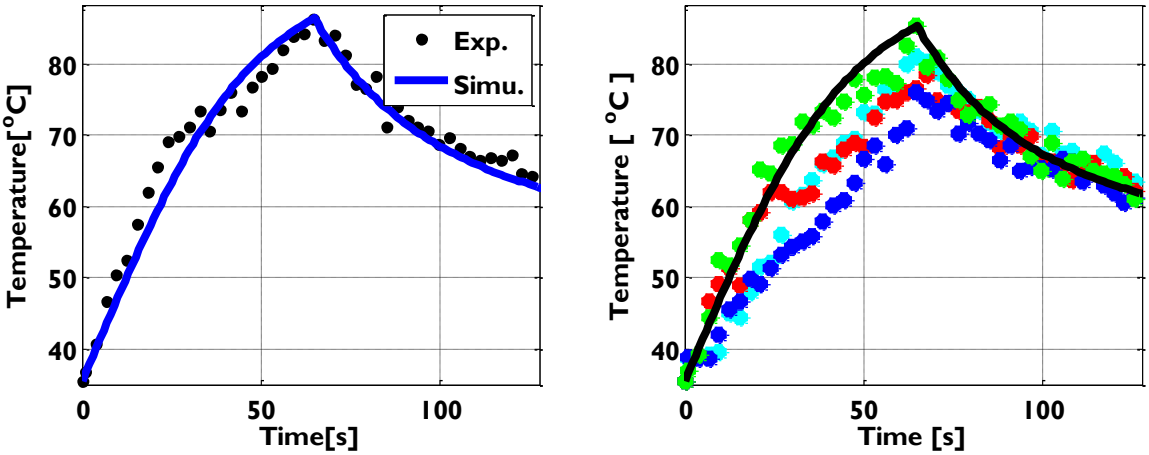

Figure 5.3 Simulation result using TBP model. Temperature evolution at heating center (Left) and 2.5mm away (Right) from heating center of both simulation (solid line) and animal experiment (dot) were compared. The goodness of fit between simulation and experiment was: r^2 = 0.95, SSE = 309.3.

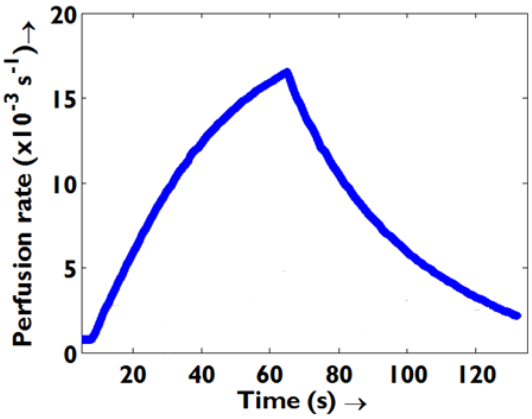

Figure 5.4 Blood perfusion rate evolution at different time in TBP model for this specific HIFU heating cell simulation.

Goodness of fit r^2 (Eq.4.8) and the summed square of residuals (SSE) (Eq. 5.8) in statistics[167] were used to evaluate which model for blood perfusion rate was better in predicting the experimental temperature evolution data.

$$SSE = \sum_{i=1}^{n} w_i (y_i' - y_i)^2 \tag{5.8}$$

Where y_i, y_i', and w_i are test data, fitted data, and weights of the test data respectively. A *SSE* value closer to 0 indicates that the model has a smaller random error component, and that the model will be more useful for prediction.

As calculated based on Eq. 4.8 and 5.8, r^2 = 0.69, *SSE* = 2012.8 and r^2 = 0.95, SSE = 309.3 corresponded to CBP and TBP models respectively for this HIFU heating of 16-mm cell. This result showed that TBP model is much better than CBP model. While the temperature evolution predicted by the CBP model showed some agreement with experimental measurements during the heating period, there was little correlation during the cooling period. The experimental temperature measurements decreased much faster than the CBP model during the

cooling period when heat transfer was purely governed by thermal conduction and convection through blood perfusion in the absence of external heat deposition.

To compensate for this rapid energy loss due to convection by blood perfusion, a temperature-dependent blood perfusion model (TBP) was introduced. TBP model-based temperature predictions matched with experimental data both in heating and cooling periods very well. By looking at the perfusion evolution at heating target (Fig. 5.4), the blood perfusion rate increases rapidly during the very short heating period (~65s). In order to compensate the energy loss due to convection, a large blood perfusion rate increased up to ~20 times of the base blood perfusion rate value in this case. The rate of blood perfusion rate decrease in cooling period is higher than the rate of blood perfusion rate increase in heating period. This is perhaps due to the destruction of vasculature in the target region. From energy point of view in this specific cell treatment, the simulated thermal energy for TBP and CBP model were 2.92×10^{8}J m^{-3} and 2.12×10^{8}J m^{-3} respectively. In other words, the models suggest that 38% more energy was needed to reach the target experimental temperature due to heat dissipation because of large increase of blood perfusion rate. From a MR-HIFU treatment point of view, this physiologic response of blood perfusion rate increase during heating may result in decreased efficiency of HIFU thermal ablation. A similar trend of temperature-dependent perfusion rate changes during HIFU heating and cooling time was also observed during the thermal ablation of a 12 mm cell. However, the applied thermal energy for TBP and CBP models were 1.68×10^{8}J m^{-3} and 1.48×10^{8}J m^{-3} respectively. The applied thermal energy difference showed a smaller discrepancy (13.5%) compared to the 16mm-cell. This suggests that for a 12 mm cell, less energy was dissipated through blood perfusion rate.

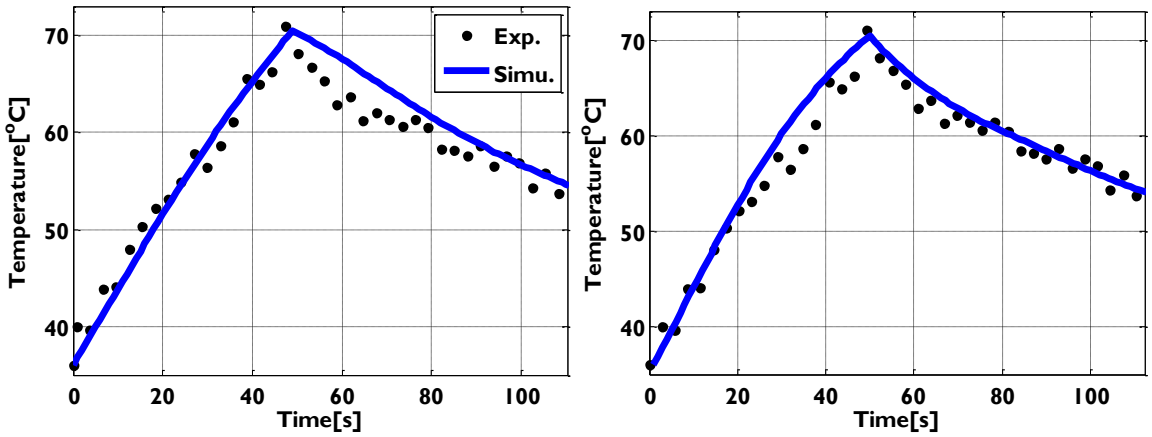

Figure 5.5 Simulation result of a 12-mm HIFU cell using both CBP (Left) and TBP (Right) models. Temperature evolution at heating center between simulation (blue solid line) and animal experiment (black dot) was compared. The goodness of fit of simulation of experiment was: r^2 = 0.95, SSE = 119.9 for TBP model and r^2 = 0.92, SSE = 189.4 for CBP model.

Along the same lines, the numerical predictions and experimental observations with respect to MR-HIFU treatment of a 8 mm cell, showed that the applied thermal energy of the CBP model was within 6% of the predictions by the TBP model (Applied thermal energy 1.81×10^{8}J m^{-3} and 1.71×10^{8}J m^{-3} for TBP and CBP models respectively.). Curiously, from a model perspective, for MR-HIFU treatment of a 8 mm cell, CBP model appears to perform slightly better than TBP model (r^2 = 0.86, SSE = 367.8 for CBP model and r^2 = 0.84, SSE = 432.5 for TBP model respectively) (Fig. 5.6). The slight difference between CBP and TBP models indicates that the blood perfusion rate of temperature dependence may be not necessary to account for the heating profile during HIFU thermal ablation or the blood perfusion rate did not respond to this specific HIFU heating although the peak temperatures exceeded 70 ^{o}C to treat about 0.7 mL of tissue. This finding suggests that there may be a threshold of volume at risk before the compensatory mechanism of perfusion response is triggered to prevent tissue damage. However this point needs to be confirmed by more investigations.

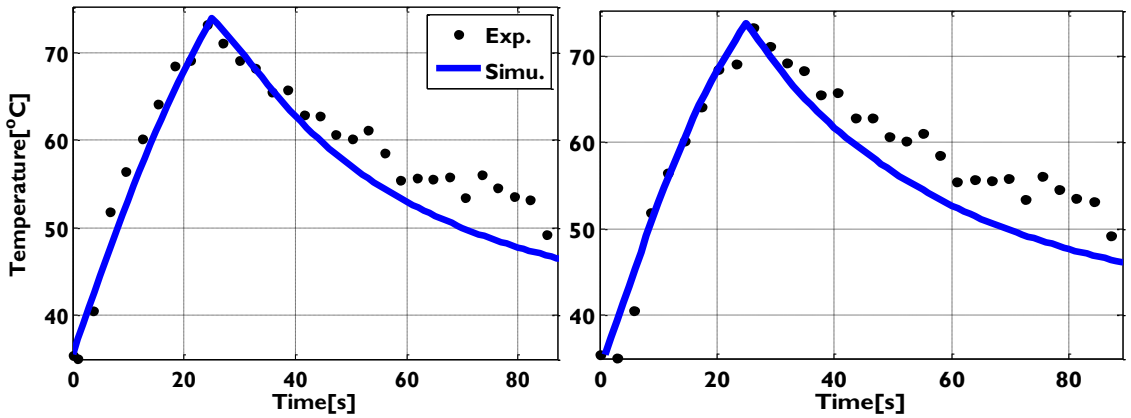

Figure 5.6 Simulation result of a 8-mm HIFU cell using both CBP (Left) and TBP (Right) models. Temperature evolution at heating center between simulation (blue solid line) and animal experiment (black dot) were compared. The goodness of fit of simulation of experiment was: r^2 = 0.84, SSE = 432.5 for TBP model and r^2 = 0.86, SSE = 367.8 for CBP model.

5.3.2 Simulation of *in-vivo* MR-HIFU Uterine Fibroid Studies

Several clinical studies have reported that while there is some general agreement between the thermal dose volume measured at the time of MR-HIFU surgery and the eventual size of the non-perfused volume (NPV), it is difficult to predict eventual tissue damage based on the thermal dose volume. For example some regions in uterine fibroid can't be treated even using high HIFU acoustic power[163], while in other cases, a small thermal dose volume measured at the time of ablation causes a substantially large area of NPV in the final imaging We speculate that the explanation for such outcomes may lie in understanding the tissue thermal properties, particularly the tissue thermal conductivity, and perfusion response to heating. In this section, we apply the model developed in the previous section to human *in-vivo* MR-HIFU treatment of uterine fibroids.

In this section, we focused on charactering the behavior of blood perfusion in one of the clinical application of HIFU ablation of uterine fibroid *in-vivo* in women using numerical method same as

used in animal studies. A total of nine women patients were treated under the same procedure of MR-HIFU platform. Five of them were treated in St Luke's Episcopal Hospital (Table 4.2) and the other four were treated in University of Chicago Medical Center (Table 5.2).

Table 5.2 Summary of MR-HIFU experiment completely performed in each patient.

Patient	Body Temperature (^oC)	No. of Sonications	Maximum Temperature (^oC)	Power (W)	Duration (sec)
1	36.2	12	64.7~73.6	130~160	15.7~47.9
2	35.8	21	64.5~70.9	170	10.8~25.0
3	36.6	12	63.5~74.9	120~160	19.1~33.3
4	36.1	25	68.1~79.9	160~200	18.6~34.3

Spatio-temporal temperature distribution from these *in-vivo* clinical MR-HIFU uterine fibroid treatments were used to simulate the blood perfusion rate and its response to HIFU heating using various cell size.

Again CBP and TBP models for blood perfusion rate were used to simulate heat convection during HIFU treatment using bio-heat transfer equation. Representative results from the application of CBP and TBP models on the experimentally measured temperature on a 16 mm cell, are shown in Fig 5.7. It should be noted that the thermal conductivity of the *in-vivo* uterine fibroid was calculated (as described in Chapter 4), and the experimentally determined thermal conductivity value ($0.48 W \cdot m^{-1} \cdot K^{-1}$ for this specific HIFU cell) was used in the numerical simulation. The black dots show the HIFU experimental temperature evolution at the trajectory center. The blue lines show the simulated temperature evolution at heating center. In this specific 16mm cell, CBP model (Left) appears clearly inadequate to describe the experimental thermal distribution ($r^2 = 0.37$). This means the assumption of CBP model for blood perfusion rate both in heating and cooling period was not proper.

While TBP model (Right) was better than the CBP model to account for the temperature evolution during heating and cooling, the model was clearly inadequate to fully characterize the perfusion response of the tissue. For example, while the experimental data fitted well with numerical simulations during the cooling period, TBP model did not accurately capture heat convection during the heating period. In this model, we assumed the baseline blood perfusion values from the skeletal muscle, and the temperature-dependent perfusion behavior of healthy muscle tissue. Both these assumptions may be invalid for the *in-vivo* fibroid tissue, and may need to be adjusted to accurately account for the temperature evolution. The applied thermal energy between these CBP and TBP models were 1.60×10^{8}J m^{-3} and 1.80×10^{8}J m^{-3} respectively.

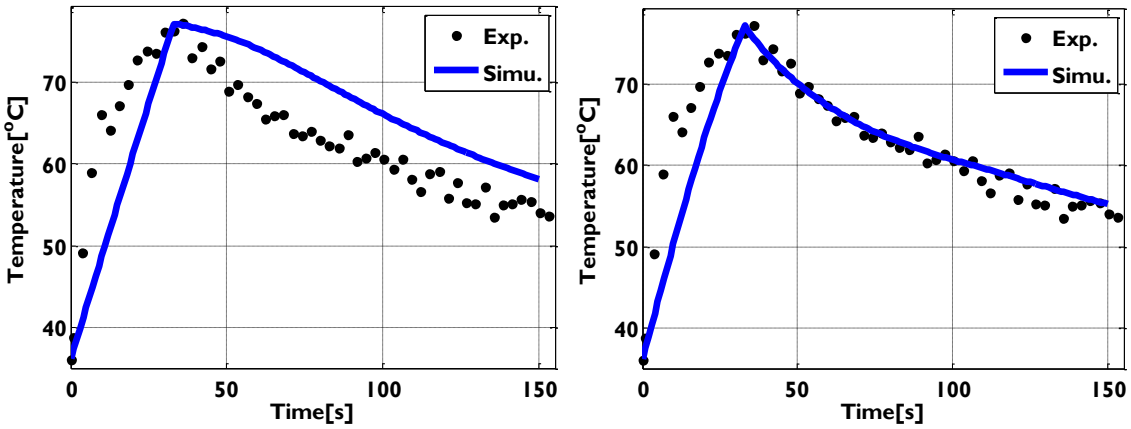

Figure 5.7 Simulation result of a 16-mm HIFU cell using both CBP (Left) and TBP (Right) models. Temperature evolution at heating center between simulation (blue solid line) and animal experiment (black dot) were compared. The goodness of fit of simulation of experiment was: r^2 = 0.37, SSE = 2446.0 for CBP model and r^2 = 0.77, SSE = 894.4 for TBP model.

While simulation for a smaller HIFU cell of 12mm heating was shown in Fig. 5.8 and indicated that TBP model (Right) still performed better than CBP model (Left) overall especially in temperature ranges above 60°C in which the rate of blood perfusion increase was conspicuous in the assumption of TBP model. This TBP model also indicated that heat convection during the heating period was a little bit different from ablation of healthy muscle tissue. But this is good for cooling period in which heat transfer was only governed purely by blood perfusion and thermal

conductivity. Applied thermal energy between these CBP and TBP models were 1.35×10^{8}J m^{-3} and 1.52×10^{8}J m^{-3} respectively to reach the experimental target temperature.

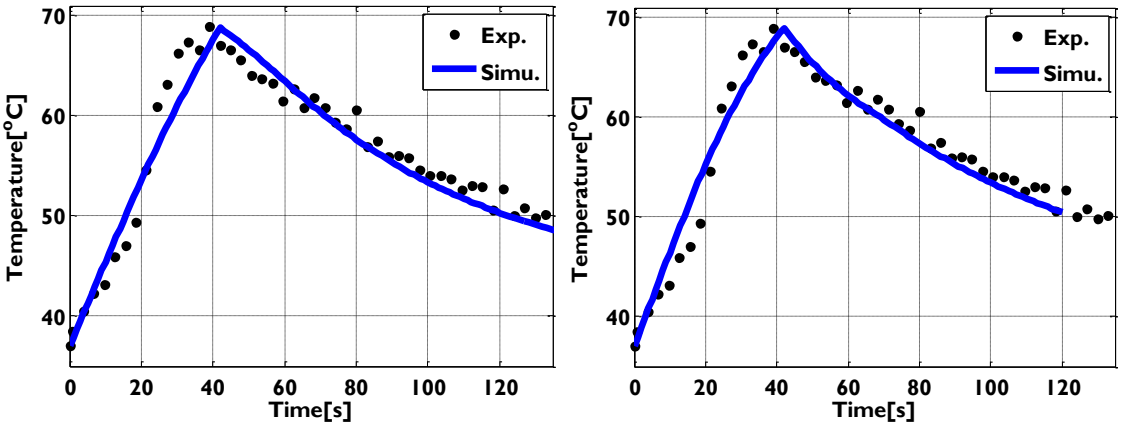

Figure 5.8 Simulation result of a 12-mm HIFU cell using both CBP (Left) and TBP (Right) models. Temperature evolution at heating center between simulation (blue solid line) and animal experiment (black dot) were compared. The goodness of fit between simulation and experiment was: r^2 = 0.94, SSE = 176.8 for CBP model and r^2 = 0.95, SSE = 155.4 for TBP model.

Similar to the case in simulating 8mm HIFU cell of ablating muscle tissue in animal study, TBP model (Fig. 5.9, Right) did not show any better charactering heat convection by blood perfusion rate *in-vivo* in uterine fibroid treatment compared to CBP model (Fig. 5.9, Left). The applied thermal energy between CBP and TBP models were 1.35×10^{8}J m^{-3} and 1.44×10^{8}J m^{-3} respectively. The applied energy difference was less than 7% which showed only a slight difference.

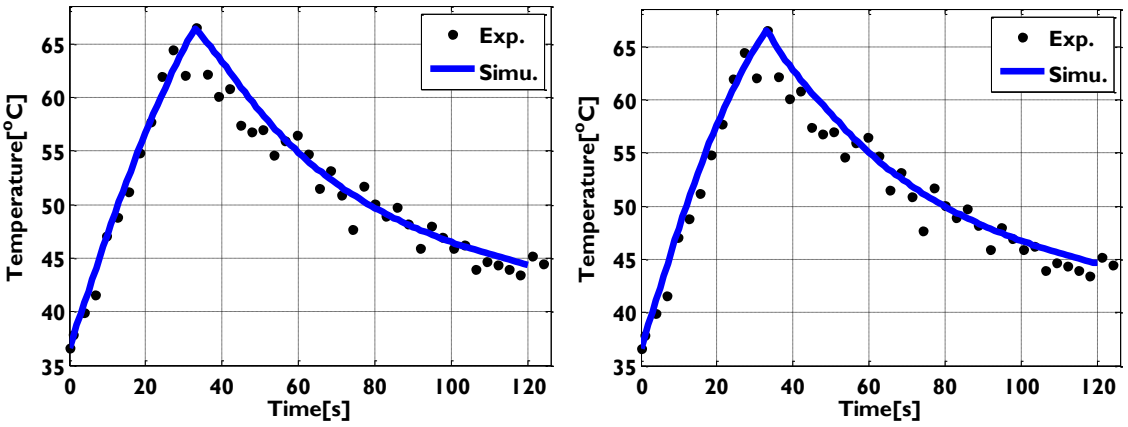

Figure 5.9 Simulation result of a 8-mm HIFU cell using both CBP (Left) and TBP (Right) models. Temperature evolution at heating center between simulation (blue solid line) and animal experiment (black dot) were compared. The goodness of fit between simulation and experiment was: r^2 = 0.95, SSE = 111.3 for CBP model and r^2 = 0.95, SSE = 117.9 for TBP model.

From theoretical applied energy point of view *in-vivo* in HIFU uterine fibroid treatment, needed theoretical energy of TBP model was around 13% more compared to CBP model using from 12-mm to 16-mm HIFU cell. As for 8mm cell, TBP model didn't perform better than CBP model. This treatment volume threshold for triggering a perfusion response in tissues has not been reported previously, and needs to be investigated further.

5.4 Discussion and Conclusions

The effect of blood perfusion rate on the temperature distribution introduced by focused ultrasound in a controlled dog's kidney model was studied using both experimental and numerical methods[52, 53]. This study showed two effects during the focused ultrasound thermal ablation: 1) magnitude of the temperature elevation; 2) the temperature distribution pattern produced at a given power level. These effects were further studied *in-vivo* in HIFU ablation of rat liver parenchyma at normal blood flow and reduced blood flow by ligating hepatic artery or portal vein[168]. The lesion diameter with normal blood perfusion rate was reduced by 14% ~ 20% depending on the heating duration. This effect has been studied in RF ablation[169]. The vasoactive

drug (hydralazine) was administered before RF ablation to decrease blood perfusion rate in entire tumor and tumor rim (~30%) and the introduced coagulated area was found to increase greatly. In the clinical HIFU surgery of uterine fibroid, a postsonication temperature decay rate was used to predict the therapeutic outcome [170]. Though the correlation between blood perfusion rate and temperature evolution during cooling period was not discussed in this study, it was closely related to the blood perfusion rate since the postsonication temperature drop was governed by heat convection. This indirectly indicated the blood perfusion change and thus affected the necrosis area.

Various models (constant and temperature-dependent blood perfusion rate) have been proposed to simulate the blood perfusion rate in hyperthermia condition in which temperature varied from 40^{o}C to 45^{o}C[171]. However the mechanism of blood perfusion and its response to thermal surgery was still largely unknown.

In this chapter, two blood perfusion models (constant blood perfusion and temperature-dependent perfusion) were proposed to simulate the blood perfusion rate and its response at therapeutic temperature level during HIFU ablation of both healthy pig thigh muscle *in-vivo* and women uterine fibroid *in-vivo*. Spatio-temporal temperature distribution calculated using TBP model for simulating blood perfusion rate was shown to be able to account for the HIFU experimental temperature evolution using large HIFU cell (12-mm and 16-mm). But TBP model did not perform better than CBP model for simulating smaller HIFU cell (8-mm). The possible reasons are: 1) blood perfusion rate dependent effects are not triggered to increase for heating a small volume or in other words a volume of temperature change is too small to cause conspicuous physiological response; 2) Temperature measurement error was too big to detect the effect from blood perfusion rate increase in 8mm cell if it was triggered since the temperature measured error increase as the dimension of HIFU cell decrease as shown in Chapter 3. More studies including

both HIFU experiment and simulation needs to be performed to confirm these preliminary observations.

Some of the assumptions/limitations in the TBP model may be addressed as follows: : 1) Optimize current temperature measurement protocol so as to improve the temperature accuracy and precision (Chapter 3); 2) For each uterine fibroid that is under consideration for being treated, the baseline perfusion rate may be determined independently prior to ablation (e.g., during the screening phase), and this value could be used in the model; and 3) Although not possible in the current experimental design, HIFU experiments can be performed on the same fibroid during two different perfusion states (e.g., during *in-vivo*, and during *ex-vivo* after hysterectomy)) Experimental and simulation temperature evolution data at both *in-vivo* and *ex-vivo* can be compared to see whether blood perfusion is triggered and whether the TBP model is necessary to account for the heat convection in HIFU heating a small volume since no perfusion effect in *ex- vivo* studies.

We want to point out that assumptions in TBP model were specific to HIFU-based thermal ablation: 1) blood perfusion rate starts to increase above temperature of 45^{o}C; 2) the blood perfusion is assumed to linearly increase with temperature; 3) higher rate of blood perfusion rate change in cooling period than heating period is assumed; 4) the blood perfusion quickly drops to the base blood perfusion rate once the temperature drops to below 60^{o}C. These assumptions were made based on the characteristics of HIFU heating: high power (>100W) and short duration (~1min) of heating. These assumptions for temperature-dependent blood perfusion need to be reconsidered if other types of heating method like RF heating, laser heating etc. are used. Furthermore, it should be noted that base blood perfusion rate and rate of blood perfusion rate increase used in this simulation are for health normal muscle tissue. As for other type of tissue, this value may need to be changed accordingly. This may also explain that bigger error

was shown in TBP model for uterine fibroid *in-vivo* HFIU treatment than the animal study. The inhomegenity of base blood perfusion rate inside the uterine fibroid also needs to be considered in simulation while it was ignored in my current study since the base local blood perfusion rate is still unknown for uterine fibroid *in-vivo*. This is an area of ongoing research in our laboratory. This may be further used to improve the TBP model for blood perfusion rate behavior during clinical HIFU surgery.

To summarize, a temperature-dependent model was successfully developed to characterize the heat convection during non invasive HIFU thermal ablation. A fast and large blood perfusion dependent on temperature was necessary to account for the HFIU experimental temperature in both animal *in-vivo* study and woman uterine fibroid *in-vivo*. Though these findings were still not validated in direct measurement of blood perfusion in real time for this technique, these provided the possible direction to optimize the planning of thermal therapy using HIFU procedure to compensate the heat dissipation by the large increase of blood perfusion rate during heating. For example, heating the target tissue to a temperature level that kills the tissue while not introducing a much larger blood perfusion increase is a potential means to improve treatment effectiveness by minimizing energy loss due to convection. Another possible measure may be taken to kill fibroid is that heating the peripheral region of uterine fibroid so as to destroy the micro vasculature. This heating stratagem has not been published yet in uterine fibroid treatment. Another potential application of these findings can also be used in targeted drug deliver. We can intentionally locally heat the target region using HIFU to a certain temperature level to trigger the blood perfusion to increase compared to surrounding health tissue. The blood perfusion increase may result in absorbing drug more efficiently and effectively.

Chapter 6

Tissue Elasticity Characterization by MR-HIFU

6.1 Introduction

Alterations in tissue mechanical properties can be sensitive markers of pathologic changes of tissue as well as reflect physical, structural changes associated with phenomena such as heating[55-57]. Elasticity imaging methods assess the underlying tissue mechanical properties by imparting a well characterized mechanical stimulus (stress) and measuring the resulting tissue deformation (strain). With the knowledge of the stress and strain tissue elasticity can be reconstructed with an appropriate choice of reconstruction algorithms. If the applied stress is non-time varying or static, time-dependent tissue properties like viscosity cannot be estimated. If the stress is dynamic caused by either internal sources (respiration or cardiac pulsations [172-174]) or external (mechanical vibrator through tissue surface [108, 175, 176]), then a more complete estimation of the viscoelastic properties of the tissue may be calculated. Despite the advantage of internal source to introduce stress, it is limited to organs that are close to lung or heart. Furthermore, such internally generated sources of stress are not controllable through amplitude and frequency which is useful in investigating the tissue viscosity.

Externally induced mechanical stress can be applied on the surface of the body and propagated to the tissue of interest and or initialized deep within tissue of interest. A mechanical driver, placed at the body surface, has been used in conventional magnetic resonance elastography (MRE) to introduce a periodic steady state stress and generate elastic shear waves in the tissue[99, 177]. This method has been well established in estimating the tissue shear elasticity in

organs close to the skin surface like liver[62, 100, 103, 178-180]. breast masses[105], prostate cancer[181] , and uterine leiomyomas[182]. However, challenges associated with MRE are as follows: 1) MRE is applicable to organs only close to body surface due to the limited penetration of the shear waves because of their significant attenuation and reflections at tissue interfaces such as between muscle and fat. 2) Estimation of wave velocity *in-vivo* can be difficult and may require sophisticated acquisition and post-processing methods to resolve multitude of contributions from traveling waves, wave reflections, wave refractions, and standing waves.

One potential method to overcome some of the limitations of an externally coupled mechanical device to generate shear waves within the body is the use of ARF to generate shear waves deep within the body. Several groups have proposed using focused ultrasound to remotely generate a localized stress deep in tissue via ARF and measuring the resulting tissue displacement using a diagnostic ultrasound-based method [112, 137, 183, 184]. However diagnostic ultrasound measures only the component of motion that occurs along the axis of the ultrasound beam. However, MRI-based method for measuring tissue displacement is not subject to this constraint due to its capability to encode for motion along any direction. The overall focus of this chapter is to provide details about the practical implementation and experimental verification of the theoretical concepts of tissue elasticity imaging based on magnetic resonance imaging of acoustic radiation force (MR-ARFI).

The organization of this chapter is as follows. A brief description of theory behind tissue elasticity imaging using MR based acoustic radiation force will be introduced in Section 6.2. The validation of this method will be performed with conventional MRE sequence in Section 6.3. The safety regarding temperature rise associated with MR-ARFI acquisitions was discussed in Section 6.4. The tissue visco-elasticity will then be characterized using MR-ARFI method in Section 6.5.

6.2 Theory

6.2.1 Tissue Visco-elasticity

In an isotropic and linearly elastic medium, mechanical wave propagation is governed by following equation[185]:

$$\rho \frac{\partial^2 \boldsymbol{u}}{\partial t^2} = \mu \nabla^2 \boldsymbol{u} + (\lambda + \mu) \nabla (\nabla \cdot \boldsymbol{u}) \tag{6.1}$$

where $\boldsymbol{u}$ is the displacement vector, ρ is the density of the medium, μ and λ are the first and second Lamé parameters. The displacement vector includes motion from longitudinal and shears wave propagation within the tissue. In elasticity imaging the relevant parameter of interest is the shear wave contribution (Chapter 2). In soft tissues, the compressional wave speed is about two orders of magnitude higher than the shear wave speed, and this large difference between the two components can be exploited to separate the two. A commonly used strategy is to take the curl of the displacement vector $\boldsymbol{u}$ ($\nabla \times \boldsymbol{u}$) in order to remove the longitudinal wave contribution, and simplify Eq. (6.1) to:

$$\rho \frac{\partial^2 \boldsymbol{u}}{\partial t^2} = \mu \nabla^2 \boldsymbol{u} \tag{6.2}$$

The temporal Fourier transform of the scalar wave field $u(r, t)$ $U(r, \omega)$ is given by:

$$\rho \omega^2 U + \mu(\omega) \nabla^2 U = 0 \tag{6.3}$$

The above equation can further be simplified to provide a frequency-dependent shear elastic modulus, as:

$$\mu(\omega) = -\frac{\rho\omega^2 U}{\nabla^2 U} \tag{6.4}$$

According to the correspondence principle[186] , the solutions of the linear visco-elastic wave equation can be obtained from the solutions of the linear elastic wave equation in the frequency domain by replacing the tissue elasticity with the corresponding complex modulus $\mu^*(\omega)$.

If a harmonic plane wave propagates within a medium with shear elastic modulus μ, and shear attenuation coefficient α, with a shear wave speed v, and an initial amplitude u_o, at a frequency of ω, then the wave displacement can be written as:

$$u = u_0 \exp[i\omega(\frac{\boldsymbol{n}\cdot\boldsymbol{r}}{v} - t) - \alpha\boldsymbol{n}\cdot\boldsymbol{r})] \tag{6.5}$$

where $\boldsymbol{n}$ is the wave normal vector, and $\boldsymbol{r}$ is the position vector. The wave speed v and attenuation α can be calculated by using Eq. (6.4) and (6.5).

$$v(\omega) = \frac{1}{\mathrm{Re}\left[\sqrt{\frac{\rho}{\mu^*(\omega)}}\right]} \tag{6.6a}$$

and

$$\alpha(\omega) = \omega \mathrm{Im}\left[\sqrt{\frac{\rho}{\mu^*(\omega)}}\right] \tag{6.6b}$$

The complex modulus $\mu^*(\omega)$ can be related to elasticity and viscosity using various rheological models (Fig. 6.1) [187].

Here we consider Voigt, and Zener models to approximate the viscoelastic response of the tissue to a mechanical disturbance[187-191]:

$$G_M(\omega) = \begin{cases} \mu_1 + i\omega\eta, & \text{Voigt} \\ \dfrac{\mu_1\mu_2 + i\omega\eta(\mu_1+\mu_2)}{\mu_2 + i\omega\eta}, & \text{Zener} \end{cases}$$

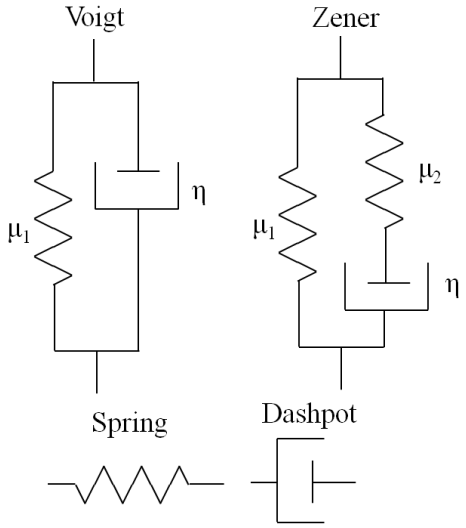

Figure 6.1 Commonly used rheological models to represent tissue visco-elasticity. Voigt model, assumes the tissue to consist of an elastic or spring (μ) term and a viscous or dashpot (η) term in parallel. A slightly more complex model of tissue is the widely used Zener approximation of tissue viscoelasticity with three terms (μ_1,μ_2 and η).

By using the Voigt model: $\mu^* = \mu_1 + \omega\eta\mathrm{i}$, we then have

$$v(\omega) = \sqrt{\frac{2(\mu_1^2 + \omega^2\eta^2)}{\rho(\mu_1 + \sqrt{\mu_1^2 + \omega^2\eta^2})}} \qquad (6.7a)$$

and

$$\alpha(\omega) = \omega\sqrt{\frac{\rho(\sqrt{(\mu_1^2 + \omega^2\eta^2)} - \mu_1)}{2(\mu_1^2 + \omega^2\eta^2)}} \qquad (6.7b)$$

To be noted that, when $\omega = 0$: $v = \sqrt{\frac{\mu_1}{\rho}}, \alpha = 0$, and $\omega \to \infty$: $v \to \infty, \alpha \to \infty$.

By using the Zener model: $\mu^* = \frac{\mu_1\mu_2 + \omega\eta(\mu_1+\mu_2)\mathrm{i}}{\mu_2 + \omega\eta\mathrm{i}}$, we then have

$$v(\omega) = \sqrt{\frac{2[(\mu_1\mu_2)^2 + \omega^2\eta^2(\mu_1+\mu_2)^2]}{\rho\left(\mu_1\mu_2^2 + \omega^2\eta^2(\mu_1+\mu_2) + \sqrt{[\mu_1\mu_2^2 + \omega^2\eta^2(\mu_1+\mu_2)]^2 + \omega^2\eta^2\mu_2^4}\right)}} \quad (6.8a)$$

and

$$\alpha(\omega) = \omega\sqrt{\frac{\rho(\sqrt{[\mu_1\mu_2^2 + \omega^2\eta^2(\mu_1+\mu_2)]^2 + \omega^2\eta^2\mu_2^4} - [\mu_1\mu_2^2 + \omega^2\eta^2(\mu_1+\mu_2)])}{2[(\mu_1\mu_2)^2 + \omega^2\eta^2(\mu_1+\mu_2)^2]}} \quad (6.8b)$$

To be noted that, when $\omega = 0$: $v = \sqrt{\frac{\mu_1}{\rho}}, \alpha = 0$, and $\omega \to \infty$: $v = \sqrt{\frac{\mu_1+\mu_2}{\rho}}, \alpha = \frac{\mu_2^2}{2\eta}\sqrt{\frac{\rho}{(\mu_1+\mu_2)^3}}$.

In the case of the pure elastic material, η is zero and the attenuation α is zero. So, the shear modulus μ_1 can be calculated using either Eq. 6.7a and 6.8a at the condition of $\eta = 0$, as:

$$\mu_1 = \rho v^2 = \rho(\frac{\omega}{k})^2 = \rho(\frac{2\pi f}{2\pi/\lambda})^2 = \rho(\lambda f)^2 \quad (6.9)$$

where *f* is the mechanical driving frequency, *k* is the wave number and λ is the specific wavelength at *f*.

The above expression cannot be directly used to assess the shear elastic modulus of soft tissues which are visco-elastic in nature. However, many clinically used MRE methods report a shear elastic modulus estimated using Equation 6.9. For example, some MRE processing techniques using local frequency estimation (LFE) or phase gradient algorithms, calculate only the local wavelength of a propagating shear wave, and use Equation 6.9 to report a shear elastic modulus (μ)[107], without taking tissue attenuation into account. These techniques essentially estimate the wave speed, and can be thought of reporting an 'effective' shear modulus or 'shear stiffness' at that frequency. Some other techniques calculate both elasticity and viscosity by directly inverting the displacement wave field. However, such inversion techniques involve

multiple derivative operations that are very sensitive to noise. A possible way to determine the visco-elastic parameters is to calculate the shear velocity at several different frequencies and fit the result to Eq.6.7a or 6.8a based on different rheological models. The attenuation can then be calculated from Eq. 6.7b or 6.8b. The disadvantage of this approach is the time penalty associated with repeated measurements at multiple frequencies.

Though the derivation for the estimation of tissue visco-elasticity is based on the assumptions of a propagating harmonic plane wave, this estimation still holds for the transient motion by decomposing the transient wave into a set of harmonic plane wave of various frequencies. This can be implemented through Fourier-based analysis of the transient wave propagation in temporal domain.

6.2.2 Spectral Analysis of Transient Motion by MRI

Motion encoding gradient waveforms can be designed with spectral selectivity to a particular harmonic frequency as discussed in Chapter 2. In MR-ARFI, a shear wave emanates from the HIFU focus consisting of a broad range of frequencies within tissue. In this section, we consider the theoretical basis for encoding such transient motion.

Consider a MEG, $G_r(t)$ truncated in time by an apodizing function $w(t)$, used to encode tissue displacement $r(t)$. The additional phase shift in the received MR signal due to the spin motion in the presence of the MEG, Eq. (2.29) can be written as:

$$\phi(\tau) = \int_0^\tau \gamma[G_r(t) \cdot w(t)] \cdot r(t) dt \tag{6.10}$$

Where,

$$w(t) = \begin{cases} 1, & 0 < t < \tau \\ 0, & otherwise \end{cases} \tag{6.11}$$

if $G_r(f)$ is the Fourier transformation (FT) of $G_r(t)$, then Eq. (6.10) can be rewritten as,

$$\phi(\tau) = \gamma \int_0^{\tau} \left[\int_{-\infty}^{\infty} G_r(f) \exp(-j2\pi ft)\, df \cdot w(t) \right] \cdot r(t) dt$$

$$= \gamma \int_{-\infty}^{\infty} G_r(f) \cdot \left[\int_0^{\tau} w(t) \cdot r(t) \exp(-j2\pi ft)\, dt \right] df \tag{6.12}$$

Eq. 6.12 can be further simplified as,

$$\phi(\tau) = \gamma \int_{-\infty}^{\infty} G_r(f) \cdot [w(-f) \otimes r(-f)] df \tag{6.13}$$

where $w(f)$ and $r(f)$ are the FT of $w(t)$ and $r(t)$ respectively and $\otimes$is the convolution operator. In other words, the spectral response of the MEG, $G_r(f)$, acts as a frequency domain filter that can extract spectral components of motion. For a pure harmonic mechanical excitation, the gradient waveform extracts spin motion at that specific frequency – the case of steady state harmonic excitation discussed previously. In the case of transient excitation, the spectral component of displacement consists of a broad band of frequencies. Therefore, to encode such a broad band mechanical excitation, $G_r(f)$ must also have broad-band spectral selectivity.

If the material is dispersive, the shear stiffness varies with frequency and the calculated stiffness based on the wave speed estimation will yield a single shear stiffness value that is a weighted average of the stiffness values at different frequencies. To reiterate, Eq. 6.13 represents a Fourier based generalization of the gradient function. Viewed in this perspective, MEG could be considered as a 'filter' that selectively measures components of motion. For example, specific harmonic component of motion can be extracted by choosing the gradient waveform at the frequency of interest.

6.2.3 Simulation of Cyclic and Transient MRE

As shown in Eq. 6.13, the MEG served as a 'filter' for MRI encoding the mechanical motion at frequency of interest. The can be explained in two ways: 1) a MEG waveform containing a single frequency can be used to extract motion component of same frequency of MEG from a multi-frequency mechanical excitation; 2) A MEG waveform containing a broad band frequency component can be used to encode a pulse excitation which contains a broad band spectrum. By employing a frequency domain analysis method, it's feasible to extract specific frequency component from the measured complex wave information. This principle was used to estimate the tissue viscoelasticity from MR-ARFI measurement in this chapter.

The spectral sensitivity of a single cycle of a trapezoidal MEG at 250Hz is shown in Fig. 6.2.

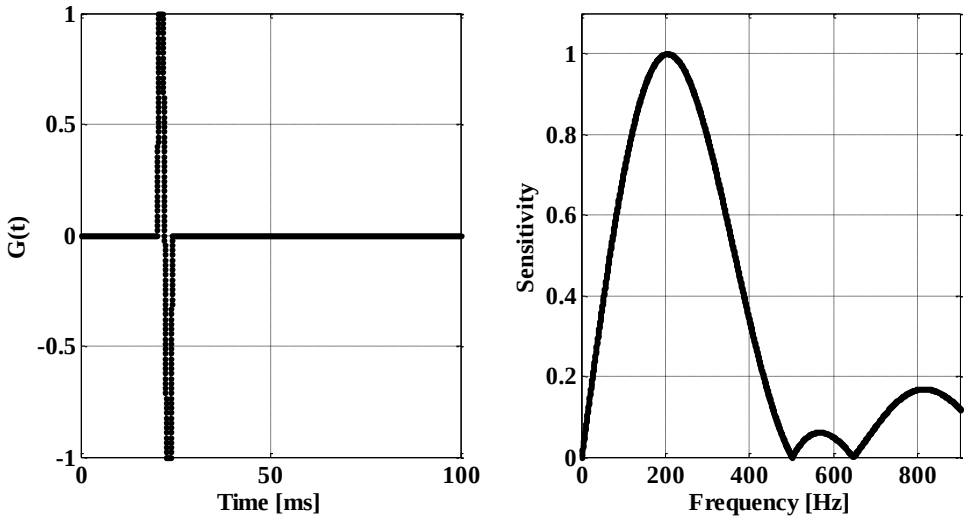

Figure 6.2 Single cycle (250 Hz) of motion encoding gradient waveform G(*t*) (left) and the corresponding sensitivity function (right).

The MEG waveform has broad motional sensitivity from 40~440Hz. Note that the peak sensitivity of this gradient waveform is close to 250 Hz (at 220 Hz), and the sensitivity to motion at other frequencies falls rapidly about the central frequency. This approach is flexible in that if

motion sensitivity at a specific frequency spectrum is desired, then a corresponding MEG waveform could be designed by inverting the process, within the slew rate and amplitude performance constraints of the gradient sub-system.

MRI encoding of cyclic motion

To investigate the effect of MEG waveform on the measured MRI phase for encoding cyclic motion, we use Eq. 6.10 to simulate the MRI encoding process. In order to mimic experimental conditions, a trapezoidal MEG at a frequency of 250 Hz, was used to encode cyclic motion occurring at three different frequencies (160 Hz, 300 Hz, and 380 Hz) is shown in Figures 6.2 – 6.4.

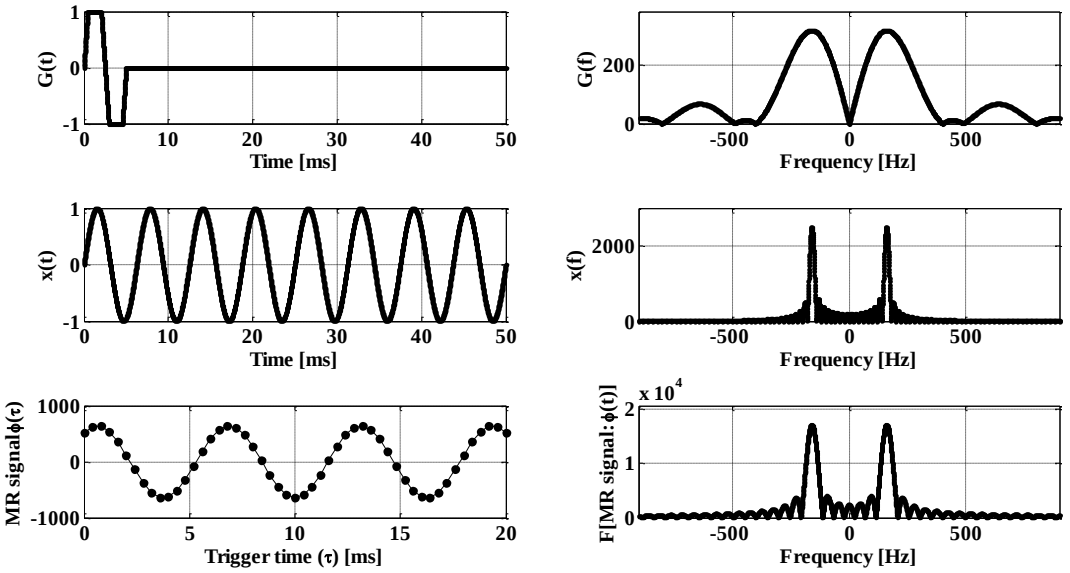

Figure 6.3 Single cycle (250 Hz) of MEG waveform G(*t*) (left) and its frequency spectrum (right) are shown in the top row. This MEG waveform was used to encode cyclic motion at 160 Hz (middle panel). . Numerically simulated results are shown in the bottom row. As the phase relationship between the MEG and the motion waveform is varied, the measured phase shift also follows a sinusoidal pattern at 160 Hz (bottom left), and the corresponding frequency domain spectrum of the measured phase shift has a peak frequency response at 160 Hz (bottom right).

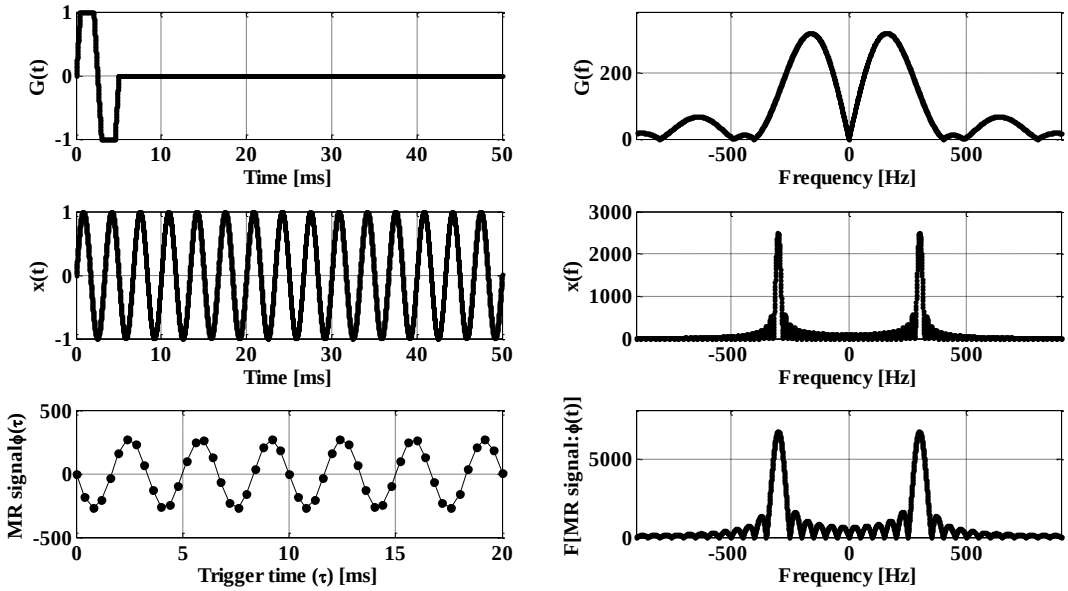

Figure 6.4 Single cycle (250 Hz) of MEG waveform G(*t*) (left) and its frequency spectrum (right) are shown in the top row. This MEG waveform was used to encode cyclic motion at 300 Hz (middle panel). . Numerically simulated results are shown in the bottom row. As the phase relationship between the MEG and the motion waveform is varied, the measured phase shift also follows a sinusoidal pattern at 300 Hz (bottom left), and the corresponding frequency domain spectrum of the measured phase shift has a peak frequency response at 160 Hz (bottom right).

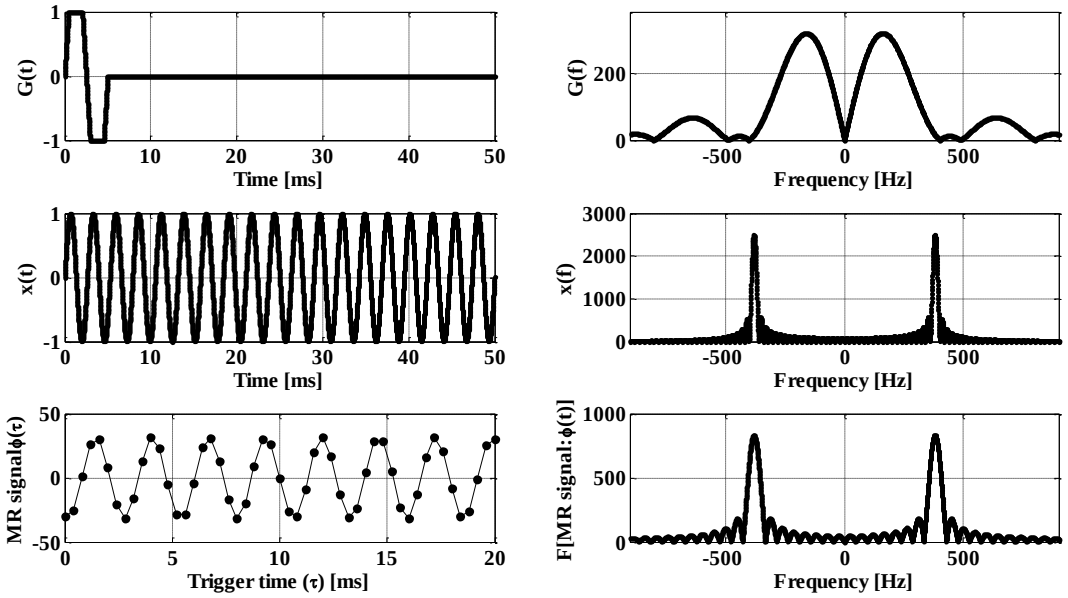

Figure 6.5 Single cycle (250 Hz) of MEG waveform G(*t*) (left) and its frequency spectrum (right) are shown in the top row. This MEG waveform was used to encode cyclic motion at 380 Hz (middle panel). . Numerically simulated results are shown in the bottom row. As the phase relationship between the MEG and the motion waveform is varied, the measured phase shift also follows a sinusoidal pattern at 380 Hz (bottom left), and the corresponding frequency domain spectrum of the measured phase shift has a peak frequency response at 160 Hz (bottom right).

MRI encoding of transient motion

MR encoding of transient motion was modeled as follows. Transient motion emanating at the HIFU focus was modeled as an impulse force applied for a duration of 1 ms, which subsequently decays exponentially (with a decay constant of 0.5) (Fig. 6.6). A single cycle of bipolar trapezoidal MEG at a frequency of 250 Hz was used to encode this transient motion.

It can be seen that the spectrum of the impulse excitation showed a broad band motion components. However, the motion above 500Hz was filtered out by the limited band frequency response of MEG from the measured resultant phase. While the spectral components of motion within the 500 Hz were encoded by the MEG, the sensitivity with which various frequencies within that range were encoded was different.

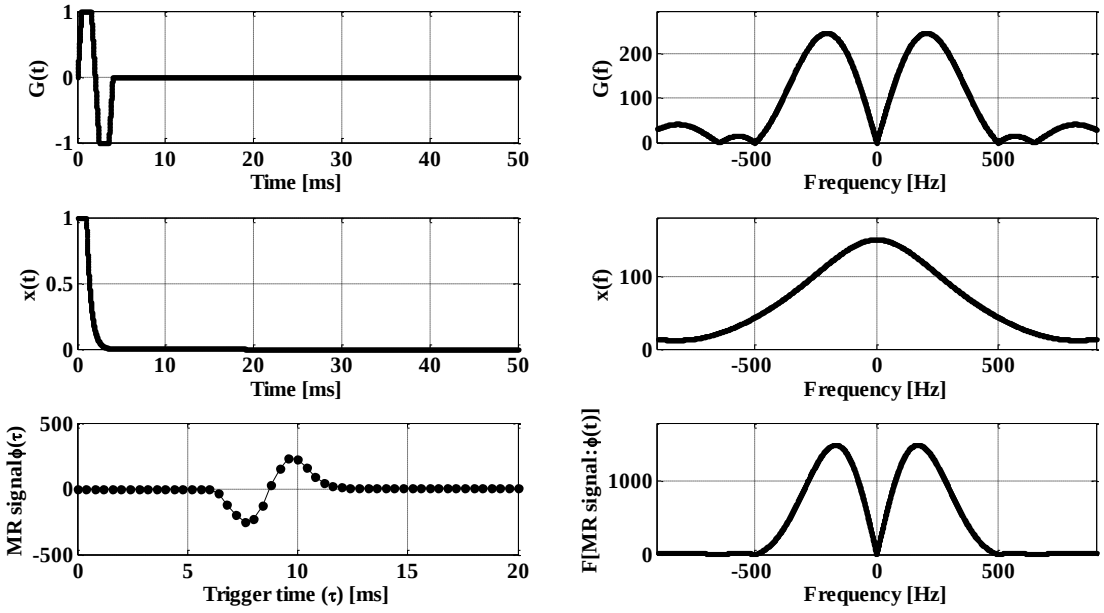

Figure 6.6 Single cycle (250 Hz) of motion encoding gradient waveform G(*t*) (top left) and the corresponding spectrum (top right). The simulated ARFI motion of square (1ms) following by an exponential decay ($1e^{-2t}$) (middle left) and the corresponding spectrum (middle right). The simulated measured MR signal and spectrum encoding the motion with G(*t*) is shown in bottom left and bottom right.

To study the effect of MEG of different frequency on encoding the same transient motion, Two MEG waveform of one cycle of frequency at 250Hz and 100Hz were used to encode the same transient motion of duration 5ms following by a exponential decay as shown in Fig. 6.7 and 6.8 respectively. The resultant MR measured signal using 250Hz MEG showed a broader band motion component compared to the 100Hz MEG due to its broader band response although the absolute signal almost decrease half. This give us two options to analyze the : 1) If only effective modulus is of interest, 100Hz MEG can be chose to maximize the signal intensity; 2) If mechanical property at broad frequencies are of interest, a 250Hz MEG can be used as long as the lower signal intensity is acceptable to reconstruct the mechanical properties.

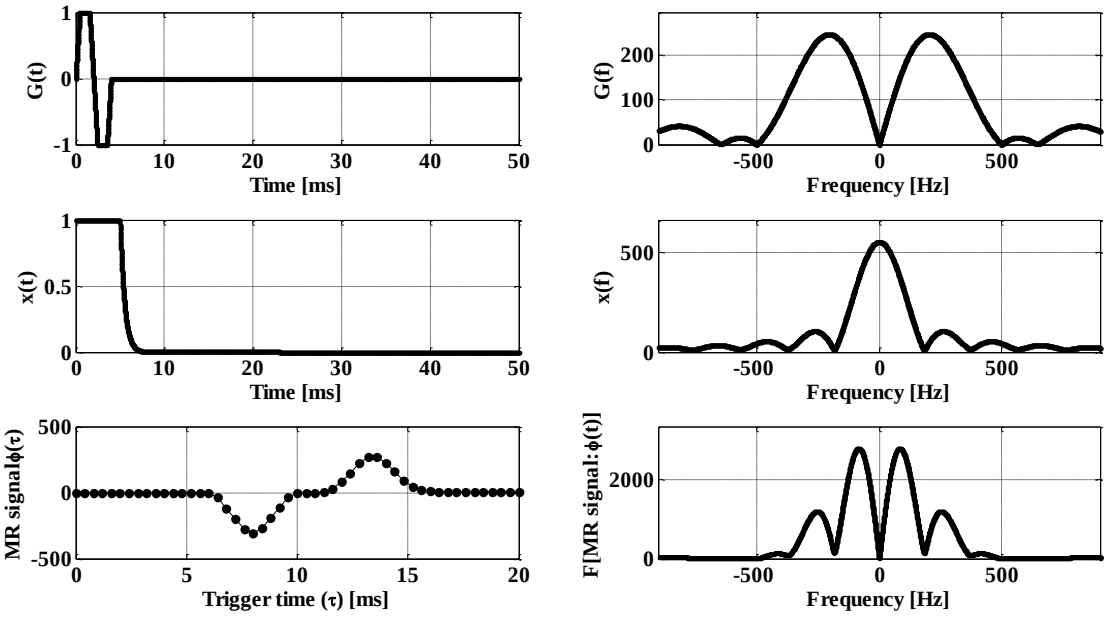

Figure 6.7 Single cycle (250 Hz) of motion encoding gradient waveform G(*t*) (top left) and the corresponding spectrum (top right). The simulated ARFI motion of square (5ms) following by exponential decay ($1e^{-2t}$) (middle left) and the corresponding spectrum (middle right). The simulated measured MR signal and its spectrum is shown in bottom left and bottom right respectively.

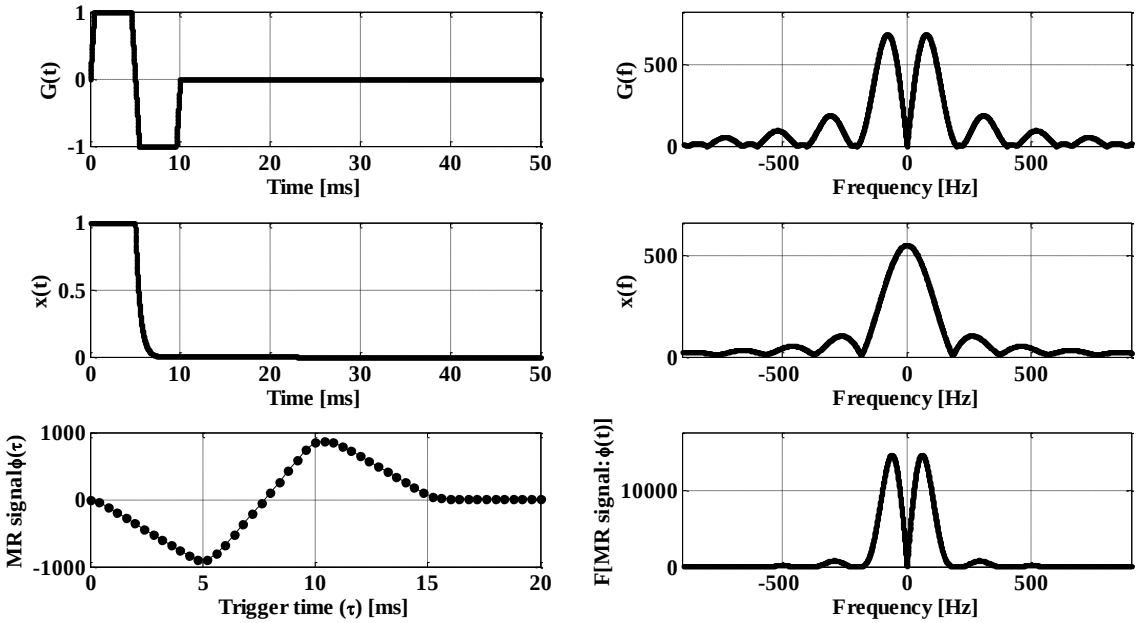

Figure 6.8 Single cycle (100 Hz) of motion encoding gradient waveform G(*t*) (top left) and the corresponding spectrum (top right). The simulated ARFI motion of square (5ms) following by exponential decay ($1e^{-2t}$) (middle left) and the corresponding spectrum (middle right). The simulated measured MR signal and spectrum encoding the motion with G(*t*) is shown in bottom left and bottom right.

In this chapter, a 250 Hz MEG was chose to estimate the mechanical properties at a broad band frequency which is used to quantitatively calculate the tissue visco-elasticity. This can be realized by performing temporally Fourier transform on MR acquired transient shear wave images and then decompose into the specific frequency component.

6.3 Validation MR-ARFI by Conventional MRE

6.3.1 Generation of Transverse Mechanical Waves within the Magnet

The following two devices were used to generate the cyclic motion and transient motion in the magnet: computer controlled voice-coil based driver (conventionally used in clinical MRE study) and piezo-electric transducer. In conventional clinical MRE, the computer controlled voice-coil based driver (from Mayo clinic, MN, US) which consists of an active acoustic driver

that located outside the MR magnet was coupled by means of plastic tubing to a disc-shaped non-metallic passive driver which is placed on top of liver (Fig. 6.9 left) to couple mechanical vibration at specific frequencies to probe internal organs such as the liver (Fig. 6.9 middle) [192]. This acoustic active-passive driver is able to generate well-controllable cyclic motion (20 -200 Hz) within the magnet and will be used to measure the elasticity of the phantom by placing the passive drive at bottom of the phantom (Fig. 6.9 right) and then to validate the result from the method we developed based on therapeutic HIFU system. In our method based on piezo-electric transducers (Fig. 6.10 left), a short burst (programmed to be 2~6ms) can be emitted from transducer to initialize a transient shear wave in the focal region (Fig. 6.10 right). We used a 256-element transducer (a 256 channel spherical shell HIFU transducer with five degrees of freedom to non invasively initialize shear wave at any position of the tissue where HIFU beam can reach by either electronically or mechanically moving the transducer. This potentially provides the opportunity to probe the tissue mechanical properties at a large and deep region in the body.

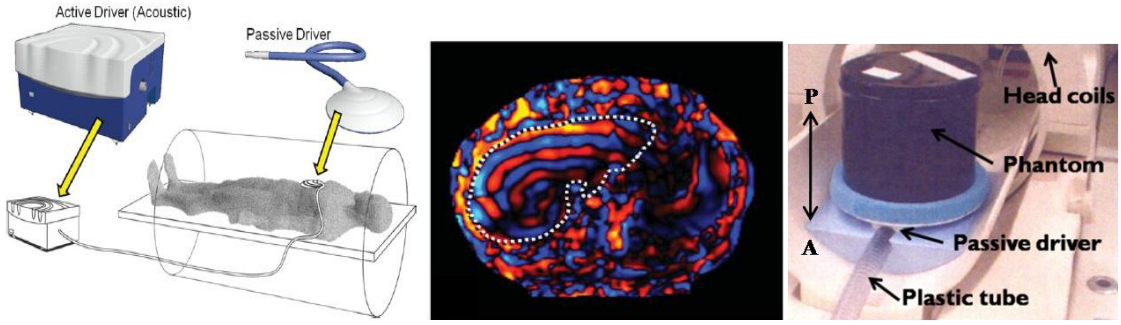

Figure 6.9 Schematic showing clinical MRE pneumatic passive driver placed on the liver of patient (left). Sound waves are transmitted through a hollow tube to the passive driver and into patient's liver (middle)[192]. Dotted line shows the liver region. The right figure shows setup of phantom MRE.

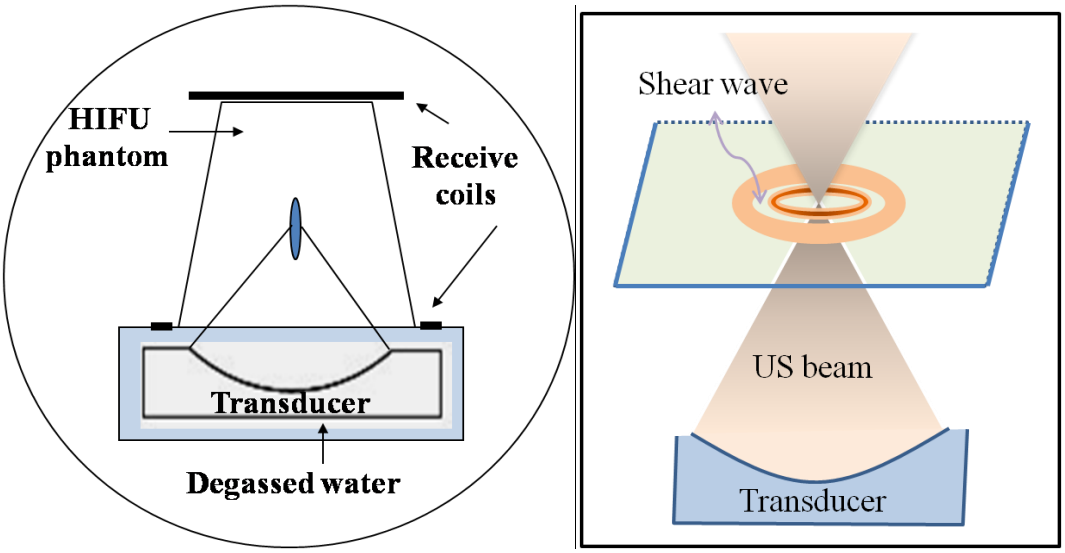

Figure 6.10 Schematic showing the experimental setup for introducing transient shear wave by MR-ARFI (left). The shear wave is initialized inside the phantom and travel outward (right).

6.3.2 Pulse Sequence and Control

Steady state motion or transient motion can introduce a measurable phase shift in the received MR signal using MEG. However, it is difficult to extract the motion information from the absolute phase of the MR signal from a single measurement since the phase of the received MR signal is also affected by other factors such as $\boldsymbol{B_0}$ inhomogeneity, RF imperfections, concomitant field, bulk motion and eddy currents caused by gradient transitions, pulse sequence timing, etc. It is therefore necessary to obtain more than one measurement to compute the relative phase shifts. In the clinical MRE study, the gradient echo sequence with provisions for superimposing cyclic gradient waveforms have been developed in the use of clinical application[192] as show in Fig.6.11.

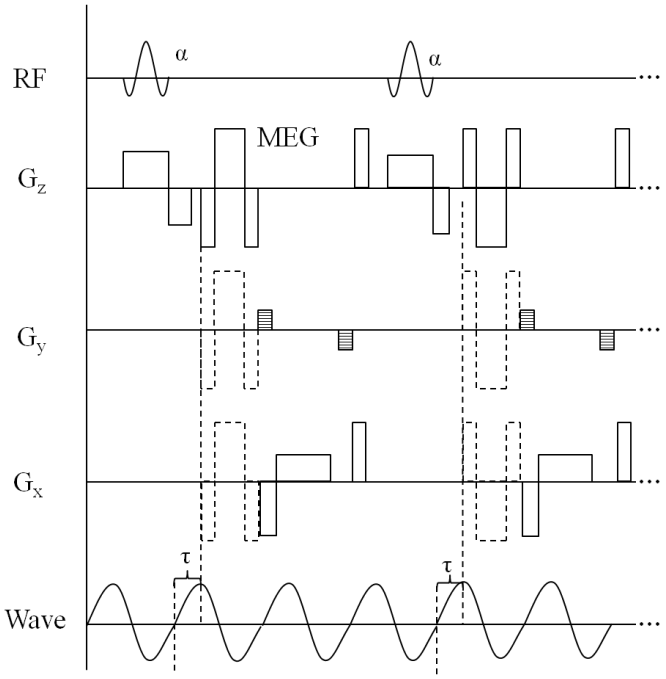

Figure 6.11 A diagram of a 2D gradient echo-based MRE of cyclic motion sequence. Sensitivity to cyclic tissue motion caused by shear wave was achieved by adding the motion encoding gradients (MEG) that were synchronized with the applied vibration throughout image acquisition. The MEG can be applied in any x-, y- or z-direction to encode the corresponding motion component. The phase offset (τ) between the MEG and the applied mechanical waves can be adjusted in steps to acquire wave images at different time.

The initial RF excitation creates the transverse magnetization. The MEGs encode the cyclic spin motion in the phase of the MR signal, at the echo time T_E. The waveform of MEG can be trapezoidal, sinusoidal or sinc function and can be superimposed along any axis to encode the different motion component. An adjustable number of trigger pulses can be applied prior to the initial RF excitation to establish a mechanical steady state. The trigger pulses (TTL signal) triggered a waveform generator coupled to a patient. The resulting motion of the actuator launches a transverse mechanical wave on body surface and propagates into the organ of interest. The phase shifts caused by the cyclic motion of the spins in the presence of the MEG provide snapshots of the mechanical waves traveling within the tissue. For each phase offset, two data phase images were acquired with opposite polarity of MEG, the wave image is reconstructed from the subtraction of the two data sets. By doing this subtraction, the sensitivity to micro level

displacement is doubled[193] and the systematic phase error due to B_0 field inhomogeneities etc. got suppressed.

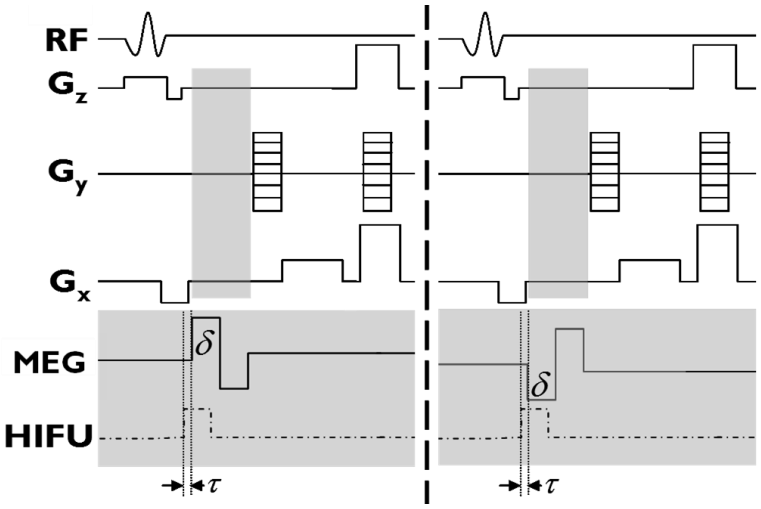

Figure 6.12A diagram of a 2D gradient echo-based MR-ARFI sequence. Sensitivity to transient tissue motion caused by shear wave was achieved by adding the MEGs that were synchronized with the applied impulse HIFU energy. The MEGs can be applied in any x-, y- or z-direction to encode the specific motion vector component. The phase offset (τ) between the MEG and the applied HIFU can be adjusted to acquire temporal propagation of transient shear wave.

Compared to the pulse sequence diagram of clinical MRE using cyclic continuous motion, the difference was that the mechanical motion was initialized by an impulse excitation from HIFU in MR-ARFI pulse sequence diagram (Fig. 6.12). The time delay (τ) between the application of the HIFU energy and the MEG was altered to capture the propagation of the displacement wave.

6.3.3 Data Acquisition and Processing

6.3.3.1 MR-ARFI Acquisition

The pulse sequence (Fig. 6.12) provided control over the duration, amplitude, timing, and the direction of the MEG to encode the spin motion. Specific acquisition parameters were: matrix size: 256 x 64; field of view: 200 mm x 200 mm; slice thickness: 5mm; repetition time/echo

time/flip angle ($TR/T_E/FA$) = 65ms/13~17 ms/30°; bandwidth: 170 Hz/pixel; scan time: 8.3s per phase offset. The duration of the symmetric bipolar MEG vary from 4.0ms to 11.1ms, and the amplitude of MEG strength was set to 27mT/m to give the maximum sensitivity to micro level displacement of spin motion. The encoding gradient slew rate was fixed at 100T/m/s through all the MR-ARFI experiments. The timing and strength of MEG was fixed during one acquisition. A coronal slice (perpendicular to HIFU beam) bisecting the plane of the focus was used as image plane and the motion encoding direction was set parallel to HIFU beam direction. A TTL signal will be generated in MR scanner in each repetition time and sent to HFIU generator to create an impulse motion of desired duration (frequency of HIFU was triggered at 1.2MHz) in target region (Table 6.1).

Table 6.1 MEG frequency synchronization with HIFU

MEG frequency (Hz)	HIFU duration [ms]	# of HIFU cycles at 1.2MHz
90	5.6	6,667
100	5.0	6,000
120	4.2	5,000
150	3.3	4,000
180	2.8	3,333
200	2.5	3,000
250	2.0	2,400

A total of 48 temporal phase offsets were acquired to visualize transient wave propagation within a tissue mimicking gel phantom (cylinder, diameter of 180mm).

6.3.3.2 MRE Acquisition of Cyclic Motion

The MRE sequence for encoding cyclic motion was the same as the clinically used sequence (Fig. 6.11). The pulse sequence provided control over the duration, amplitude, timing, and the direction of MEGs. Specific acquisition parameters for the conventional MRE sequence were: acquired matrix size: 172 x 171; field of view: 256 mm x 210 mm; slice thickness: 5mm;

repetition time/echo time/flip angle (TR/TE/FA) = 20~100ms/13~17 ms/30° (TR is an integral multiple of period of cyclic motion, Table 5.2); bandwidth: 110 Hz/pixel; scan time: 6s~30s per phase offset. The duration of symmetric flow compensated 1-2-1 motion encoding gradient varied from 5.0 ms to 11.1 ms, and the MEG strength was set to 21 mT/m. A coronal slice placed in the middle of phantom was imaged and the MEG was set perpendicular to the slice-select direction. A TTL signal was generated in MR scanner in each repetition time and was sent to activate the external mechanical driver to generate motion of desired frequency and amplitude. The duration of MEG was synchronized to the frequency of cyclic motion. In order to achieve steady state for cyclic motion, 10 cycles of motion was applied prior the data acquisition for each phase offset between motion and MEG. Total 12 phase offsets were acquired for imaging the cyclic motion wave propagation at temporal interval of one twelfth of motion period in the same tissue mimicking gel phantom used in MR-ARFI.

Table 6.2 Synchronization of motion with MRI acquisition

Motion frequency (Hz)	TR(ms)	# cycles of motion per TR
90	100	9
100	50	5
120	50	6
150	20	3
200	20	4

6.3.3.3 MR-ARFI Elasticity Reconstruction

To extract the shear wave propagation from the two data sets of phase images with opposite polarity of MEG were acquired. A phase difference (wave) image was generated from these two acquisitions. Since these phase images reflect the displacement of spins in the medium, the phase difference images were also referred to as the ‘shear wave’ images. Experimental

results illustrating shear wave propagation excited by ARF from HIFU in homogeneous phantom media is provided as in Fig. 6.13. It clearly shows the propagation of the shear wave in the phantom. Both positive and negative peak phase shift can be clearly distinguished due to the high achieved SNR in phase images. The amplitude of the shear wave clearly decreases as the wave travels outward.

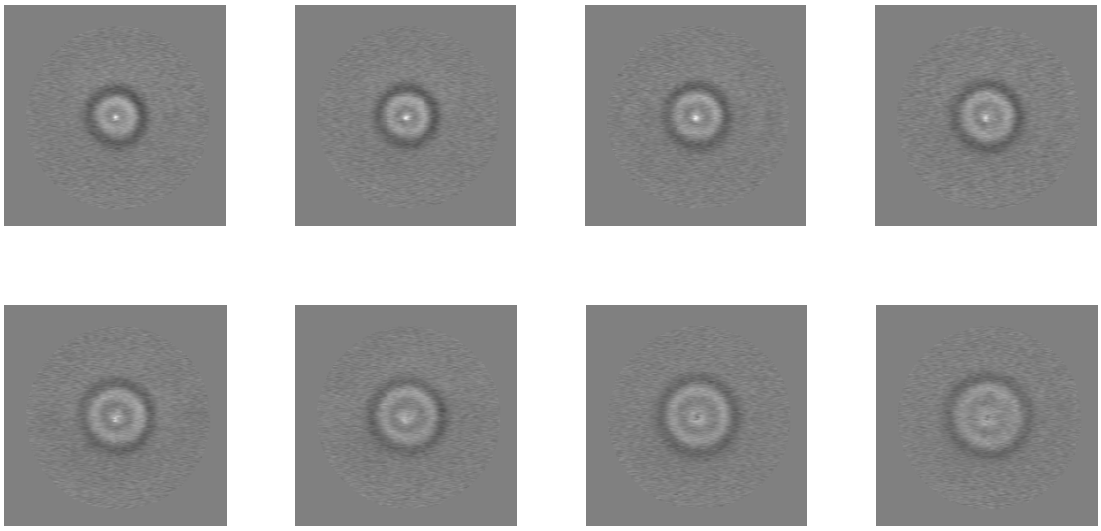

Figure 6.13 Typical series of eight consecutive shear wave images (located at the center of HIFU focus and perpendicular to the ultrasound beam) encoded with one pair of bipolar gradient at frequency 250Hz, HIFU impulse duration is 2ms, P_{max} = 250W(acoustic power). Each image is of 20×20 cm^2.The images were separated by a time interval (or phase offset) $\Delta\tau$ = 0.4ms. Gray scale is $-\pi/2$ to $\pi/2$ from back to white.

In the homogeneous medium, the expected shear wave initialized at center of the phantom by ARF in the plane perpendicular to the HIFU beam are concentric circles of different diameters at different time delay. The following steps were employed to reconstruct the medium elasticity: 1) phase difference images were created by subtraction the two phase images with opposite polarity of MEG at same time delay; 2) Two sequential Radon transforms (RT) [194, 195] were performed on each phase difference image to identify the diameter of circle of the negative peak using user customized matlab function (Mathworks, MA), which corresponds to wave front at that time delay (Fig. 6.14); 3) the distance of shear wave front traveled at different time points

were fitted to a linear function and the slope yields the shear wave velocity (Fig 6.15); 4) shear elasticity is then estimated based on Eq. 6.9 with known density of phantom material ($1.02 g/cm^3$ in this phantom).

This post-process reconstruction of medium elasticity would be applied to experiments in the following section using ARF excited wave propagation to reconstruct the mechanical properties. It should be noted that, as implemented currently, the RT based algorithm can only be used for evaluating transient wave propagation in homogeneous medium.

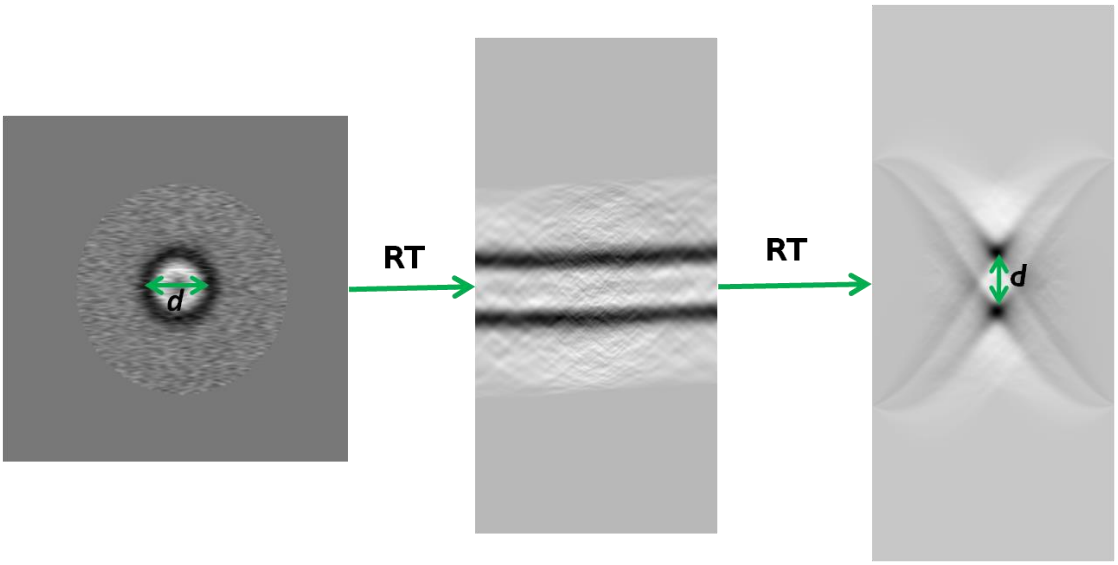

Figure 6.14 Phase difference image from subtraction of two phase images acquired with opposite polarity of MEG at same time delay between excitation and MEG (left). A RT was performed on the phase difference image to convert the circle pattern to two straight lines (middle). The 2nd RT was performed to convert the two straight lines to two points in one image (right). The distance between these two negative points corresponds to the diameter of the negative peak circle on left image.

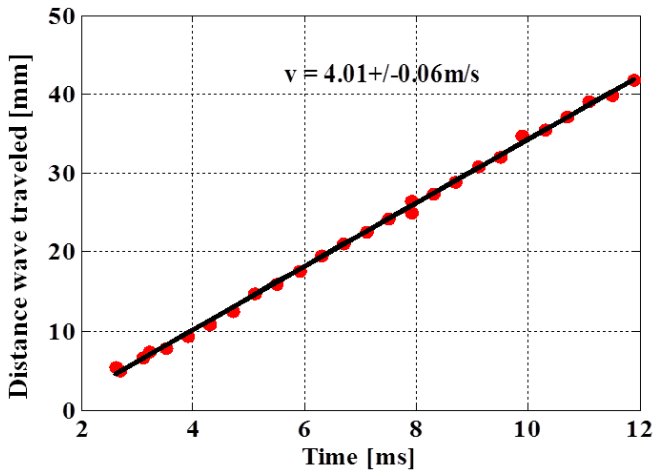

Figure 6.15 The estimated shear wave velocity with MEG frequency of 250Hz while the duration of HIFU pulse was 2ms and thus the estimated shear elasticity $\mu = \rho v^2 = 16.4 \pm 0.5$kPa.

6.3.3.4 MRE Elasticity Reconstruction

As for conventional MRE, the cyclic motion was initialized on the surface of the medium and then the wave traveled into the medium. From Eq. 6.9, the medium elasticity can be calculated by estimating the wave length at specific frequency of cyclic motion. Similar to MR-ARFI elasticity imaging, the shear wave image was referred to the phase difference from the two phase images acquired at same phase offset (time delay) with opposite polarity of MEG.

In the homogeneous medium, the steady-state shear wave propagation pattern introduced by cyclic motion in the homogeneous phantom (cylinder) was expected to be multiple concentric circles (successive peak-to-peak distance is considered as one wave length). Typical shear wave propagation at different time delay in this phantom is shown in Fig. 6.16.

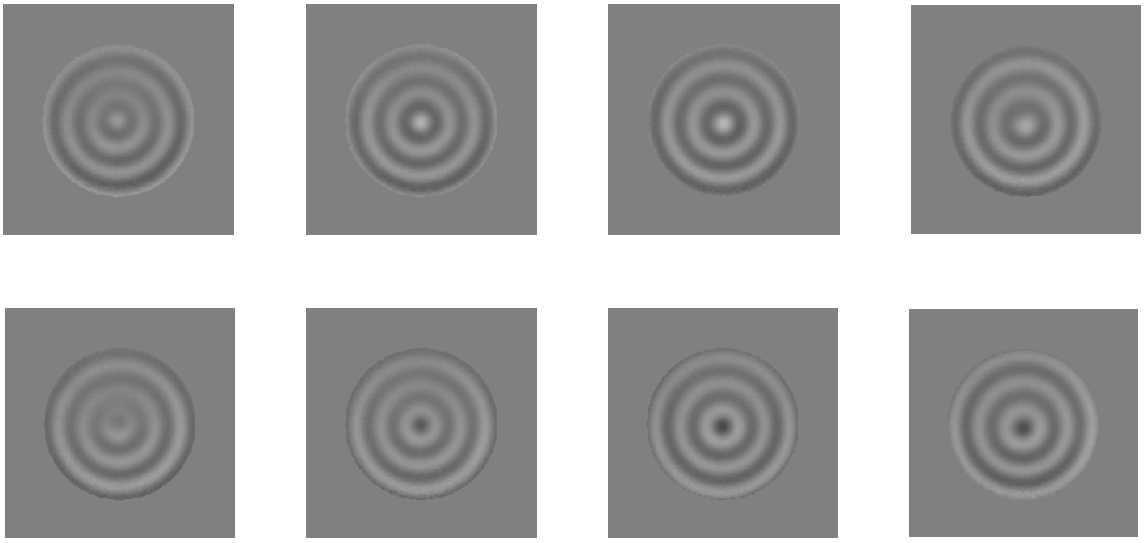

Figure 6.16 Typical series of eight consecutive shear wave images capturing the steady-state motion caused by an external actuator are shown above. Each of the eight images was acquired at progressively increasing delays between the onset of the MEG and the external vibration (both at 120 Hz). Gray scale is $-\pi/2$ to $\pi/2$ from back to white.

To extract the elasticity information in this homogeneous phantom which is essentially to estimate the wave speed, the only step needed is to track the distance traveled by one of chosen wave phase (negative or positive peak, or transition zone between negative and positive peaks) in the wave images. That is implemented by manually drawing one circle of different diameter at chosen phase on each time delay (phase offset) image (Fig. 6.17).

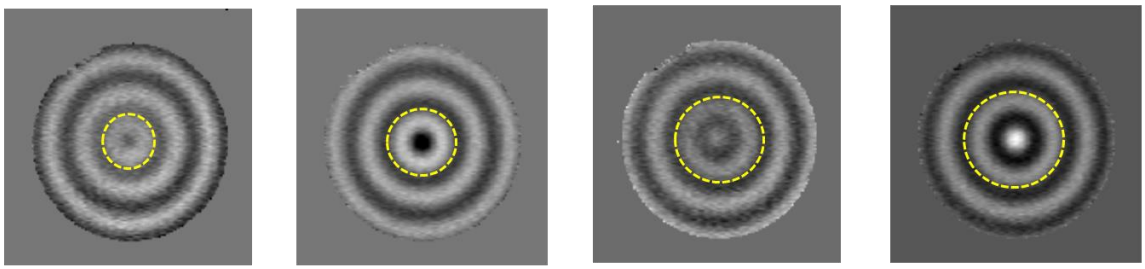

Figure 6.17 A manual approach for estimating shear wave speed in steady state MRE. Circles circumscribing the onset of negative peak at each of the four temporal delays were drawn. Wave speed in this homogeneous medium can be readily computed as the ratio of the distance travelled by the wave(Δr – or change in the radius), over the duration between the offsets ($\Delta t = 1/4T_{vibration}$). .

The radius of the drawn circles shows how far the shear wave traveled at each time points. The wave speed at this frequency was estimated as the slope by fitting the traveled distance of shear wave at different time points to a linear function of time. Fig.6.18 shows the result estimated wave speed at vibration of frequency of 200Hz.

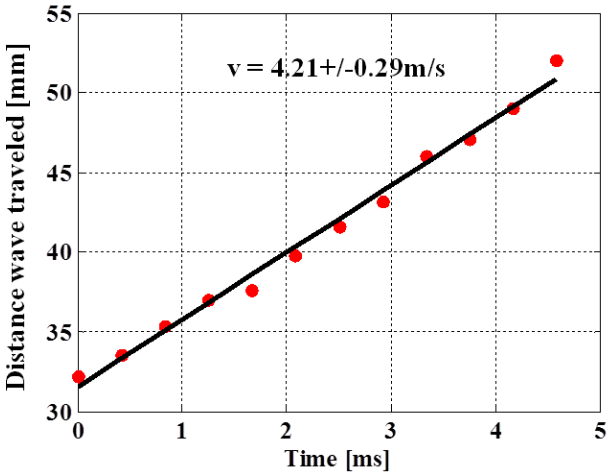

Figure 6.18 The estimated shear wave velocity with MEG frequency of 200Hz synchronized with the cyclic motion of 200Hz and thus the estimated shear elasticity $\mu = \rho v^2$=18.1 ±2.6kPa.

While this approach is suitable for estimating shear wave speed in homogeneous media, more complex algorithms are necessary to estimate local wave speed in heterogeneous media. As for *in-vivo* study or inhomogeneous medium, other algorithms such as time direct inversion algorithm (TDI), local frequency estimation (LFE), and phase gradient method[107] have been proposed in the literature. The details of these algorithms are out of scope of this dissertation.

In summary, the estimated elasticity of phantom using new MR-ARFI elastography method (16.4 ±0.5kPa) agreed with conventional steady state MRE (18.1 ±2.6 kPa at vibration frequency of 200 Hz). The slight different elasticity between these two methods was possible because of that the wave speed estimated with MR-ARFI elastography is the *group* velocity over the wide frequency range of 20~200 Hz motion which will lower the estimated speed compared

to the wave speed estimated from the MRE with a single frequency excitation which only include a single frequency of 200Hz motion. More details can be found in section 6.5.

6.4 Safety: Temperature Rise during MR-ARFI Acquisition

Mechanical properties estimation based on the MR-ARFI relies on ARF from HIFU pulse to create a disturbance and initialize the shear wave in focal region[133]. In order for this new technique to be clinically used, special attention needs to be paid to the thermal effects of the HIFU since high acoustic power is used to initialize the shear wave in deep tissue and multiple time delay (phase offset) are necessary to capture the shear wave propagation. This may result in significant local heating at the HIFU focus. Thus it is necessary to simultaneously monitor the temperature change and wave propagation so as to make sure the temperature rise is still in the safety range.

6.4.1 Principles of Simultaneous Measurement of Displacement and Temperature

For wave images at each time point, two phase images are acquired with opposite polarity of MEG, the phase of positive and negative polarity are denoted as ϕ_+ and ϕ_- respectively.

$$\phi_+(n) = \Delta\phi_T(n) + \Delta\phi_M(n) + \phi_0 \qquad (6.14a)$$

$$\phi_-(n) = \Delta\phi_T(n) - \Delta\phi_M(n) + \phi_0 \qquad (6.14b)$$

where $\Delta\phi_T$, and $\Delta\phi_M$ are the phase change due to the temperature and motion while $\phi_0$is the systematic background phase[196]. The phase change due to the motion and temperature can be solved using Eq. 6.14a and 6.14b.

$$\Delta\phi_M(n) = \frac{\phi_+(n) - \phi_-(n)}{2} \tag{6.15}$$

$$\Delta\phi_T(n) = \frac{\phi_+(n) + \phi_-(n)}{2} - \phi_0 \tag{6.16}$$

The phase change due to motion in Eq. 6.15 purely relies on the subtraction of the two phase images. While the phase change due to temperature change relies on both the addition of the two phase images and the systematic background phase which does not change with time. Thus it is possible to get the dynamic temperature information during the MR-ARFI acquisitions. The temperature can be calculated based on proton resonance frequency (PRF) method [197, 198].

$$T(n) = T(n-1) + \frac{\Delta\phi_T(n) - \Delta\phi_T(n-1)}{\gamma\alpha B_0 T_E} \tag{6.17}$$

where γ is the gyromagnetic ratio, α = -0.01 ppm/^{o}C is the PRF change coefficient for aqueous tissue, B_0 is the main magnetic field, T_E is the echo time. Thermal dose accumulation during MR-ARFI was also calculated using the Sapareto-Deway equation (Eq. 3.2)[13].

The thermal dose thresholds of 30 EM and 240 EM were used to characterize the tissue damage during MR-ARFI acquisition.

6.4.2 Resultant Temperature Change from MR-ARFI Acquisition

Figure 6.19 shows one example of simultaneously visualizing mechanical shear wave propagation and temperature change. The left two images acquired at the fifth and twentieth time delays showed the shear wave initialized in the center of phantom propagating outwards. As repeating HIFU energy applied to generate shear wave, obvious temperature rise was caused at the focal region.

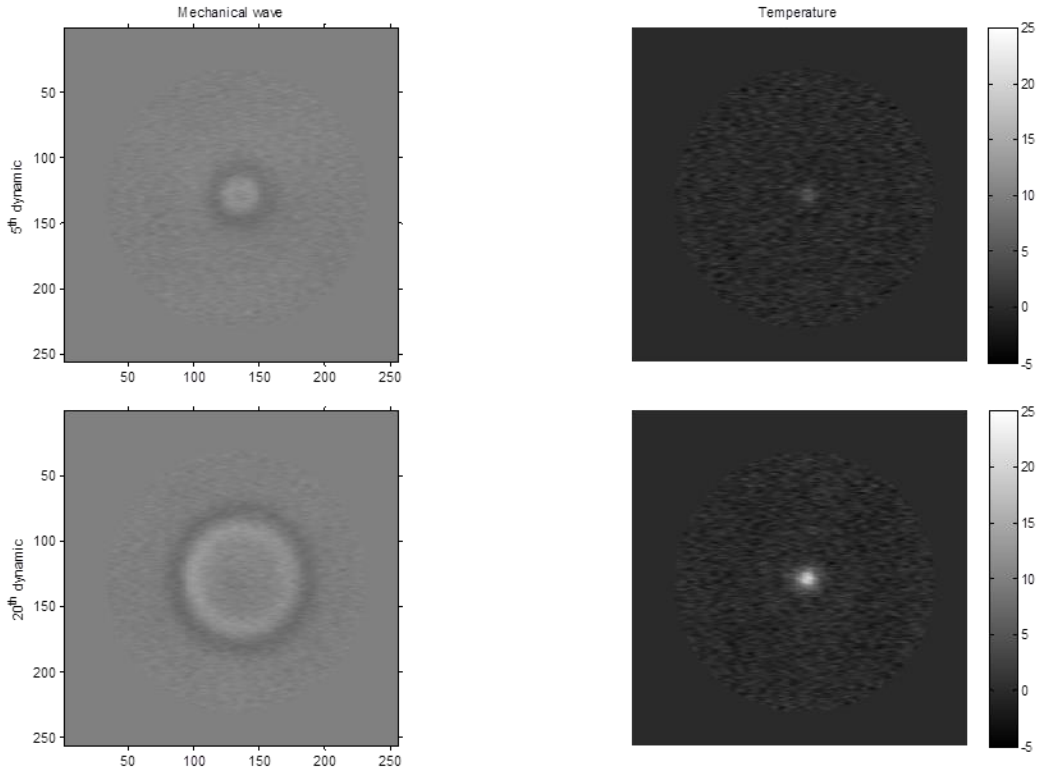

Figure 6.19 Simultaneous estimation of tissue displacement caused by ARF (left) and local increase in temperature (right) at images acquired at a temporal interval of 133 s. HIFU duty cycle = 3.1%, HIFU applied acoustic power = 250W.

The temperature evolution during the MR-ARFI acquisition of shear wave propagation at focal and far away from focal region was show in Fig. 6.20. Total 48 wave and temperature images (48×128 ultrasonic bursts) were acquired with emanating HIFU energy at power of 250W and burst duration of 2ms. The temperature rise was characterized in ^{o}C. The HIFU duty cycle (defined as the ratio of the HIFU duration to repetition time TR) is 3.1%. The temporal profile of temperature at focus region shows that temperature increase as the HIFU pulse was applied. Around 15 ^{o}C increase was reached after continuous 48 MR-ARFI acquisitions for tracking shear wave propagation. The initial temperature rise of 4^{o}C is because not enough cooling time is used to cool the phantom from last experiment.

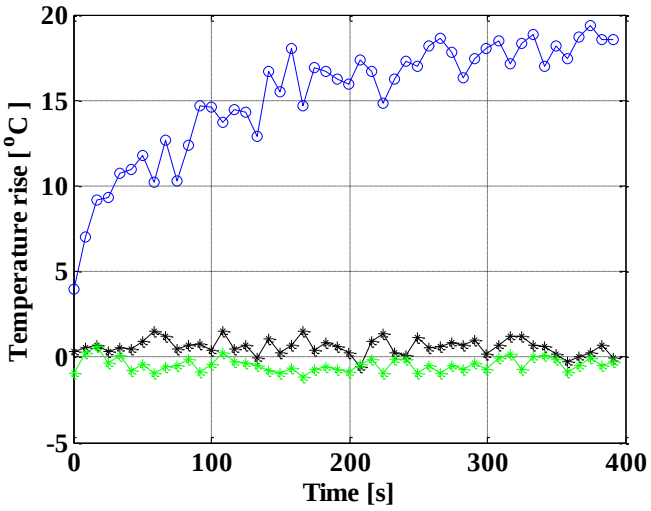

Figure 6.20 Temperature change during the MR-ARFI acquisition. HIFU duty cycle = 3.1%, applied acoustic power = 250W. Total 48 dynamics (time delays) with each dynamic of 8.3s was reconstructed. Blue line + circle is the temperature evolution at the focal point while the black and green lines plus marker star shows the temperature evolution at two pixels far away from the focal region.

To further quantify the thermal effect of using ARF from HIFU to generate shear wave, the accumulated thermal dose evolution at focus was shown in Fig. 6.21. It took about 170s (around 20 dynamic acquisitions) to reach the thermal dose at 30EM (safety region) and about 300s (around 36 dynamic acquisitions) to reach the lesion dosage of 240EM. To ensure the safety during the capturing shear wave propagation, MR-ARFI acquisition should be finished in 20 dynamics in this setting of HIFU power and duty cycle and this specific type of tissue mimicking material. The 20 dynamics of MR-ARFI acquisitions is much more than needed to estimate the tissue shear modulus.

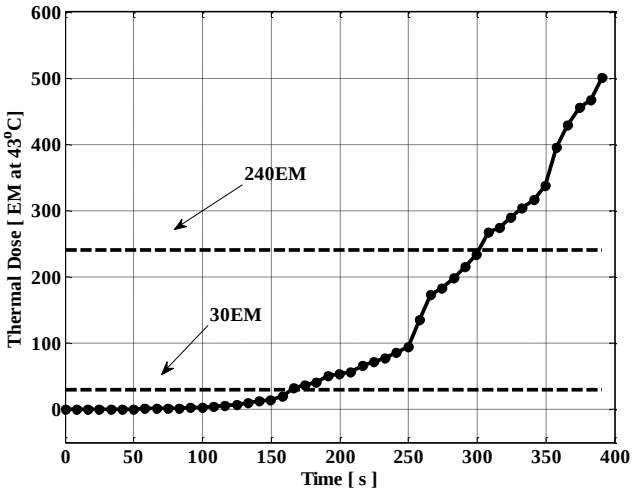

Figure 6.21 The accumulated thermal dose evolution at focus during the MR-ARFI acquisitions. HIFU duty cycle = 3.1%, applied acoustic power = 250W. Total 48 dynamics with each dynamic of 8.3s was reconstructed. Two dotted straight lines showed the thermal dosage of 30 EM and 240EM respectively.

It can also be seen that the temperature increase faster at the beginning and slow down afterwards. The rate of temperature increase was shown in Fig. 6.22. The initial slope of temperature increase is of 0.13°C/s ($\Delta T/\Delta t$) at setting condition (TR = 65ms, HIFU duty cycle = 3.1%, acoustic power = 250W).

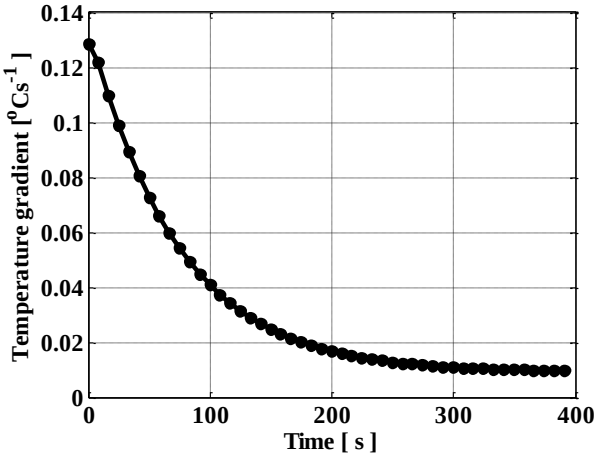

Figure 6.22 The gradient of temperature rise in time domain shows the slope of temperature rise during the MR-ARFI acquisition at focus point. HIFU duty cycle is 3.1%, applied acoustic power is 250W. Total 48 dynamics with each dynamic of 8.3s interval was reconstructed.

The rate of temperature increase is governed by the bio-transfer equation (Eq. 4.1). This equation can be simplified in phantom study since blood perfusion and Q_{met} is zero in phantom study as below

$$\rho_t c_t \frac{\partial T(\vec{r},t)}{\partial t} = k_t \nabla^2 T(\vec{r},t) + Q_{ext} \tag{6.18}$$

At the onset of HIFU application, the temperature rise in the medium is largely governed by the external thermal energy imparted to the medium (Q_{ext}). As the temperature in the target location increases, temperature rise at the focus is partly offset by heat loss due to conduction, and the rate of temperature rise starts to diminish. In the absence of perfusion, for a given HIFU heating protocol, the local temperature rise is essentially a function of the HIFU duty cycle and the thermal conductivity of the medium. A relatively high temperature rise of 15^{o}C observed in this acquisition can be mitigated by several strategies such as: 1) Reducing the number of acquisitions for measuring shear wave velocity. In this study, we imaged the wave propagation at 48 time delays. Wave speed could easily be measured with as much as one sixth of the data collected, which will substantially decrease the local temperature rise; 2) longer TR or short HIFU burst duration can be used to decrease the HIFU duty cycle; and 3) Lower HIFU power can be used to decrease the deposited energy.

While the temperature rise is a significant issue in phantom studies, this may be lesser of an issue in the presence of perfusion for *in-vivo* studies, due to additional heat losses caused by convection.

6.5 Tissue Visco-elasticity by MR-ARFI

6.5.1 Tissue Dispersion by MR-ARFI

For visco-elastic material, both wave speed and attenuation exhibits a behavior of frequency dependence which is known as dispersion. This behavior is usually studied by a series of steady-state MRE data acquired at a range of specific frequencies, or by using a broad band excitation as in the case of MR-ARFI. In steady state MRE, the velocity and attenuation can be directly estimated at each frequency at the cost of long acquisition time (above 10 minutes). In this chapter, we will focus on developing MR-ARFI to measure the dispersion of both velocity and attenuation of low frequency shear waves within tissue-like materials.

Mechanical excitation from MR-ARFI includes broad band frequencies and therefore, provides an opportunity to evaluate shear wave velocity and attenuation dispersions. For example, using the spectral analysis of motion as described in Section 6.2.2, we can extract individual frequency components of motion via Fourier domain analysis, and estimate the shear wave speed, and attenuation at each frequency to study the frequency-dependent tissue mechanical properties.

Data acquisition: The sensitivity of the MEG waveform to motional spectra should be taken into account in dispersion studies. . Fig. 6.7 (top) and 6.8 (top) The spectrum of one cycle MEG at 100Hz and 250Hz respectively are shown in Fig. 6.7 and 6.8 (top panels) respectively. The spectrum of 250Hz MEG waveform, which exhibits a frequency response from ~50Hz to ~450Hz at sensitivity decay of 30%, shows 2.5 times wider than the 100Hz MEG waveform. For this specific phantom used material and dimension, the 250Hz MEG waveform was used to encode the shear wave propagation emanated from a 2ms ARF impulse. 24 phase offsets between the

onset of MEG and ARF excitation was used to capture the dynamic shear wave propagation at time interval of 0.4ms.

Data Analysis: 1) A dynamic phase difference image (or *wave image, x*(*t*)) from the two sets of raw data (acquired at same phase offset with opposing polarities of MEG) was reconstructed ; 2) Fourier transform (FT) were performed on the dynamic wave images in temporal domain and subsequent band-pass (bandwidth of 5% of central frequency) filtering signal resulted in multiple single frequency images from the same data-set; 3) An inverse FT (IFT) was performed on filtered frequency spectrum to capture displacement wave propagation at each specific frequency $x_{f0}(t)$[199]. The flow chart of the data analysis was shown in the Fig. 6.23.

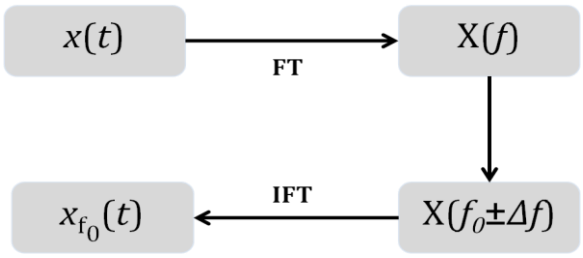

Figure 6.23 Flow chart of extracting wave propagation at single frequency from broad band impulse excitation by ARF by spectrum analysis in temporal domain

6.5.1.1 Velocity Dispersion

The reconstructed shear wave images of motion at single frequency $x_{f0}(t)$ from MR-ARFI were then used to estimate the corresponding velocity under the same algorithm discussed in Section 6.3.3.3. The shear wave velocity estimated at different frequencies (at 20Hz intervals) is shown in Fig. 6.24.

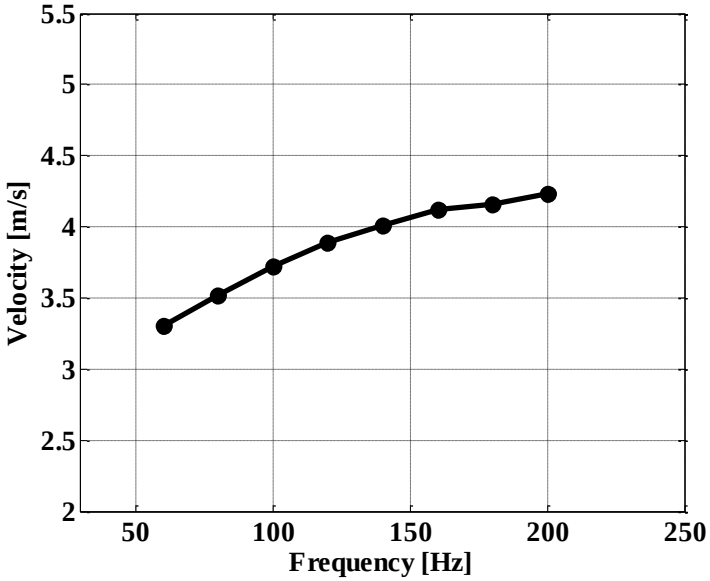

Figure 6.24 Velocity dispersion from MR-ARFI. This velocity at different frequencies was estimated from a 2-ms impulse excitation in the tissue mimicking gel phantom.

The shear wave velocity increase as the frequency but the rate decrease at the low frequency range below 200Hz while the group velocity as shown in Fig. 6.15 was 4.01m/s which was the weighted velocities at these frequencies.

To compare the velocity dispersion estimated from this new technique MR-ARFI to the conventional MRE, multiple MRE experiments was carried out with different single frequency excitation. The comparison result was shown in the following table.

Table 6.3 Comparison between the estimated velocity at frequency of 90, 120, 150, 200 Hz from impulse excitation (MR-ARFI) and the steady state cyclic excitation at single frequency (MRE)

Frequency (Hz)		90	100	120	150	200
Velocity (m/s)	MR-ARFI	3.63 ± 0.12	3.72 ± 0.09	3.89 ± 0.08	4.07 ± 0.09	4.23 ± 0.06
	MRE	2.97 ± 0.09	3.31 ± 0.12	3.47 ± 0.15	3.73 ± 0.22	4.21 ± 0.29

Both methods showed the shear wave velocity increase with the frequency. But the measurement error increase with the frequency for MRE while decrease with the frequency for MR-ARFI. In the MRE, as frequency increase the sensitivity of MEG in detecting the motion decrease and also the attenuation increase so as to result in lower SNR. While the sensitivity function (Fig. 6.7 and 6.8) for MR-ARFI is at maximum around 250Hz. As the frequency deviates away from this frequency, the sensitivity decreases. This table also showed that the discrepancy of measured velocity between these two methods decrease as the frequency increase. The minimal error introduced in the 200Hz is 0.4%. However the maximum error is 22% at low frequency 90Hz. More research needs to be done to understand this error in the lower frequency excitation. Since the impulse excitation from ARF is still not fully understood and is totally different from the steady state cyclic excitation since the wave is also affected by the boundary condition. From acquisition point of view, the MEG in MR-ARFI is not an instantaneously measurement, which is the average effect from the wave propagation during the time of performing motion encoding.

6.5.1.2 Attenuation Dispersion

To estimate the attenuation during the shear wave propagation, each dynamic wave image (corresponding to each phase offset between MEG and the mechanical stimulus) was processed by converting 2D wave image to 1D wave image to achieve higher SNR so as to accurately capture the position and intensity of negative peak value at each dynamic. In this specific ARF impulse excitation of homogeneous phantom, the wave pattern at each dynamic time point is multiple concentric circles with known center, which was the position of HIFU focus. The signal at the pixels of same distance to the HIFU focus is averaged to improve SNR, which is especially helpful in dealing the case when the shear wave traveled away from the center

in the high attenuation material. The example of 2D shear wave pattern at 10^{th} and 24^{th} dynamic time point and their corresponding conversion to 1D wave profile were shown in Fig. 6.25.

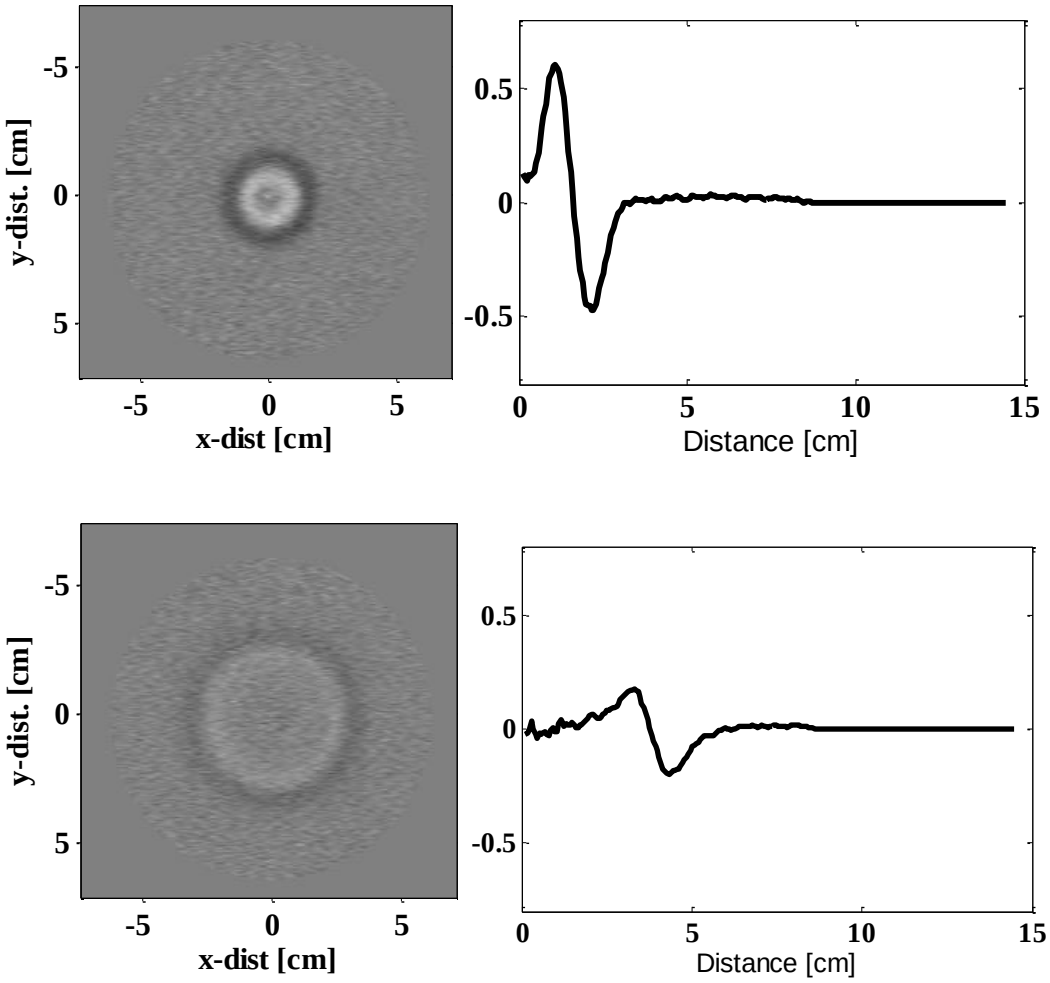

Figure 6.25 Two-dimensional wave images (Left) and their conversion to one dimensional profiles (right) at 10^{th} (Top) and 24^{th} (Bottom) dynamic were shown. The signal intensity at latter time point showed the wave propagation and the poorer signal to noise ratio (SNR). In 1D wave profile the SNR is improved at least six times higher compared to the 2D wave image at 24th dynamic.

It showed that the intensity of negative peak and the signal to noise ratio (SNR) decreased as the shear wave traveled away from the HIFU focus. Tracking the position and intensity of wave front from low SNR 2D wave images is a challenge. By converting the 2D wave pattern to 1D wave profile, the improved SNR facilitates the post process algorithm to yield attenuation. The

measured wave front intensity at different dynamics was then fitted to the following formula to yield the attenuation:

$$y(t) = e^{-\alpha x(t)} \tag{6.19}$$

Here *y* and *x* are the absolute signal intensity and position of wave front at each dynamic. Where α is the shear wave attenuation in [1/m].

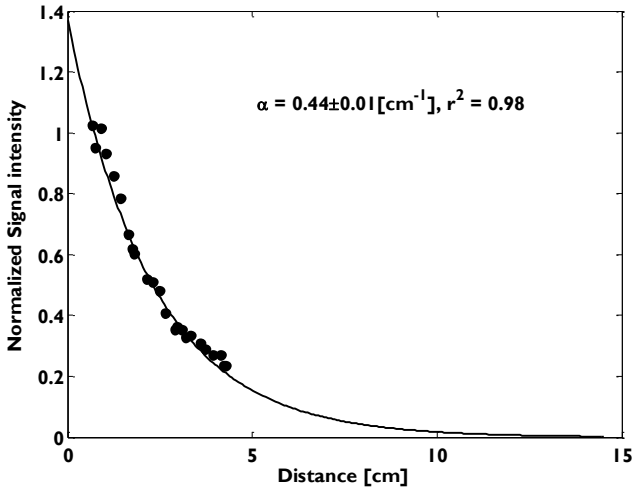

Figure 6.26 The y-axis is the relative signal intensity normalized to the MR acquired 1st dynamic. The estimated group attenuation is $0.44 \pm 0.01 \text{cm}^{-1}$, which is the combination of attenuation at a broad band.

To be noted that, the estimated shear wave attenuation (Fig. 6.26) was the group attenuation since the shear wave generated was the impulse excitation which consisted of a broad band frequency components.

To characterize the tissue attenuation dispersion from MR-ARFI measurement, the reconstructed 2D dynamic shear wave images $x_{f0}(t)$ at specific frequency underwent the same procedure of estimating group attenuation to yield the attenuation dispersion. Fig. 6.27 showed the estimated attenuation dispersion of the used tissue mimicking gel phantom using the data

$x_{f0}(t)$ reconstructed from dynamic wave images from 2ms ARF impulse excitation with MR motion encoding gradient of one cycle at 250Hz.

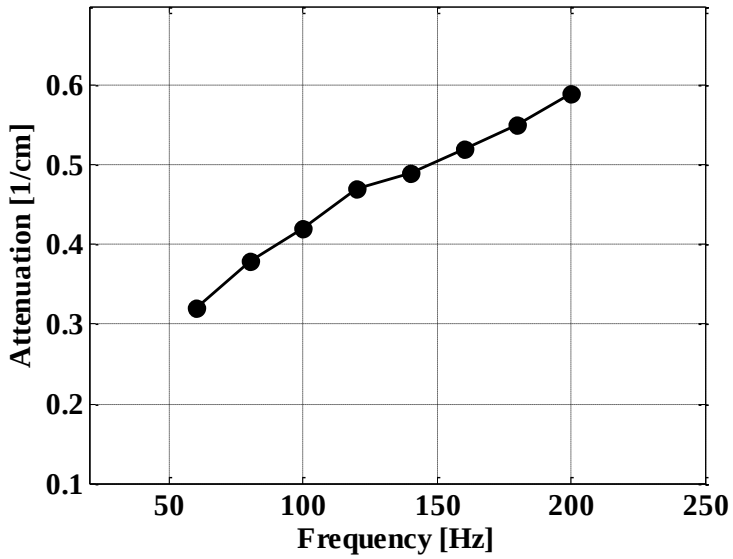

Figure 6.27 The estimated attenuation dispersion from reconstructed multiple frequencies shear wave propagations excited by ARF impulse excitation.

This showed that the attenuation also increase with the frequency. Higher frequency results in higher attenuation during the shear wave propagation and thus limited the penetration of higher frequency shear wave so as to result in the lower SNR in the region away from the excitation source which will challenge the elasticity reconstruction algorithm in those region. This is also one of the constraints of conventional MRE. However, this drawback is overcome by method of MR-ARFI since the shear wave can be initialized in deep region that is out of reach by conventional MRE.

6.5.2 Tissue Visco-elasticity Estimation by MR-ARFI

Tissue visco-elasticity (shear modulus and viscosity) can be estimated by fitting either the velocities or attenuation at different frequencies to the different rheological models. Fig. 6.28

shows the result of estimated shear modulus (μ_1 and μ_2) and shear viscosity (η) using the velocity dispersion information (Section 6.5.1.1) based on the Zener model.

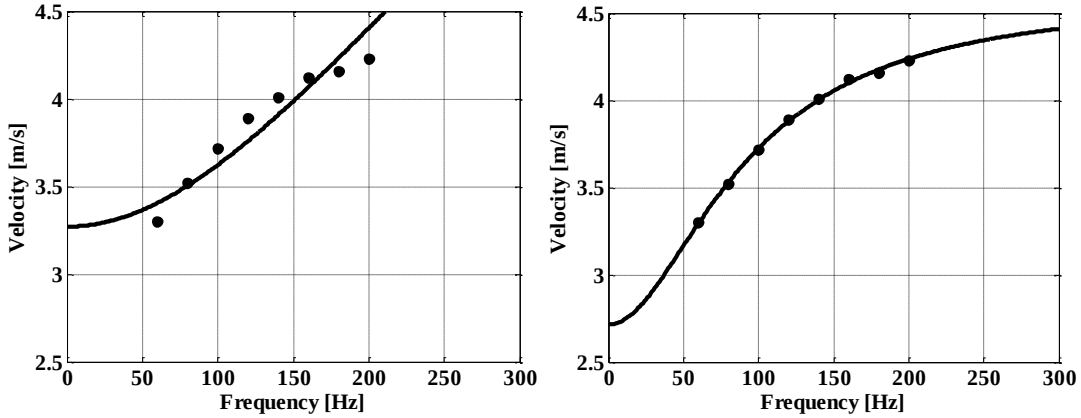

Figure 6.28 The estimated shear modulus and shear viscosity was obtained by fitting the measured velocity at different frequency (MR-ARFI) to the Zener model (r^2 =0.99, Right): μ_1 = 7.37 ±0.47kPa, η = 14.2 ±1.9Pa s, μ_2 = 13.68 ± 0.6kPa and the Voigt model(r^2 =0.91, Left): μ = 10.76 ±0.74kPa, η = 9.6 ±0.8Pa s. The black circle is the measured velocity and the solid line shows the fitted velocity.

The estimated shear modulus and viscosity from Zener were μ_1 = 7.37 ±0.47kPa, μ_2 = 13.68 ± 0.6kPa and η = 14.2 ±1.9Pa s respectively. The static shear modulus is going to be μ_1 according to Eq. 6.8a and the corresponding velocity would be 2.7m/s.

After the shear modulus and shear viscosity were obtained, the analytical attenuation behavior can be generated based on Eq. 6.8b. The analytical attenuation dispersion curve based on the estimated visco-elasticity is shown in Fig. 6.29. The solid line is the analytical attenuation dispersion curve based on the estimated visco-elasticity from velocity dispersion and the black circles were the experimental measured attenuation value.

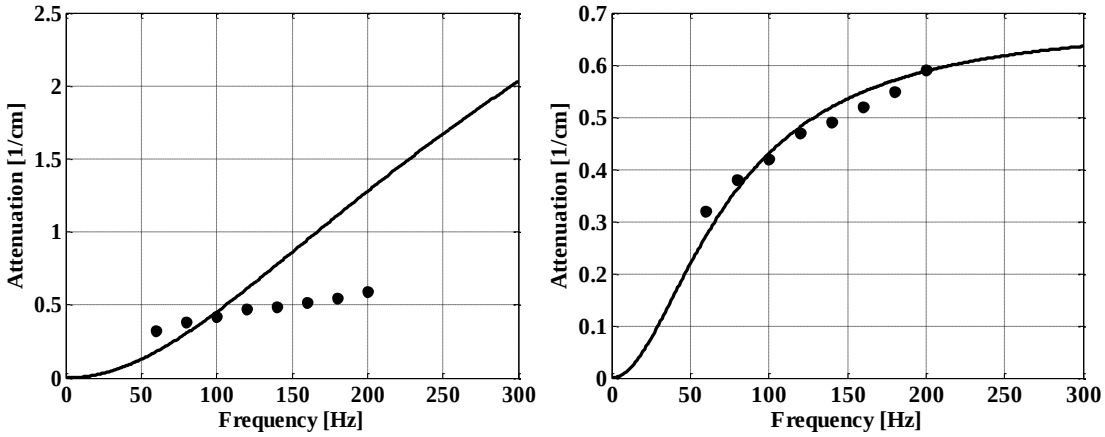

Figure 6.29 The analytical dispersion curve from the estimated shear modulus and shear viscosity of both Voigt (Left) and Zener (Right) models were plotted together with the measured attenuation dispersion data. solid line is analytical curve and the circles is the measured data.

This figure showed that the tissue visco-elasticity estimated from velocity dispersion is consistent with the experimental measured attenuation data for Zener model. While the Voigt model gave an error of magnitude compared to the experiment data. This means the Zener model gave better illustration of tissue visco-elasticity for this specific tissue mimicking gel phantom material. This model has also been shown that it gave better description of brain tissue visco-elasticity[187].

6.6 Discussion and Conclusions

Tissue mechanical property change is closely related to the pathology information. A reliable and accurate non invasive method to quantify the tissue mechanical property is highly needed instead of the invasive biopsy method which is the gold standard nowadays to stage the tumor. To non invasively quantify tissue mechanical property, three basic steps is needed: 1) non invasive introduced mechanical stress by either external or internal force; 2) non invasive imaging modality to measure tissue response to the stimulus; 3) Suitable algorithm to evaluate the tissue mechanical property. In conventional non invasive clinical MRE study, a cyclic motion was applied at the body surface to initialize the mechanical wave and then is coupled into the

inside body. The complicate tissue interfaces inside the human body make the wave propagation much complicate which challenge the reconstruction algorithm. The reachable target region is constrained by the attenuation of shear wave especially in the deep tissue. Acoustic radiation force (ARF) could be a potential tool to initialize the mechanical stimulus in deep region directly to partially overcome the attenuation effect from wave generated externally which has been used in the ultrasound-based elastography[183, 184, 200, 201]. Due to the intrinsic constraints of ultrasound imaging as discussed in the Chapter 2, MRI can be used to image the wave propagation as used in conventional clinical MRE. MRI has been shown the capability of imaging the wave propagation from the modulated ARF cyclic excitation[129]. In this work, the ARF was generated by focused ultrasound (FUS) transducer of a single element which limited the available windows for electronically steering the position of focus of ARF.

Therefore in the section of tissue mechanical property characterization in this dissertation, we used impulse excitation instead of modulated cyclic excitation from ARF from 256-element FUS transducer to initialize the shear wave directly in deep tissue region and MRI to image the resultant shear wave propagation. Due to the intrinsic broadband component in the impulse excitation, this way provides us the chance to study the tissue mechanical property behavior at a broadband frequency in a single impulse excitation which was studied previously in multiple excitations with each excitation at a single frequency and thus inevitably result in clinically prohibitive acquisition time. This is also known as multi-frequency MR elastography which has been shown to be sensitive for early detection of tumor and subtle alterations of tissue visco-elasticity changes [202, 203].

In this chapter, we used the MRI to image the wave propagation initialized from ARF and developed the elasticity reconstruction algorithm for MR-ARFI. To validate the estimated result from MR-ARFI, a conventional clinical used MRE using cyclic motion were performed. The

MR-ARFI experiments were carried out in a homogeneous phantom material. 2ms-impulse broad band ARF excitation was used to initialize the shear wave propagation. In this homogeneous phantom, the wave pattern at different dynamic time showed as a series of concentric circles of different radius in the imaging plane perpendicular to the ultrasound beam. So a reconstruction algorithm was developed specifically for this type of wave propagation. A radon transform is used to capture the distance that the shear wave traveled at different time. The elasticity was then estimated based on the velocity calculation from the traveled distance curve at different time. To be noted that, the assumption of this algorithm were as following: 1) tissue mechanical property was assumed homogeneous during the region that shear wave traveled; 2) the position where the shear wave was initialized was known which was required by the radon transform; 3) the wave propagation pattern was of the circular shape in plane perpendicular to HIFU beam; 4) only travelling shear wave exists. These assumptions were satisfied in the MR-ARFI experiments performed in homogeneous phantom. For other kind of experiments that these conditions are not satisfied, this reconstruction algorithm is not going to work or needs to be modified, which is out the scope of this dissertation. To validate the estimated elasticity from MR-ARFI, a conventional clinical MRE experiments using cyclic motion excitation were also performed. The estimated velocity was 4.01 ± 0.06m/s (2ms-impulse) and 4.21 ± 0.29m/s (200Hz) for MR-ARFI and MRE respectively. The two estimated results matched each other despite of the small discrepancy (5%). To be noted that, the velocity estimated from MR-ARFI was the group velocity which contained the motions of a broadband frequency while the velocity estimated in MRE was the velocity measured at motion of a single frequency. The velocity dispersion result showed confirmed the group velocity lies between the minimum and the measured maximum velocity at different frequency. Before discussion of velocity dispersion, the effect of the sensitivity of motion encoding gradient was studied (Table.6.4).

Table 6.4 Estimated shear velocity with different sensitvity of motion encoding graident at mechanical excitation of 2ms-impulse from MR-ARFI

MEG frequency (Hz)	120	150	200	250
Shear velocity (m/s)	3.96±0.07	4.01±0.07	3.93±0.04	4.01±0.06

Though the sensitivity of motion encoding gradient (MEG) as shown in Section. 6.2.3 was different at different MEG frequency for encoding the same impulse motion, the estimated result of group velocity were still the same with negligible difference. The sensitivity of MEG only affects the SNR in measured wave image, which will challenge the reconstruction algorithm if the SNR is too low. A frequency domain analysis method[199] was used to extract the velocity and attenuation information from MR-ARFI measurements. Both velocity and attenuation dispersion showed that they increase with the frequency. To further estimate the shear modulus and viscosity based on the measured velocity and attenuation dispersion, A proper rheological model needs to be used to depict the visco-elasticity behavior for different medium. Zener model has been shown to be a very appropriate model to describe visco-elasticity material behavior for brain and liver tissue among various rheological models[187]. Two rheological models (Voigt model and Zener model) were studied for characterizing this phantom material using MR-ARFI. The velocity dispersion curve was fitted to both the Voigt model and Zener models to yield both the shear modulus and shear viscosity (Fig. 6.28). The fitted shear modulus and viscosity was then used to generate the analytical attenuation dispersion curve which is compared to the measured attenuation dispersion from MR-ARFI (Fig. 6.29). Though the Voigt model can somewhat describe velocity dispersion, it cannot depict the attenuation dispersion and large discrepancy existed as shown in the Fig. 6.29 (Left) and the Zener model can characterize both velocity and attenuation dispersion very well. Hence, Zener model is also the better model to describe the viscoelasticity behavior for this specific phantom material.

However, as for other material, different rheological mode may be necessary to be used. The velocity dispersion at high frequency (>300Hz) is still missing due to measurement constraints by the hardware limitation of MR scanner, strong shear wave attenuation, and lower sensitivity of the MEG which will result in unacceptable SNR in wave images for high frequency study.

Further experiments needs to be performed to understand the large discrepancy of the estimated velocity at low frequency (< 12 Hz) between impulse excitation from MR-ARFI and conventional MRE. At lower frequency, the wavelength of the shear wave conventional MRE is comparable to the dimension of phantom and thus MR recorded wave pattern was a superposition of different types of waves: travelling wave, reflection wave and also standing wave depends on the geometric shape of the phantom. Though the MR recorded shear wave is only travelling wave from MR-ARFI without interfere with other types of wave, the lower sensitivity of motion encoding gradient at lower frequency also increase the measurement error.

In summary of this chapter:

1) Tissue mechanical property non invasively estimated from the new technique MR-ARFI is consistent with the result of conventional clinical used MRE in phantom study.

2) The reconstruction algorithm of tissue mechanical property from MR-ARFI in homogeneous phantom has been developed and was validated by conventional MRE.

3) Temperature change and accumulated thermal dose due to energy deposition from ARF impulse excitation during the MR-ARFI acquisitions were analyzed. The rate of temperature increase during the MR-ARFI acquisition was also characterized. Proper duty cycle of HIFU energy and total number of dynamic of wave images need to be considered carefully to avoid overheating in the focus region.

4) Zener model has been shown to be a good candidate rheological model to characterize both shear modulus and viscosity.

Chapter 7

Summary

The main focus of this dissertation was to non invasively characterize thermal (conductivity), physiological (blood perfusion rate) and mechanical (viscoelasticity) properties of living tissue in the clinical context of magnetic resonance imaging guided high-intensity focused ultrasound (MR-HIFU) surgery. Traditional approach in MR-HIFU therapy relies largely on the delivery of lethal thermal dose to the tissue. However, clinical studies from the past two decades have repeatedly found that there is not a predictable correlation between thermal dose volume delivered at the time of surgery and the eventual treatment outcome as measured by indices such as non-perfused volume. In this dissertation, we have proposed methods to measure tissue thermal properties (thermal conductivity), tissue physiologic response to heating (blood perfusion), and tissue biophysical changes that accompany heating (tissue elasticity). The specific contributions of this dissertation are as follows.

We determined the MR acquisition parameters that affect the accuracy and precision of MR-based temperature measurement (and thermal dose). Our investigations showed that in the context of volumetric MR-HIFU heating, the accuracy of temperature measurement is strongly influenced by the spatial resolution of MR temperature mapping method. In specific, the spatial resolution of the MR temperature imaging sequence should be better than a third of the diameter of the volumetric HIFU treatment area in the plane perpendicular to the HIFU beam path. While the radial targeting accuracy of the HIFU (in the plane perpendicular to the ultrasound beam path) was high, there can be substantial variation in the axial direction (parallel to the beam path), and should be taken into account when designing MR-HIFU treatment. Lastly, our investigations

confirmed previous findings that thermal dose efficiency increases with the size of volumetric ablation target.

Conceptually, non invasive tissue properties characterization using MR-HIFU involves the following steps: 1) non invasively probing tissue using HIFU; 2) employing a phase based MR method to obtain dynamic snapshots of either tissue temperature or tissue displacement; 3) estimating the regional tissue properties of the material from these snapshots. Practical realization of each of these steps required extensive theoretical and experimental developments.

We estimated *thermal conductivity* of tissue *in-vivo* using an approach previously reported in the hyperthermia literature. In specific, we approximated the spatial distribution of temperature during the cooling period to a Gaussian function, and the temporal spread of the fitted Gaussian variance was used to directly estimate tissue thermal conductivity. We experimentally tested the validity of this approach in tissue mimicking phantoms, animal studies (skeletal muscle), and human uterine fibroid tissue *in-vivo*. Our preliminary results show that the thermal conductivity of skeletal muscle and uterine fibroid are independent of temperature in the range encountered in MR-HIFU surgery (45 ºC – 90 ºC). Thermal conductivity of live tissue at this temperature range has not been reported to date. This approach may pave the way for patient specific estimation of the thermal conductivity of the tissue under MR-HIFU surgery.

We developed a numerical finite-element modeling approach to estimate tissue perfusion response to MR-HIFU heating from bio-heat transfer equation. Our model incorporated subject specific tissue thermal conductivity (using the method described above), and the measured temperature change as its experimentally determined inputs to the model, and evaluated various theoretical perfusion models that can account for the experimental observations. Our investigations showed that constant blood perfusion model did not accurately characterize tissue

thermal response, but a temperature-dependent perfusion model (TBP) more accurately described tissue physiologic response. Our results also showed that local blood perfusion rate will have to increase by more than an order of magnitude, in a span of few tens of seconds in order to describe the tissue response. We found that local blood perfusion might account for nearly 40% of the thermal energy loss, and this loss might account for the variability in outcome observed between the tissue thermal dose delivered at the time of treatment, and the eventual treatment outcome as measured by non-perfused volume, or histologically determined tissue necrosis volume.

We implemented an MR method to measure microscopic tissue displacements caused by acoustic radiation force (ARF) at the HIFU focus. Velocity and attenuation of shear waves emanating from the transient mechanical excitation caused by ARF were used to characterize the tissue visco-elastic properties. We implemented imaging methods to acquire MR-ARFI data, and developed data analysis methods to extract tissue specific visco-elastic properties. We validated these techniques in tissue mimicking phantoms. We speculate that these techniques may pave way for evaluating structural and physical alterations in tissue mechanical properties following MR-HIFU therapy.

In summary, in this dissertation we described a comprehensive set of tools to include biological response of the tissue to MR-HIFU based surgery. The methods proposed in this dissertation use existing MR-HIFU set up to extract information regarding tissue thermal conductivity, local physiologic perfusion response to heating at the MR-HIFU focus, and to measure tissue mechanical properties. We hope that these tools would pave way for the development of patient specific, MR-HIFU treatment strategies in the future.

The results from this dissertation point to several directions to explore further for optimizing MR-HIFU therapy. While our results show that the *in-vivo*, uterine fibroid thermal

conductivity values were within 15% of the mean value, there may be substantial heterogeneity among different fibroid types. More research needs to be performed for determining if there is any relationship between thermal conductivity and signal intensity of T_2 w image or other parameters such as diffusion, T_1, or even mechanical property. Relating local thermal conductivity to pathologic information may be another interesting topic, and can serve as a tissue characterization method. Blood perfusion increase due to local heating of HIFU may be potentially used in targeted drug delivery. The rapid increase in blood flow might carry a therapeutic payload differentially to the heated region, and may improve treatment efficacy.

The mechanical property change due to HIFU ablation estimated from MR-ARFI can be used to evaluate the treatment outcome after surgery. This can serve as a surrogate for contrast enhanced MRI to measure the non-perfused volume which is currently clinical available tool for evaluating treated volume after contrast agent administration. It can even be used during the HIFU surgery to tell the treated and non treated regions without the need for other external devices such as those used in conventional MR elastography.

Bibliography

1. Kennedy, J.E., *High-intensity focused ultrasound in the treatment of solid tumours.* Nat Rev Cancer, 2005. **5**(4): p. 321-7.
2. ter Haar, G.R., *High intensity focused ultrasound for the treatment of tumors.* Echocardiography, 2001. **18**(4): p. 317-22.
3. Rebillard, X., et al., *High-intensity focused ultrasound in prostate cancer; a systematic literature review of the French Association of Urology.* BJU Int, 2008. **101**(10): p. 1205-13.
4. Jolesz, F.A., et al., *Noninvasive thermal ablation of hepatocellular carcinoma by using magnetic resonance imaging-guided focused ultrasound.* Gastroenterology, 2004. **127**(5 Suppl 1): p. S242-7.
5. Tempany, C.M., et al., *MR imaging-guided focused ultrasound surgery of uterine leiomyomas: a feasibility study.* Radiology, 2003. **226**(3): p. 897-905.
6. Jolesz, F.A. and K. Hynynen, *Magnetic resonance image-guided focused ultrasound surgery.* Cancer J, 2002. **8** Suppl **1**: p. S100-12.
7. Fennessy, F.M., et al., *Uterine leiomyomas: MR imaging-guided focused ultrasound surgery--results of different treatment protocols.* Radiology, 2007. **243**(3): p. 885-93.
8. Shaplysin, L.V., et al., *High-intensity focused ultrasound (HIFU) for the prostate cancer treatment: 5-year resuts.* Urologiia, 2013. (1): p. 70-2.
9. Crouzet, S., et al., *High intensity focused ultrasound (HIFU) for prostate cancer: current clinical status, outcomes and future perspectives.* Int J Hyperthermia, 2010. **26**(8): p. 796-803.
10. Furusawa, H., et al., *Magnetic resonance-guided focused ultrasound surgery of breast cancer: reliability and effectiveness.* J Am Coll Surg, 2006. **203**(1): p. 54-63.
11. Zippel, D.B. and M.Z. Papa, *The use of MR imaging guided focused ultrasound in breast cancer patients; a preliminary phase one study and review.* Breast Cancer, 2005. **12**(1): p. 32-8.
12. Hynynen, K., et al., *MR imaging-guided focused ultrasound surgery of fibroadenomas in the breast: A feasibility study.* Radiology, 2001. **219**(1): p. 176-185.
13. Sapareto, S.A. and W.C. Dewey, *Thermal dose determination in cancer therapy.* Int J Radiat Oncol Biol Phys, 1984. **10**(6): p. 787-800.
14. Porter, W.B.a.R., *Medicine and the Five Senses.* Cambridge University Press, 2005.
15. Elias, D., et al., *Incidence of unsuspected and treatable metastatic disease associated with operable colorectal liver metastases discovered only at laparotomy (and not treated when performing percutaneous radiofrequency ablation).* Ann Surg Oncol, 2005. **12**(4): p. 298-302.
16. Holleb, A.L., D.J. Fink, and G.P. Murphy, *American Cancer Society textbook of clinical oncology.* The American Cancer Society, Inc., Atlanta, GA, 1991.
17. Vanne, A. and K. Hynynen, *MRI feedback temperature control for focused ultrasound surgery.* Physics in Medicine and Biology, 2003. **48**(1): p. 31-43.
18. Hynynen, K., *MRI guided focused ultrasound surgery.* Medical Physics, 2002. **29**(6): p. 1329-1329.
19. Cline, H.E., et al., *MR temperature mapping of focused ultrasound surgery.* Magnetic Resonance in Medicine, 1994. **31**(6): p. 628-636.

20. Ekstrand, V., et al., *Influence of electrical and thermal properties on RF ablation of breast cancer: is the tumour preferentially heated?* Biomed Eng Online, 2005. **4**: p. 41.
21. Liu, Z., et al., *Characterization of the RF ablation-induced 'oven effect': The importance of background tissue thermal conductivity on tissue heating.* International Journal of Hyperthermia, 2006. **22**(4): p. 327-342.
22. Zhu, L., D.E. Lemons, and S. Weinbaum, *A new approach for predecting the enhancement in the effective conductivity of perfused muscle tissue due to hyperthermia.* Annals of Biomedical Engineering, 1995. **23**(1): p. 1-12.
23. Lang, J., B. Erdmann, and M. Seebass, *Impact of nonlinear heat transfer on temperature control in regional hyperthermia.* IEEE Transactions on Biomedical Engineering, 1999. **46**(9): p. 1129-1138.
24. Zhang, A.L., et al., *A microscale model for prediction of breast cancer cell damage during cryosurgery.* Cryobiology, 2003. **47**(2): p. 143-154.
25. Rui, J., et al., *Effect of thermal variables on human breast cancer in cryosurgery.* Breast Cancer Research and Treatment, 1999. **53**(2): p. 185-192.
26. Diller, K.R. and T.P. Ryan, *Heat transfer in living systems: Current opportunities.* Journal of Heat Transfer-Transactions of the Asme, 1998. **120**(4): p. 810-829.
27. Hatfield, H.S. and L.G. Puch, *Thermal conductivity of human fat and muscle.* Nature, 1951. **168**(4282): p. 918-9.
28. Levy, L., et al., *Evaluation of local tissue blood flow by continuous direct measurement of thermal conductivity.* Journal of Applied Physiology, 1967. **22**(5): p. 1026-&.
29. Chato, J.C., *A method for the measurement of thermal properties of biologic materials.* Thermal problems in biotechnology. Presented at the winter annual meeting of the American Society of Mechanical Engineers(Symp. on Thermal Problem in Biotechnology (New York: ASME)), 1968: p. 16-25.
30. Valvano, J.W., J.R. Cochran, and K.R. Diller, *Thermal-conductivity and diffusivity of biomaterials measured with self-heated thermistors.* International Journal of Thermophysics, 1985. **6**(3): p. 301-311.
31. Valvano, J.W., J.T. Allen, and H.F. Bowman, *The simultaneous measurement of thermal-conductivity, thermal-diffusivity, and perfusion in small volumes of tissue.* Journal of Biomechanical Engineering-Transactions of the ASME, 1984. **106**(3): p. 192-197.
32. Cooper, T.E. and G.J. Trezek, *Probe technique for determining thermal-conductivity of tissue.* Journal of Heat Transfer, 1972. **94**(2): p. 133-&.
33. Arkin, H., K.R. Holmes, and M.M. Chen, *A sensitivity analysis of the thermal pulse decay method for measurement of local tissue conductivity and blood perfusion.* Journal of Biomechanical Engineering-Transactions of the Asme, 1986. **108**(1): p. 54-58.
34. Chen, M.M., K.R. Holmes, and V. Rupinskas, *Pulse-decay method for measuring the thermal-conductivity of living tissues.* Journal of Biomechanical Engineering-Transactions of the Asme, 1981. **103**(4): p. 253-260.
35. Liang, X.G., et al., *A convenient method of measuring the thermal-conductivity of biological tissue.* Physics in Medicine and Biology, 1991. **36**(12): p. 1599-1605.
36. Bhattacharya, A. and R.L. Mahajan, *Temperature dependence of thermal conductivity of biological tissues.* Physiological Measurement, 2003. **24**(3): p. 769-783.
37. Yi, M., et al., *Micromachined hot-wire thermal conductivity probe for biomedical applications.* IEEE Transactions on Biomedical Engineering, 2009. **56**(10): p. 2477-2484.
38. Telenkov, S.A., et al., *Non-contact measurement of thermal diffusivity in tissue.* Physics in Medicine and Biology, 2001. **46**(2): p. 551-558.

39. Anand, A. and P.J. Kaczkowski, *Noninvasive measurement of local thermal diffusivity using backscattered ultrasound and focused ultrasound heating.* Ultrasound in Medicine and Biology, 2008. **34**(9): p. 1449-1464.
40. Cheng, H.L.M. and D.B. Plewes, *Tissue thermal conductivity by magnetic resonance thermometry and focused ultrasound heating.* Journal of Magnetic Resonance Imaging, 2002. **16**(5): p. 598-609.
41. Miller, N.R., J.C. Bamber, and G.R. ter Haar, *Imaging of temperature-induced echo strain: preliminary in vitro study to assess feasibility for guiding focused ultrasound surgery.* Ultrasound Med Biol, 2004. **30**(3): p. 345-56.
42. Guilhon, E., et al., *Image-guided control of transgene expression based on local hyperthermia.* Mol Imaging, 2003. **2**(1): p. 11-7.
43. Gianfelice, D., et al., *Palliative treatment of painful bone metastases with MR imaging--guided focused ultrasound.* Radiology, 2008. **249**(1): p. 355-63.
44. Dromi, S., et al., *Pulsed-high intensity focused ultrasound and low temperature-sensitive liposomes for enhanced targeted drug delivery and antitumor effect.* Clin Cancer Res, 2007. **13**(9): p. 2722-7.
45. McDannold, N., et al., *Heat-activated liposomal MR contrast agent: Initial in-vivo results in rabbit liver and kidney.* Radiology, 2004. **230**(3): p. 743-752.
46. Song, C.W., et al., *Implication of blood flow in hyperthermic treatment of tumors.* IEEE Trans Biomed Eng, 1984. **31**(1): p. 9-16.
47. London, R.A., et al., *Laser-tissue interaction modeling with LATIS.* Appl Opt, 1997. **36**(34): p. 9068-74.
48. Jiang, S.C. and X.X. Zhang, *Effects of dynamic changes of tissue properties during laser-induced interstitial thermotherapy (LITT).* Lasers Med Sci, 2005. **19**(4): p. 197-202.
49. Xu, L.X., L. Zhu, and K.R. Holmes, *Thermoregulation in the canine prostate during transurethral microwave hyperthermia, Part I: Temperature response.* Int J Hyperthermia, 1998. **14**(1): p. 29-37.
50. Xu, L.X., L. Zhu, and K.R. Holmes, *Thermoregulation in the canine prostate during transurethral microwave hyperthermia, Part II: Blood flow response.* Int J Hyperthermia, 1998. **14**(1): p. 65-73.
51. Martin, G.T., et al., *Thermal model for the local microwave hyperthermia treatment of benign prostatic hyperplasia.* IEEE Trans Biomed Eng, 1992. **39**(8): p. 836-44.
52. Hynynen, K., et al., *The effect of blood perfusion rate on the temperature distributions induced by multiple, scanned and focused ultrasonic beams in dogs' kidneys in-vivo.* Int J Hyperthermia, 1989. **5**(4): p. 485-97.
53. Hynynen, K., *Effect of tissue perfusion on temperature elevation.* Ultrasound in Medicine and Biology, 1989. **15**: p. 41-43.
54. Zhu, L., L. Pang, and L.X. Xu, *Simultaneous measurements of local tissue temperature and blood perfusion rate in the canine prostate during radio frequency thermal therapy.* Biomech Model Mechanobiol, 2005. **4**(1): p. 1-9.
55. Fasano, V.A., et al., *Effects of laser sources (argon, Nd:YAG, CO2) on the elastic resistance of the vessel wall: histological and physical study.* Lasers Surg Med, 1983. **3**(1): p. 45-54.
56. Consigny, P.M., et al., *Effects of laser thermal angioplasty on arterial contractions and mechanics.* Cardiovasc Intervent Radiol, 1989. **12**(2): p. 83-7.
57. Sapin-de Brosses, E., et al., *Temperature dependence of the shear modulus of soft tissues assessed by ultrasound.* Phys Med Biol, 2010. **55**(6): p. 1701-18.
58. Bedossa, P., D. Dargere, and V. Paradis, *Sampling variability of liver fibrosis in chronic hepatitis C.* Hepatology, 2003. **38**(6): p. 1449-1457.

59. Regev, A., et al., *Sampling error and intraobserver variation in liver biopsy in patients with chronic HCV infection.* American Journal of Gastroenterology, 2002. **97**(10): p. 2614-2618.
60. Bedossa, P., et al., *Intraobserver and interobserver variations in liver-biopsy interpretation in patients with chronic hepatitis-C.* Hepatology, 1994. **20**(1): p. 15-20.
61. Carey, E. and W.D. Carey, *Noninvasive tests for liver disease, fibrosis, and cirrhosis: Is liver biopsy obsolete?* Cleve Clin J Med, 2010. **77**(8): p. 519-27.
62. Huwart, L., et al., *Liver fibrosis: non invasive assessment with MR elastography.* NMR Biomed, 2006. **19**(2): p. 173-9.
63. Barton, M.B., R. Harris, and S.W. Fletcher, *Does this patient have breast cancer? The screening clinical breast examination: Should it be done? How?* Jama-Journal of the American Medical Association, 1999. **282**(13): p. 1270-1280.
64. FA, D., *Physical properties of tissues.* A Comprehensive Reference Book, 1990. **6th Edition**.
65. Sarvazyan AP, S.A., Emelianov SY, Fowlkes JB, Pipe JG, Adler RS, Buxton RB, Carson PL, *Biophysical bases of Elasticity Imaging.* Acoustical Imaging. New York: Plenum Press. P223-240, 1995.
66. Sarvazyan, A., *Shear acoustic properties of soft biological tissues in medical diagnostics.* J. Acoust. Soc. Am, 1993. **93**(4): p. 2329-2330.
67. Sarvazyan AP., e.a., *Elasticity Imaging as a new modality of medical imaging for cancer detection.* In Proceeding of International Workshop on Interaction of Ultrasound with Biological Media, Valenciennes, France, 1994.
68. Skovoroda, A.R., et al., *Reconstructive elasticity imaging for large deformations.* IEEE Trans Ultrason Ferroelectr Freq Control, 1999. **46**(3): p. 523-35.
69. Leach, M.O., *Breast cancer screening in women at high risk using MRI.* NMR Biomed, 2009. **22**(1): p. 17-27.
70. Kim, Y.S., et al., *MR thermometry analysis of sonication accuracy and safety margin of volumetric MR imaging-guided high-intensity focused ultrasound ablation of symptomatic uterine fibroids.* Radiology, 2012. **265**(2): p. 627-37.
71. Zhang, J., P.H. Hor, and R. Muthupillai, *Spatial accuracy of volumetric ablation of tissue using Magnetic Resonance Imaging guided High Intensity Focused Ultrasound (MR-HIFU) with feedback control and multi-slice thermal monitoring: Initial experience in a pig model.* Proceedings, 2010 Conference, 2nd International Symposium of Focused Ultrasound. 2 (2010), 2010. **#P29**.
72. Kohler, M.O., et al., *Volumetric HIFU ablation under 3D guidance of rapid MRI thermometry.* Medical Physics, 2009. **36**(8): p. 3521-3535.
73. Illing, R.O., et al., *The safety and feasibility of extracorporeal high-intensity focused ultrasound (HIFU) for the treatment of liver and kidney tumours in a Western population.* Br J Cancer, 2005. **93**(8): p. 890-5.
74. Wijlemans, J.W., et al., *Magnetic resonance-guided high-intensity focused ultrasound (MR-HIFU) ablation of liver tumours.* Cancer Imaging, 2012. **12**: p. 387-94.
75. Beyer, R.T., *Radiation pressure—the hitory of a mislabeled tensor.* J Acoust Soc Am, 1978. **63**: p. 1025-1030.
76. Calle, S., et al., *Temporal analysis of tissue displacement induced by a transient ultrasound radiation force.* J Acoust Soc Am, 2005. **118**(5): p. 2829-40.
77. Torr, G.R., *The acoustic radiation force.* American Journal of Physics, 1984. **52**(5): p. 402-408.
78. Westervelt, P.J., *The theory of steady forces caused by sound waves.* J Acoust Soc Am, 1951. **23**(3): p. 312-315.

79. Borgnis, F.E., *Acoustic Radiation Pressure of Plane Compressional Waves.* Rev. Mod. Phys., 1953. **25**(3): p. 653 - 664.
80. Gadian, D.G., *Nuclear magnetic resonance and its application to living systems.* Oxford: Clarendon Press, 1982.
81. Haacke, E.M.e.a., *Magnetic resonance imaging physical principles and sequence design.* A John Willey & Sons, Inc., 1999.
82. Simpson, J.H. and H.Y. Carr, *Diffusion and nuclear spin relaxation in water.* Physical Review, 1958. **111**(5): p. 1201-1202.
83. Parker, D.L., et al., *Temperature distribution measurements in two-dimensional NMR imaging.* Medical Physics, 1983. **10**(3): p. 321-325.
84. Parker, D.L., *Applications of NMR imaging in hyperthermia - an evaluation of the potential for localized tissue heating and noninvasive temperature monitoring.* IEEE Transactions on Biomedical Engineering, 1984. **31**(1): p. 161-167.
85. Graham, S.J., M.J. Bronskill, and R.M. Henkelman, *Time and temperature dependence of MR parameters during thermal coagulation of ex-vivo rabbit muscle.* Magn Reson Med, 1998. **39**(2): p. 198-203.
86. Abragam, A., *The Principles of Nuclear Magnetism.* Oxford: Clarendon Press, 1983.
87. Chen, J., B.L. Daniel, and K.B. Pauly, *Investigation of proton density for measuring tissue temperature.* J Magn Reson Imaging, 2006. **23**(3): p. 430-4.
88. Young, I.R., et al., *Modeling and observation of temperature changes in-vivo using MRI.* Magn Reson Med, 1994. **32**(3): p. 358-69.
89. Graham, S.J., et al., *Analysis of changes in MR properties of tissues after heat treatment.* Magn Reson Med, 1999. **42**(6): p. 1061-71.
90. Fossheim, S.L., et al., *Thermosensitive paramagnetic liposomes for temperature control during MR imaging-guided hyperthermia: in vitro feasibility studies.* Acad Radiol, 2000. **7**(12): p. 1107-15.
91. McDannold, N., et al., *Heat-activated liposomal MR contrast agent: initial in-vivo results in rabbit liver and kidney.* Radiology, 2004. **230**(3): p. 743-52.
92. Frich, L., et al., *Experimental application of thermosensitive paramagnetic liposomes for monitoring magnetic resonance imaging guided thermal ablation.* Magn Reson Med, 2004. **52**(6): p. 1302-9.
93. Hindman, J.C., *Proton resonance shift of water in gas and liquid states.* Journal of Chemical Physics, 1966. **44**(12): p. 4582-&.
94. McDannold, N., *Quantitative MRI-based temperature mapping based on the proton resonant frequency shift: Review of validation studies.* International Journal of Hyperthermia, 2005. **21**(6): p. 533-546.
95. Graham, S.J., et al., *Quantifying tissue damage due to focused ultrasound heating observed by MRI.* Magn Reson Med, 1999. **41**(2): p. 321-8.
96. Chen, L., et al., *MRI study of immediate cell viability in focused ultrasound lesions in the rabbit brain.* J Magn Reson Imaging, 2001. **13**(1): p. 23-30.
97. Hoffmann, M.M. and M.S. Conradi, *Are there hydrogen bonds in supercritical water?* Journal of the American Chemical Society, 1997. **119**(16): p. 3811-3817.
98. Hore, P., *Nuclear Magnetic Resonance.* Oxford: Oxford University Press, 1995.
99. Muthupillai, R., et al., *Magnetic resonance elastography by direct visualization of propagating acoustic strain waves.* Science, 1995. **269**(5232): p. 1854-7.
100. Serai, S.D., A.J. Towbin, and D.J. Podberesky, *Pediatric Liver MR Elastography.* Dig Dis Sci, 2012.
101. Warner, L., et al., *Noninvasive In-vivo assessment of renal tissue elasticity during graded renal ischemia using MR elastography.* Invest Radiol, 2011. **46**(8): p. 509-14.

102. Mariappan, Y.K., et al., *MR elastography of human lung parenchyma: technical development, theoretical modeling and in-vivo validation.* J Magn Reson Imaging, 2011. **33**(6): p. 1351-61.
103. Huwart, L., et al., *Magnetic resonance elastography for the noninvasive staging of liver fibrosis.* Gastroenterology, 2008. **135**(1): p. 32-40.
104. Sinkus, R., et al., *MR elastography of breast lesions: understanding the solid/liquid duality can improve the specificity of contrast-enhanced MR mammography.* Magn Reson Med, 2007. **58**(6): p. 1135-44.
105. Sinkus, R., et al., *Viscoelastic shear properties of in-vivo breast lesions measured by MR elastography.* Magn Reson Imaging, 2005. **23**(2): p. 159-65.
106. Uffmann, K., et al., *In-vivo elasticity measurements of extremity skeletal muscle with MR elastography.* NMR Biomed, 2004. **17**(4): p. 181-90.
107. Manduca, A., et al., *Magnetic resonance elastography: non invasive mapping of tissue elasticity.* Med Image Anal, 2001. **5**(4): p. 237-54.
108. Muthupillai, R., et al., *Three dimensional magnetic resonance elastography with multi-axis motion encoding*. Proceedings of the International Society for Magnetic Resonance in Medicine Scientific Meeting and Exhibition, 1997. **5**: p. 460.
109. Moran, P.R., *A flow velocity zeugmatographic interlace for NMR imaging in humans.* Magn Reson Imaging, 1982. **1**(4): p. 197-203.
110. Pattany, P.M., et al., *Motion artifact suppression technique (MAST) for MR imaging.* J Comput Assist Tomogr, 1987. **11**(3): p. 369-77.
111. Zhang, J., P.H. Hor, and R. Muthupillai, *Frequency domain analysis of displacement wave propagation introduced by a transient high intensity focused ultrasound measured using a gradient echo sequence* Proceedings, 2012 Conference, 3rd International Symposium of Focused Ultrasound. 2 (2012), 2012. **#P140-LP**.
112. Sarvazyan, A.P., et al., *Shear wave elasticity imaging: A new ultrasonic technology of medical diagnostics.* Ultrasound in Medicine and Biology, 1998. **24**(9): p. 1419-1435.
113. Lalonde, R.J. and J.W. Hunt, *Optimizing ultrasound focus distributions for hyperthermia.* IEEE Transactions on Biomedical Engineering, 1995. **42**(10): p. 981-990.
114. Meininger, G.R., et al., *Initial experience with a novel focused ultrasound ablation system for ring ablation outside the pulmonary vein.* Journal of Interventional Cardiac Electrophysiology, 2003. **8**(2): p. 141-148.
115. O' Neil, H.T., *Theory of focusing radiators* J. Acoust. Soc. Am., 1949. **21**(5): p. 516-526.
116. Ferenc A. Jolesz, K.H.H., *MRI-Guided Focused Ultrasound Surgery.* Informa Healthcare USA, Inc, 2007.
117. Lynn, J.G., Putnam, T.J., *Histological and cerebral lesions produced by focused ultrasound.* Am. J. Pathol., 1944. **20**: p. 637-649.
118. Lynn, J.G., Zwemmer, R.L., Chick, A.J., Miller, A.F., *A new method for the generation and use of focused ultrasound in experimental biology.* J. Gen. Physiol., 1942. **26**: p. 179-193.
119. Salomir, R., et al., *Local hyperthermia with MR-guided focused ultrasound: spiral trajectory of the focal point optimized for temperature uniformity in the target region.* J Magn Reson Imaging, 2000. **12**(4): p. 571-83.
120. McDannold, N.J., F.A. Jolesz, and K.H. Hynynen, *Determination of the optimal delay between sonications during focused ultrasound surgery in rabbits by using MR imaging to monitor thermal buildup in-vivo.* Radiology, 1999. **211**(2): p. 419-26.
121. Fan, X. and K. Hynynen, *Control of the necrosed tissue volume during noninvasive ultrasound surgery using a 16-element phased array.* Med Phys, 1995. **22**(3): p. 297-306.

122. Ebbini, E.S. and C.A. Cain, *Multiple-focus ultrasound phased-array pattern syndissertation: optimal driving-signal distributions for hyperthermia.* IEEE Trans Ultrason Ferroelectr Freq Control, 1989. **36**(5): p. 540-8.
123. Fan, X. and K. Hynynen, *Ultrasound surgery using multiple sonications--treatment time considerations.* Ultrasound in Medicine and Biology, 1996. **22**(4): p. 471-82.
124. Daum, D.R. and K. Hynynen, *A 256-element ultrasonic phased array system for the treatment of large volumes of deep seated tissue.* IEEE Trans Ultrason Ferroelectr Freq Control, 1999. **46**(5): p. 1254-68.
125. Daum, D.R. and K. Hynynen, *Thermal dose optimization via temporal switching in ultrasound surgery.* IEEE Trans Ultrason Ferroelectr Freq Control, 1998. **45**(1): p. 208-15.
126. Kohler, M.O., et al., *Volumetric HIFU ablation under 3D guidance of rapid MRI thermometry.* Med Phys, 2009. **36**(8): p. 3521-35.
127. Pennes, H.H., *Analysis of tissue and arterial blood temperatures in the resting human forearm.* J Appl Physiol, 1948. **1**(2): p. 93-122.
128. Enholm, J.K., et al., *Improved volumetric MR-HIFU ablation by robust binary feedback control.* IEEE Trans Biomed Eng, 2010. **57**(1): p. 103-13.
129. Wu, T., et al., *MR imaging of shear waves generated by focused ultrasound.* Magn Reson Med, 2000. **43**(1): p. 111-5.
130. Kaye, E.A., J. Chen, and K.B. Pauly, *Rapid MR-ARFI method for focal spot localization during focused ultrasound therapy.* Magn Reson Med, 2011. **65**(3): p. 738-43.
131. Chen, J., R. Watkins, and K.B. Pauly, *Optimization of encoding gradients for MR-ARFI.* Magn Reson Med, 2010. **63**(4): p. 1050-8.
132. Nyborg, W., *Physical Acoustics.* Academic, New York, 1965. Vol. IIB: p. Chap. 11.
133. Starritt, H.C., F.A. Duck, and V.F. Humphrey, *Forces acting in the direction of propagation in pulsed ultrasound fields.* Phys Med Biol, 1991. **36**(11): p. 1465-74.
134. Souchon, R., et al., *Transient MR elastography (t-MRE) using ultrasound radiation force: Theory, safety, and initial experiments in vitro.* Magnetic Resonance in Medicine, 2008. **60**(4): p. 871-881.
135. Andreev, V.G., et al., *Observation of shear waves excited by focused ultrasound in a rubber-like medium.* Acoustical Physics, 1997. **43**(2): p. 123-128.
136. Cheng, Y., et al., *Shear wave elasticity imaging based on acoustic radiation force and optical detection.* Ultrasound in Medicine and Biology, 2012. **38**(9): p. 1637-1645.
137. Nightingale, K.R., et al., *On the feasibility of remote palpation using acoustic radiation force.* Journal of the Acoustical Society of America, 2001. **110**(1): p. 625-634.
138. Behler, R.H., et al., *ARFI ultrasound for in-vivo hemostasis assessment postcardiac catheterization, part II: pilot clinical results.* Ultrason Imaging, 2009. **31**(3): p. 159-71.
139. Wu, T., et al., *Assessment of thermal tissue ablation with MR elastography.* Magn Reson Med, 2001. **45**(1): p. 80-7.
140. Palmeri, M.L., K.D. Frinkley, and K.R. Nightingale, *Experimental studies of the thermal effects associated with radiation force imaging of soft tissue.* Ultrason Imaging, 2004. **26**(2): p. 100-14.
141. McCracken, P.J., et al., *Mechanical transient-based magnetic resonance elastography.* Magn Reson Med, 2005. **53**(3): p. 628-39.
142. Ishihara, Y., et al., *A precise and fast temperature mapping using water proton chemical shift.* Magn Reson Med, 1995. **34**(6): p. 814-23.
143. El-Sharkawy, A.M., et al., *Monitoring and correcting spatio-temporal variations of the MR scanner's static magnetic field.* MAGMA, 2006. **19**(5): p. 223-36.

144. Enholm, J.K., et al., *Improved volumetric MR-HIFU ablation by robust binary feedback control.* IEEE Transactions on Biomedical Engineering, 2010. **57**(1): p. 103-113.
145. Lenard, Z.M., et al., *Uterine leiomyomas: MR imaging-guided focused ultrasound surgery - Imaging predictors of success.* Radiology, 2008. **249**(1): p. 187-194.
146. Ueda, H., et al., *Unusual appearances of uterine leiomyomas: MR imaging findings and their histopathologic backgrounds.* Radiographics, 1999. **19**: p. S131-S145.
147. Conturo, T.E. and G.D. Smith, *Signal-to-noise in phase angle reconstruction: dynamic range extension using phase reference offsets.* Magn Reson Med, 1990. **15**(3): p. 420-37.
148. Mougenot, C., et al., *Quantification of near-field heating during volumetric MR-HIFU ablation.* Med Phys, 2011. **38**(1): p. 272-82.
149. Todd, N., et al., *The effects of spatial sampling choices on MR temperature measurements.* Magn Reson Med, 2011. **65**(2): p. 515-21.
150. Zhang, J., P.H. Hor, and R. Muthupillai, *Effect of spatial resolution on MRI guided high intensity focused ultrasound (MR-HIFU) temperature measurement.* Proceedings, 2011 Conference, International Symposium on Therapeutic Ultrasond. 11 (2011): # 1569403503, 2011.
151. Cheng, H.L. and D.B. Plewes, *Tissue thermal conductivity by magnetic resonance thermometry and focused ultrasound heating.* J Magn Reson Imaging, 2002. **16**(5): p. 598-609.
152. Zhang, J., P.H. Hor, and R. Muthupillai, *Effect of spatial resolution on magnetic resonance imaging guided high intensity focused ultrasound (MR-HIFU) temperature measurement.* International Society for Therapeutic Ultrasound (ISTU) conference, New York, USA,2011, 2011. **#1569403503**.
153. Bai, X.M. and D.E. Pegg, *Thermal property measurements on biological materials at subzero temperatures.* Journal of Biomechanical Engineering-Transactions of the ASME, 1991. **113**(4): p. 423-429.
154. Dragonu, I., et al., *Non invasive determination of tissue thermal parameters from high intensity focused ultrasound treatment monitored by volumetric MRI thermometry.* NMR in Biomedicine, 2009. **22**(8): p. 843-851.
155. *http://www.mathworks.com/help/curvefit/evaluating-goodness-of-fit.html.*
156. Zhang, J., et al., *Volumetric MRI-guided high-intensity focused ultrasound for non invasive, in-vivo determination of tissue thermal conductivity: initial experience in a pig model.* J Magn Reson Imaging, 2013. **37**(4): p. 950-7.
157. Zhang, J., et al., *Volumetric ablation of tissue using magnetic resonance imaging guided high intensity focused ultrasound (MRgFUS) with feedback control and multi-slice thermal monitoring: Initial experience in a pig model.* International Society for Magnetic Resonance in Medicine conference 2010, 2010: p. #4131.
158. Crezee, J. and J.J. Lagendijk, *Experimental verification of bioheat transfer theories: measurement of temperature profiles around large artificial vessels in perfused tissue.* Phys Med Biol, 1990. **35**(7): p. 905-23.
159. Chato, J.C., *A method for the measurement of thermal properties of biologic materials. Thermal problems in biotechnology.* Proc. Symposium on Thermal Problems in Biotechnology. American Society of Mechanical Engineers, New York, 1968: p. 16-25.
160. Ramires, M.L.V., et al., *Standard reference data for the thermal-conductivity of water.* Journal of Physical and Chemical Reference Data, 1995. **24**(3): p. 1377-1381.
161. Decastro, C.A.N., et al., *Standard reference data for the thermal-conductivity of liquids.* Journal of Physical and Chemical Reference Data, 1986. **15**(3): p. 1073-1086.
162. Chato, J.C., *Measurement of thermal properties of growing tumors.* Ann N Y Acad Sci, 1980. **335**: p. 67-85.

163. Kim, Y.S., et al., *Dynamic contrast-enhanced magnetic resonance imaging predicts immediate therapeutic response of magnetic resonance-guided high-intensity focused ultrasound ablation of symptomatic uterine fibroids.* Investigative Radiology, 2011. **46**(10): p. 639-647.
164. Zhang, J., P.H. Hor, and R. Muthupillai, *A temperature-dependent perfusion rate model for simulating temperature evolution in tissue for magnetic resonance imaging guided high intensity focused ultrasound (MR-HIFU) therapy: Initial Experience in a pig model.* Proceedings, 2011 Conference, International Society for Magnetic Resonance in Medicine, 2011. **19**(#3716).
165. Gautherie, M., *Temperature and blood flow patterns in breast cancer during natural evolution and following radiotherapy.* Prog Clin Biol Res, 1982. **107**: p. 21-64.
166. Wu, Z., et al., *A basic step toward understanding skin surface temperature distributions caused by internal heat sources.* Phys Med Biol, 2007. **52**(17): p. 5379-92.
167. *Evaluation goodness of fit.* Documentation center from matchworks. http://www.mathworks.com/help/curvefit/evaluating-goodness-of-fit.html.
168. Chen, L., et al., *Effect of blood perfusion on the ablation of liver parenchyma with high-intensity focused ultrasound.* Phys Med Biol, 1993. **38**(11): p. 1661-73.
169. Wu, H., et al., *Vasomodulation of tumor blood flow: effect on perfusion and thermal ablation size.* Ann Biomed Eng, 2009. **37**(3): p. 552-64.
170. Kim, Y.S., et al., *Uterine fibroids: postsonication temperature decay rate enables prediction of therapeutic responses to MR imaging-guided high-intensity focused ultrasound ablation.* Radiology, 2013.
171. Tompkins, D.T., et al., *Temperature-dependent versus constant-rate blood perfusion modelling in ferromagnetic thermoseed hyperthermia: results with a model of the human prostate.* Int J Hyperthermia, 1994. **10**(4): p. 517-36.
172. Mai, J.J. and M.F. Insana, *Strain imaging of internal deformation.* Ultrasound Med Biol, 2002. **28**(11-12): p. 1475-84.
173. Kanai, H., *Viscoelasticity measurement of heart wall in in-vivo.* 2004 IEEE Ultrasonics Symposium, Vols 1-3, 2004: p. 482-485.
174. Bae, U., et al., *Ultrasound thyroid elastography using carotid artery pulsation - Preliminary study.* Journal of Ultrasound in Medicine, 2007. **26**(6): p. 797-805.
175. Xu, L., et al., *Magnetic resonance elastography of the human brain: a preliminary study.* Acta Radiol, 2007. **48**(1): p. 112-5.
176. Bercoff, J., M. Tanter, and M. Fink, *Supersonic shear imaging: A new technique for soft tissue elasticity mapping.* IEEE Transactions on Ultrasonics Ferroelectrics and Frequency Control, 2004. **51**(4): p. 396-409.
177. Muthupillai, R. and R.L. Ehman, *Magnetic resonance elastography.* Nat Med, 1996. **2**(5): p. 601-3.
178. Garteiser, P., et al., *MR elastography of liver tumours: value of viscoelastic properties for tumour characterisation.* Eur Radiol, 2012.
179. Yin, M., et al., *Assessment of hepatic fibrosis with magnetic resonance elastography.* Clin Gastroenterol Hepatol, 2007. **5**(10): p. 1207-1213 e2.
180. Rouviere, O., et al., *MR elastography of the liver: preliminary results.* Radiology, 2006. **240**(2): p. 440-8.
181. Sahebjavaher, R.S., et al., *Transperineal prostate MR elastography: Initial in-vivo results.* Magn Reson Med, 2012.
182. Stewart, E.A., et al., *Magnetic resonance elastography of uterine leiomyomas: a feasibility study.* Fertil Steril, 2011. **95**(1): p. 281-4.

183. Walker, W.F., F.J. Fernandez, and L.A. Negron, *A method of imaging viscoelastic parameters with acoustic radiation force.* Physics in Medicine and Biology, 2000. **45**(6): p. 1437-1447.
184. Negron, L.A., W.F. Walker, and F.J. Fernandez, *Tissue elasticity using acoustic radiation force.* Medical Imaging 2000: Ultrasonic Imaging and Signal Processing, 2000. **1**(27): p. 306-314.
185. Auld, B.A., *Acoustic Fields and Waves in Solids.* Krieger, Malabar, FL., 1990.
186. Carcione, J., *Wave Fields in Real Media: Wave Propagation in Anisotropic, Anelastic, Porous and Electromagnetic Media* (Amsterdam: Elsevier). 2007.
187. Klatt, D., et al., *Noninvasive assessment of the rheological behavior of human organs using multifrequency MR elastography: a study of brain and liver viscoelasticity.* Phys Med Biol, 2007. **52**(24): p. 7281-94.
188. Asbach, P., et al., *Assessment of liver viscoelasticity using multifrequency MR elastography.* Magn Reson Med, 2008. **60**(2): p. 373-9.
189. Asbach, P., et al., *Viscoelasticity-based staging of hepatic fibrosis with multifrequency MR elastography.* Radiology, 2010. **257**(1): p. 80-6.
190. Kim, B.H., et al., *MR elastography for noninvasive assessment of hepatic fibrosis: experience from a tertiary center in Asia.* J Magn Reson Imaging, 2011. **34**(5): p. 1110-6.
191. Klatt, D., et al., *Viscoelasticity-based MR elastography of skeletal muscle.* Phys Med Biol, 2010. **55**(21): p. 6445-59.
192. Venkatesh, S.K., M. Yin, and R.L. Ehman, *Magnetic resonance elastography of liver: technique, analysis, and clinical applications.* J Magn Reson Imaging, 2013. **37**(3): p. 544-55.
193. Conturo, T.E. and B.H. Robinson, *Analysis of encoding efficiency in MR imaging of velocity magnitude and direction.* Magn Reson Med, 1992. **25**(2): p. 233-47.
194. Bracewell, R.N., *Two-Dimensional Imaging.* Englewood Cliffs, NJ, Prentice Hall, 1995: p. 505-537.
195. Lim, J.S., *Two-Dimensional Signal and Image Processing.* Englewood Cliffs, NJ, Prentice Hall, 1990: p. 42-45.
196. Le, Y., et al., *Feasibility of simultaneous temperature and tissue stiffness detection by MRE.* Magn Reson Med, 2006. **55**(3): p. 700-5.
197. Ishihara, Y., et al., *Precise and fast temperature mapping using water proton chemical-Shift.* Magnetic Resonance in Medicine, 1995. **34**(6): p. 814-823.
198. Rieke, V., et al., *Referenceless PRF shift thermometry.* Magn Reson Med, 2004. **51**(6): p. 1223-31.
199. Zhang, J., P.H. Hor, and R. Muthupillai, *Frequency domain analysis of displacement wave propagation introduced by a transient high intensity focused ultrasound measured using a gradient echo sequence* Proceedings, 2012 Conference, 3rd International Symposium of Focused Ultrasound, 2, P115-EA, 2012.
200. Castera, L., X. Forns, and A. Alberti, *Non invasive evaluation of liver fibrosis using transient elastography.* Journal of Hepatology, 2008. **48**(5): p. 835-847.
201. Cho, S.H., et al., *Acoustic radiation force impulse elastography for the evaluation of focal solid hepatic lesions: preliminary findings.* Ultrasound in Medicine and Biology, 2010. **36**(2): p. 202-208.
202. Sack, I., et al., *The impact of aging and gender on brain viscoelasticity.* Neuroimage, 2009. **46**(3): p. 652-7.
203. Wuerfel, J., et al., *MR-elastography reveals degradation of tissue integrity in multiple sclerosis.* Neuroimage, 2010. **49**(3): p. 2520-5.

Publication

Journal

1. **J. Zhang**, C. Mougenot, A. Partanen, R. Muthupillai*, P. Hor*, "Volumetric Magnetic Resonance Imaging–Guided High-Intensity Focused Ultrasound for Noninvasive, *in-vivo* Determination of Tissue Thermal Conductivity: Initial Experience in a Pig Model", *Journal of Magnetic Resonance Imaging*, 37(4), 2012, 950-957.

Book Chapter

1. **J. Zhang**, R. Muthupillai*, "Magnetic resonance elastography review", Book chapter: *CRC Handbook of Imaging in Biological Mechanics* (2013). Accepted.

Conference Abstracts

1. **J. Zhang**, A. Marciel, T. Karjalainen, A. Partanen, C. Mougenot, A. Pednekar, G. Costas, J. Rios, F. Clubb, J. Fischer, R. Zurawin, P. Hor*, and R. Muthupillai*, "Volumetric ablation of tissue using magnetic resonance imaging guided high intensity focused ultrasound (MRgFUS) with feedback control and multi-slice thermal monitoring: initial experience in a pig model", *Proceedings, 2010 Conference, International Society for Magnetic Resonance in Medicine. 18 (2010): # 4131.*
2. **J. Zhang**, R. Muthupillai*, J. Fischer, A. Partanen, P. Hor*, *"In-vivo* Estimation of Tissue Thermal Conductivity from Spatio-Temporal Temperature Profiles of Volumetric Sonications using MR-HIFU: Initial Experience in a Pig Model", *Proceedings, 2010 Conference, 2nd International Symposium of Focused Ultrasound. 2 (2010): # P21.*
3. **J. Zhang**, P. Hor*, J. Fischer, A. Partanen, and R. Muthupillai*, "Spatial Accuracy of Volumetric Ablation of tissue using Magnetic Resonance Imaging guided High Intensity Focused Ultrasound (MR-HIFU) with feedback control and multi-slice thermal monitoring: Initial experience in a pig model", *Proceedings, 2010 Conference, 2nd International Symposium of Focused Ultrasound. 2 (2010): # P29.*
4. **J. Zhang**, P. Hor*, J. Fischer, A. Partanen, T. Karjalainen and R. Muthupillai*, "A Temperature Dependent Perfusion Rate Model for Simulating Temperature Evolution in Tissue for Magnetic Resonance Imaging guided High Intensity Focused Ultrasound (MR-HIFU) Therapy: Initial Experience in a Pig Model", *Proceedings, 2011 Conference, International Society for Magnetic Resonance in Medicine. 19 (2011): # 3716.*
5. **J. Zhang**, P. Hor*, and R Muthupillai*, "Effect of Spatial Resolution on MRI Guided High Intensity Focused Ultrasound (MR-HIFU) Temperature Measurement", *Proceedings, 2011 Conference, International Symposium on Therapeutic Ultrasond. 11 (2011): # 1569403503.*
6. **J. Zhang**, P. Hor*, and R Muthupillai*, "Rapid magnetic resonance imaging of displacement wave propagation introduced by a transient high intensity focused ultrasound using a gradient echo sequence", *Proceedings, 2012 Conference, International Society for Magnetic Resonance in Medicine. 20 (2012): # 2922.*
7. **J. Zhang**, P. Hor*, and R Muthupillai*, "Frequency domain analysis of displacement wave propagation introduced by a transient high intensity focused ultrasound measured using a gradient echo sequence ", *Proceedings, 2012 Conference, 3rd International Symposium of Focused Ultrasound. 2 (2012): P140-LP.*

8. **J. Zhang**, P. Hor*, and R Muthupillai*, "Displacement sensitivity analysis of shear wave propagation introduced by a transient high intensity focused ultrasound using a gradient echo sequence ", *Proceedings, 2012 Conference, 3rd International Symposium of Focused Ultrasound. 2 (2012): P115-EA.*
9. **J. Zhang**, C. Uribe, J. Liu, C. Cheong, A. Pednekar, P. Angelini, and R Muthupillai*, "A systematic evaluation of left ventricular (LV) models for estimating LV volumes in children using cardiac cine (MRI) ", *Proceedings, 2013 Conference, 16th Society for Cardiovascular Magnetic Resonance. (2013): P234.*
10. **J. Zhang**, J. H. Fischer, P. H. Hor*, and R Muthupillai*, "Non invasive *in-vivo* estimation of uterine fibroid thermal conductivity in magnetic resonance imaging guided high intensity focused ultrasound (MR-HIFU) therapy ", *Proceedings, 2013 Conference, 99th Radiological Society of North America (2013): 13028501.*